



## Infrared Supercontinuum Generation in Soft-glass Fibers

**Agger, Christian**

*Publication date:*  
2013

*Document Version*  
Publisher's PDF, also known as Version of record

[Link back to DTU Orbit](#)

*Citation (APA):*  
Agger, C. (2013). *Infrared Supercontinuum Generation in Soft-glass Fibers*. Technical University of Denmark.

---

### General rights

Copyright and moral rights for the publications made accessible in the public portal are retained by the authors and/or other copyright owners and it is a condition of accessing publications that users recognise and abide by the legal requirements associated with these rights.

- Users may download and print one copy of any publication from the public portal for the purpose of private study or research.
- You may not further distribute the material or use it for any profit-making activity or commercial gain
- You may freely distribute the URL identifying the publication in the public portal

If you believe that this document breaches copyright please contact us providing details, and we will remove access to the work immediately and investigate your claim.

# Infrared Supercontinuum Generation in Soft-glass Fibers

**Christian Skovmøller Agger**

**May 24, 2013**

Main Supervisor:

Professor Ole Bang, DTU Fotonik

Co-Supervisor:

Carsten L. Thomsen, NKT Photonics A/S



# Preface

This thesis is submitted in candidacy for the Ph.D. degree from the Technical University of Denmark (DTU). It documents three years of Ph.D.-studies that have been carried out at DTU Fotonik, Department of Photonics Engineering with professor Ole Bang as main supervisor and Ph.D. Carsten L. Thomsen from NKT Photonics A/S as co-supervisor. The thesis is a summary of the most important findings and experiences gained during this first Ph.D.-study at DTU-Fotonik to work with numerical modeling of supercontinuum generation in various soft-glass optical fibers.

The project has been part of a larger collaboration between DTU, Aarhus University (AU) and industry, represented by NKT Photonics, and one important aim was developing a mid-infrared supercontinuum light source to be manufactured by NKT Photonics. I would very much like to express what a pleasure it has been to be part of a successful collaboration in which all participants seem to have gained from each other, and the whole has become larger than the sum of its parts elegantly framing the nonlinearity inherent to supercontinuum generation.

## Acknowledgements

Firstly, I wish to thank the Danish National Advanced Technology Foundation for financial support. I also want to thank my supervisors for support and collaboration both day, night and across half the globe, especially during the initial work on supercontinuum in chalcogenide fibers.

Next, I want to thank all the professional people I have become acquainted with during the last three years. Particularly, I owe my regards to Christian Petersen, Sune Dupont, Jacob Ramsay, Jan Thøgersen, and Søren Rud Keiding all from AU (though C. Petersen is currently at NKT). It has been a real pleasure to visit your lab, where I was welcomed in spite of my complete lack of laboratory experience, and where I learned about practical photonics. It was also very enjoyable to accompany you to

the CLEO-US conference in San José in May 2012, which also brings in mind our informal post-HTF-meeting conferences across the street from Bogtårnet in Aarhus, where some serious research was discussed. In addition to Carsten Thomsen at NKT, I would also like to extend my thanks to Lasse Leick who managed this entire collaboration and kept the group focus all the way to the end. Furthermore, it has been inspiring to witness practical creativity at work, and therefore I must make a special mention of the laser-carpenter Peter Morten Moselund also from NKT.

From DTU, I would like to thank all of my colleagues at DTU-Fotonik, and particularly Simon T. Sørensen for collaboration during the Ph.D.-study. Furthermore, Uffe Møller, Capser Larsen and Henrik Steffensen deserve my appreciation for having provided vital feedback for this thesis, along with my elder brother and Ph.D. Søren Agger.

On a more personal level I owe my regards to my nearest friends and colleagues, Mikkel Heuck, Johan R. Ott, Henrik Steffensen, Martin Erland Vestergaard Pedersen and Lars Rishøj whom are/were all Ph.D.-students at DTU-Fotonik. I would like to thank you for allowing me into your midst shortly after returning from an early and brief leave of absence from DTU. Luckily, the medical study at Copenhagen University was not for me. We have followed each other rather closely since, and the time span now approaches ten years. The termination of our individual Ph.D.-projects truly do mark the end of a significant part of my life.

Finally, and most importantly, I wish to express my gratitude to my wife Mette Skovmøller Agger. A Ph.D.-student is typically subject to an extensive amount of stress during the thesis writing, and I feel my writing process has been no exception. Mette has completely relieved me of all day to day domestic related obligations, allowing me to focus completely on thesis writing, yet still reminding me of a larger world outside dispersion properties, the GNLSE, nonlinear refractive index values and delayed Raman responses. For this, and for the care packages of candy, fruit, lunch and comforting text-massages in late evening hours, I owe you a great thank you and a vast amount of flowers.

This version of the present thesis is the second iteration written. It contains minor corrections to the manuscript originally handed in for evaluation on October 14th 2012. The corrections are provided both by the evaluation committee and by the author. In this regards, particularly attention should be appointed to table 5.1 in chapter 5 which was incorrect in the original version. Using values from table 5.1 from the first iteration of this thesis will lead to erroneous conclusions.

Christian Skovmøller Agger  
May 24, 2013



# Abstract

This Ph.D.-project presents numerical simulations of supercontinuum (SC) generation in optical fiber laser systems based on various soft-glass materials. Extensive numerical modeling is performed in order to understand and characterize the generated SC. This includes a review of the generalized nonlinear Schrödinger equation, and a detailed discussion of the implementation. The thesis primarily considers two types of soft-glasses, which are characterized by lower attenuation than conventional silica glasses beyond  $2\text{ }\mu\text{m}$ . This low loss enables an extension of the long wavelength edge of existing SC sources. A novel SC system, incorporating a fluor based (ZBLAN) step-index fiber (SIF), has been developed by an industrial collaborator. Numerical simulations show good agreement with measurements of fs-pumped SC generation stretching above  $4\text{ }\mu\text{m}$  in a ZBLAN fiber.

Furthermore, a design parameter, useful for designing nonlinear laser systems by passive concatenation of optical fibers is proposed. The design parameter quantifies regimes of different soliton dynamics, and predicts either stable soliton redshift for high energy conversion, or soliton fission giving large redshifts but lower energy conversion.

Finally, it is predicted numerically how it is possible to design a SC laser spanning the wavelength region between  $4$  and  $12\text{ }\mu\text{m}$ , by pumping a chalcogenide SIF with a praseodymium (Pr) doped fiber laser operating at  $4.5\text{ }\mu\text{m}$ .

---

Christian Skovmøller Agger  
May 24, 2013





# Resumé (Danish Abstract)

Dette Ph.D.-projekt præsenterer numeriske simuleringer af superkontinuums-generering i fiberbaserede optiske lasersystemer, som bygger på forskellige blødt-glas materialer. Materialerne er karakteriseret ved at have et lavere materialetab ved bølgelængder længere end  $2\text{ }\mu\text{m}$ , end konventionelle glasarter baseret på siliciumdioxid. Omfattende numerisk modellering er foretaget for at forstå og karakterisere det dannede superkontinuum. Dette inkluderer en gennemgang af den generaliserede ikke-lineære Schrödinger ligning, hvortil der gives en detaljeret diskussion af den numeriske løsning. Afhandlingen behandler fortrinsvis to typer af blødt-glas, ZBLAN og chalcogenide, hvis lave baggrundstab for lange bølgelængder muliggør en forøgelse af den bølgelængdekant, som ellers begrænser eksisterende superkontinuums-kilder. Et nyt superkontinuumssystem, der anvender en blødt-glad flourbaseret (ZBLAN) trin indeks fiber, er blevet udviklet og en prototype er fremstillet af en industriel partner. Numeriske simuleringer viser god overensstemmelse med målinger af femtosekundpumpet superkontinuums-generering, der strækker sig ud over  $4\text{ }\mu\text{m}$  i en ZBLAN fiber.

Derudover præsenterer afhandlingen en designparameter, som kan bruges ved design af ikke-lineære lasersystemer konstrueret via seriekobling af passive optiske fibre. Parameteren kvantificerer regimer for forskellig solitondynamik, og forudsiger enten stabilt rødskitte af en soliton med høj energikonverteringseffektivitet til følge, eller soliton fission som giver et stort rødskitte men lav energikonverteringseffektivitet.

Til sidst angives det, hvorledes det er muligt at designe et superkontinuumssystem med effekt i hele bølgelængderegionen mellem  $4\text{ }\mu\text{m}$  og  $12\text{ }\mu\text{m}$ . Kontinuumet dannes ved at pumpe en blødt-glas chalcogenide

trin indeks fiber med en praseodymiumdoteret fiber laser, som har en bølgelængde på  $4.5\text{ }\mu\text{m}$ .

---

Christian Skovmøller Agger  
May 24, 2013

# Contents

<b>Preface</b>	<b>iii</b>
<b>Abstract</b>	<b>vii</b>
<b>Resumé (Danish Abstract)</b>	<b>ix</b>
<b>1 Introduction</b>	<b>1</b>
<b>2 Mathematics and Physics Related to Supercontinuum Generation</b>	<b>7</b>
2.1 The Mathematical Starting Point . . . . .	8
2.2 The Linear Problem - Optical Fibers . . . . .	9
2.2.1 Finite Element Method Calculations in Comsol . .	12
2.2.2 Dispersion of a Guided Mode . . . . .	14
2.3 The Nonlinear Problem - Pulse Development . . . . .	16
2.3.1 Interpreting Results from Simulations . . . . .	19
2.4 Propagation Effects in Nonlinear Optics . . . . .	20
2.4.1 Self-phase Modulation . . . . .	20
2.4.2 Solitons . . . . .	21
2.4.3 Four-wave Mixing . . . . .	22
2.4.4 Effects From Delayed Raman Response . . . . .	22
2.4.5 Higher Order Dispersion . . . . .	24
2.5 Summary of Chapter 2 . . . . .	24
<b>3 Supercontinuum in a ZBLAN Soft-glass Fiber</b>	<b>27</b>
3.1 ZBLAN Optical Properties . . . . .	28
3.1.1 A Particular ZBLAN Fiber . . . . .	31
3.2 Delayed Raman Response in the ZBLAN Fiber . . . . .	34
3.2.1 Measurement of Delayed Raman Response in the ZBLAN Fiber . . . . .	35

3.3	Supercontinuum Generation in the ZBLAN Fiber . . . . .	38
3.3.1	Experimental Setup for Measurements of Supercontinuum . . . . .	40
3.3.2	Simulation of Supercontinuum Generation in the ZBLAN Fiber . . . . .	41
3.3.3	Normal Dispersion Regime Pumping . . . . .	43
3.3.4	Supercontinuum Generation - Continuing . . . . .	47
3.3.5	Anomalous Dispersion Regime Pumping . . . . .	49
3.3.6	Discussion of Spectral Predictions . . . . .	52
3.4	Nonlinear Fiber and Seed Laser for Mid-infrared Supercontinuum Source . . . . .	54
3.5	The Infrared Absorption Microscope . . . . .	56
3.6	The Mid-infrared Supercontinuum Laser Source . . . . .	57
3.7	Summary of Chapter 3 . . . . .	59
<b>4</b>	<b>Concatenating Fibers for Continued Nonlinear Effects</b>	<b>61</b>
4.1	Coupling of Solitons Between Nonlinear Fibers . . . . .	62
4.1.1	Tellurite Soft-glass Material . . . . .	63
4.1.2	Nonlinear Soliton Matching . . . . .	65
4.2	Summary of Chapter 4 . . . . .	71
<b>5</b>	<b>Supercontinuum up to 12 <math>\mu\text{m}</math> in Chalcogenide Fibers</b>	<b>73</b>
5.1	Chalcogenide Fiber Design . . . . .	74
5.1.1	Chalcogenide Photonic Crystal Fibers . . . . .	76
5.1.2	Chalcogenide Step-index Fibers . . . . .	77
5.2	Parameters for Modelling SCG in Chalcogenide . . . . .	80
5.2.1	Time- and Frequency Grid and Extreme Broadening . . . . .	82
5.3	Results of Simulations . . . . .	83
5.3.1	The Larger Core Fiber . . . . .	85
5.3.2	The Smaller Core Fiber . . . . .	86
5.3.3	Bandwidths and Fiber Length . . . . .	87
5.4	Summary of Chapter 5 . . . . .	89
<b>6</b>	<b>Conclusion</b>	<b>91</b>
6.1	Future Perspectives in Mid-IR SCG . . . . .	92
<b>A</b>	<b>The Generalized Nonlinear Schrödinger Equation in the Interaction Picture</b>	<b>95</b>
A.1	The GNLSE . . . . .	96
A.2	Transforming into the IAP . . . . .	97

<b>B Structuring a Matlab-code for Solving the Generalized Non-linear Schrödinger Equation</b>	<b>99</b>
B.1 Code for Solving the GNLSE (or NLSE) . . . . .	101
B.2 Structure of Code . . . . .	101
B.2.1 Speed Optimizing . . . . .	104
B.2.2 Small Example . . . . .	104
B.2.3 GNLSE Implementation . . . . .	105
B.2.4 NLSE Implementation . . . . .	106
<b>C Fourier Transforming</b>	<b>107</b>
C.1 Common Pulse Shapes . . . . .	108
C.1.1 The Gaussian Shape . . . . .	108
C.1.2 The sech Shape . . . . .	109
C.2 A Few Needed Relations . . . . .	110
C.2.1 The $\delta$ -function . . . . .	110
C.2.2 Transforming the Differential Operator . . . . .	111
C.2.3 FT of Real Valued Function . . . . .	111
C.3 Parseval's Theorem . . . . .	111
C.3.1 ESD in Wavelength Domain . . . . .	112
C.4 Fourier Transform in Matlab . . . . .	113
C.4.1 Making the Time and Frequency Axes . . . . .	115
C.4.2 Using the Provided Matlab Functions . . . . .	116
C.4.3 funcAgrawalFT.m . . . . .	117
C.4.4 funcAgrawaliFT.m . . . . .	117
<b>D Expansion Frequency and Pseudo Frequency Axis</b>	<b>119</b>
D.1 Identical Expansion and Pump Frequency . . . . .	119
D.2 Non-identical Expansion and Pump Frequency . . . . .	120
<b>E Why the Pump Frequency Appears in the Linear Operator</b>	<b>123</b>
E.1 The Retarded Time Frame . . . . .	124
<b>F Conserved Quantity in the IAP GNLSE</b>	<b>127</b>
F.1 Deriving the Photon Number in the IAP GNLSE . . . . .	127
<b>G Obtaining Material Response from Raman Gain Measurement</b>	<b>133</b>
G.1 The Math . . . . .	133
G.1.1 Material Response of ZBLAN . . . . .	135

List of Acronyms	137
Bibliography	141
H Bibliography	141

# Chapter 1

## Introduction

Electromagnetic radiation is an omnipresent part of our world and the electromagnetic spectrum that summarizes the properties and frequencies associated with the electromagnetic waves propagating in free space, is so vast it covers waves with wavelengths from thousands of kilometres ( $10^6$  m) over 20 orders of magnitude to wavelengths as small as the nucleus of an atom ( $10^{-14}$  m) [1]. The everyday human though, will experience only a few small overlapping fractions of the electromagnetic spectrum directly. We feel the heat from the sun, which is infrared (IR) radiation, our built-in detectors (eyes) view the visible part of the sun spectrum reflected off of things in our surroundings, and we get sunburned by the ultraviolet (UV) part of the sun spectrum. These mentioned parts though, cover only the spectral range from approximately 300 nm and to 1  $\mu\text{m}$  [1].

Conventional laser sources cover even smaller fractions of the electromagnetic spectrum, and often have very narrow line widths that are best imagined as single colors. The laser source is a light source with a particular set of traits, distinguishing it from a traditional source of light, e.g., an incandescent lamp. More strictly speaking, lasers show spatial and temporal coherence, i.e., the photons of a laser source propagate in phase and in a well defined spatial mode of the electromagnetic field. It is the coherence properties in particular that make lasers very useful for applications requiring high brightness, i.e., much light confined to a small area and solid angle. An exhaustive list of uses for lasers is impossible to make, but uses range from low power applications like sensing and optical tweezers, over optical communications to welding, cutting and the ultra-high power: *record 500-trillion-Watt laser shot* of the National Ignition



Facility used for kick-starting a fusion process [2].

It is the fundamental working mechanism of a conventional laser that cause the narrow linewidth or single color, and while often times useful, a broad band laser, containing all colors at once, is also desirable. The aim of this thesis, is to aid in developing such a source, i.e., one that combines the spatial and temporal properties of a conventional laser with a continuum of colors, forming a so called supercontinuum (SC), and consequently appearing as a white light laser (at least when in the visible part of the spectrum).

A SC can be formed by sending a light pulse from a conventional laser into (pumping) a nonlinear optical fiber, where the narrow band pulse undergoes spectral broadening due to nonlinear effects, and partially inherits the coherence properties of the pump. A low-loss optical fiber allows the photons of the pump beam to interact with each other and with the material over long distances, without needing amplification. Furthermore, the spatial confinement of the photons in a fiber, can be so small that it enhances the nonlinear effects greatly, promoting spectral broadening. Thus, a low loss optical fiber that supports a small and well confined mode, is a key enabler for robust SC sources.

Commercial SC sources have already been developed by our industrial collaborators at NKT Photonics A/S, and can be bought off the shelf. These available sources cover the range from approximately 400 nm (visible) and to 2.4  $\mu\text{m}$  (near-IR), with good laser properties [3], but has nearly reached the limitations of the silica technology they build on. The short wavelength edge (also called, the blue wavelength edge) is still investigated for a potential to expand it into the UV but the long wavelength edge (also called, the red wavelength edge) has reached its full potential. This is realized, because the transmission window for fused silica stretches from below 400 nm but not much further than approximately 2  $\mu\text{m}$  after which, the material absorption increases by orders of magnitude [4].

The maturation of the silica technology has caused a gradual shift towards other types of glass, that have transmission windows stretching further into the IR, for the nonlinear fiber in SC sources. In particular ZBLAN ( $\text{ZrF}_4\text{BaF}_2\text{LaF}_3\text{AlF}_3\text{NaF}$ ), tellurite ( $\text{TeO}_2\text{Na}_2\text{ZnF}_2$ ), and chalcogenide ( $\text{As}_2\text{Se}_3$ ) have been investigated in this thesis, but other alternatives, that allow drawing into fibers, are also available [5]. The nonlinear properties are approximately the same for silica and ZBLAN [6, 7], while tellurite is roughly 30 times as nonlinear as silica [8], and chalcogenide can be as much as a factor of 1000 more nonlinear than silica [9, 10].

The soft-glass materials though, have different linear properties than silica, and particularly the zero dispersion wavelength (ZDW) of the bulk materials are different, and consequently warrants a reconsideration for the design of a proper pumping laser system.

Creating a SC source with a spectrum stretching further into the mid-IR, than is already available, is attracting because it opens the door to numerous applications outside the range of existing SC sources. In particular directional infrared counter measures (DIRCM) is a promising application where an IR SC source confuses, or even saturates, the sensors in the tip of a heat seeking missile, causing it to loose track of target, and thereby protecting, e.g., civilian aircrafts from potential threats. DIRCM is a potential application for a source covering the range between 1  $\mu\text{m}$  and to 4  $\mu\text{m}$ . Proteins and lipids show absorption from around 3  $\mu\text{m}$  to above 9  $\mu\text{m}$  [11], and thus extending the red edge of beyond 4  $\mu\text{m}$  and to 12  $\mu\text{m}$ , has been proposed in order to create a source for in-vivo and non invasive optical biopsies useful in early cancer detection [12]. Besides these two applications, a range of other uses have been proposed, e.g., detection of explosive or toxic gases, pollution monitoring, industrial quality checking in, e.g., agricultural, diary, or pharmaceutical productions. Also mentioned are light detection and ranging (LIDAR), IR absorption microscopes, optical components testing, and numerous others.

## Goals

To be quite clear and specific, the aim of this project, at its onset was to

1. aid in developing a SC source with a spectrum stretching above 4  $\mu\text{m}$  by use of ZBLAN-based fiber technology.
2. gain experience in simulations of supercontinuum generation (SCG) in interchangeable glass materials, specifically the soft-glasses mentioned above.

Along the course of the project, these goals where accompanied by

3. introduction of a design parameter, useful when creating laser systems by concatenating nonlinear optical fibers. The parameter determines the behaviour, expected from nonlinear dynamics upon coupling a soliton between two fibers.
4. numerical investigation of the possibility of making a SC source stretching as far as 12  $\mu\text{m}$  or further, by simulating a praseodymium

(Pr) doped fiber laser seed system pumping a highly nonlinear chalcogenide optical fiber.

## Outline

This report is divided into the following chapters: In chapter 2 is given a brief account for the theory behind SCG, and the chapter introduces the basic nonlinear processes and the mathematical problems that need to be solved, in order to enable numerical predictions of SC spectra. Chapter 3 investigates ZBLAN based optical fibers, and their use in a mid-IR SC source. Particularly, the linear properties of ZBLAN are reviewed, a measurement of the delayed Raman response is presented, along with measurements and simulations of SC. Finally is given a brief review of an application developed by our collaborators at Aarhus University (AU), where a mid-IR SC is used as the light source in an absorption microscope [13], and chapter 3 concludes with a presentation of the celebrated end product of the successful collaboration between universities and industry.

Chapter 4 introduces the nonlinear coupling coefficient that defines regimes of nonlinear dynamics following the coupling of a soliton between two nonlinear fibers. The parameter is useful when choosing fibers for a passively concatenated fiber system that enables wavelength tuning with a high energy conversion based on stable and continuous frequency down shift of a soliton, or a large redshift with low energy conversion, caused by soliton fission.

Finally, chapter 5 considers SCG in chalcogenide soft-glass fibers. Two possible pump sources are considered, and both conventional step-index fibers (SIFs) and microstructured optical fibers are investigated for potential use in IR SCG. The chapter presents numerical simulations of SC in a conventional fiber, where it is proposed that a SC spectrum spanning a region between 4 and possibly beyond 12  $\mu\text{m}$  is achievable. Lastly, chapter 6 presents a summary of the presented work and an outlook towards interesting future issues to continue working with.

The appendixes, starting page 95, are readable in their own right, and is meant to be relevant for anyone constructing a numerical solver for the generalized nonlinear Schrödinger equation (GNLSE). They present useful building blocks needed to construct a solver code, and should lead the reader to a position enabling the building of a working code. The appendixes are divided into the following: In appendix A the traditional

version of the GNLSE [6,14] is recast to better include the large frequency range covered by generated SC in the IR, and the transformation into the interaction picture (IAP) is reviewed in detail. Appendix B contains a code example, most relevant to be followed by a developer seeking to investigate different fibers, different materials or different versions of the GNLSE using a single robust code. In the remaining appendixes, C through F, technical details for understanding the GNLSE, and how to solve it, is included. Finally in appendix G, it is specified how to convert a measurement of the Raman gain profile to a mathematical expression for the full material response, including both instantaneous response and delayed Raman response that can be incorporated in the GNLSE.



## Chapter 2

# Mathematics and Physics Related to Supercontinuum Generation

In linear optics, frequencies are only amplified or attenuated, while in nonlinear optics, new frequencies can be generated, and a spectrum of a laser pulse can change drastically during propagation. Historically, the first observation of supercontinuum (SC) is ascribed to Alfano and Shapiro [15] and was made in 1970. Here nondegenerate four-photon coupling (or four-wave mixing (FWM)) caused a frequency doubled laser beam at 530 nm (doubled from 1.06  $\mu\text{m}$ ), with a relatively large peak-power, to broaden into a spectrum covering the range from approximately 400 and to 700 nm. This initial experiment was done in bulk borosilicate glass, and required a large peak power because the nonlinearity of glass is small. Five years later, in 1975, Lin and Stolen produced a broad spectrum in a nonlinear optical fiber using a ns-pulsed laser with significantly less peak power [16]. Ultra low loss optical fibers with low dispersion, can compensate for a low generic nonlinearity, because they will allow light to propagate and interact with the material over long distances without the pulse content diverging temporally or being lost or absorbed by the waveguide. Furthermore, the well developed fabrication technology of optical fibers, provide waveguides where the guided mode can have a small effective area, giving a large electric field strength, thereby enhancing the effective nonlinearity. For these reasons, optical fiber based SC sources are considered exclusively in this work and the generic configuration we investigate consist of

1. a pulsed pump laser system that generate narrow band laser pulses.
2. a fiber optical waveguide, designed and chosen so that it enables nonlinear processes to broaden the pump pulse significantly during propagation.

This chapter reviews the basic theory needed to understand results presented in chapters 3, 4, and 5. It starts by a brief walk-through of the linear properties of fiber waveguides in section 2.2, where the finite element method (FEM) calculation that yields the properties of the optical fibers is also introduced. Section 2.3 reviews the generalized nonlinear Schrödinger equation (GNLSE), which is the nonlinear differential equation that governs the supercontinuum generation (SCG) itself, and finally section 2.4 reviews isolated effects often observed in SCG.

## 2.1 The Mathematical Starting Point

The starting point for modeling any classical electrodynamic phenomenon is Maxwell's equations for the electric and magnetic fields. They are [1,6]

$$\nabla \times \mathbf{E} = -\frac{\partial \mathbf{B}}{\partial t}, \quad \nabla \times \mathbf{H} = \mathbf{J} + \frac{\partial \mathbf{D}}{\partial t}, \quad \nabla \cdot \mathbf{D} = \rho_f, \quad \nabla \cdot \mathbf{B} = 0 \quad (2.1.1)$$

where  $\mathbf{E}$  is the electric field,  $\mathbf{B}$  is the magnetic flux density,  $\mathbf{H}$  is the magnetic field,  $\mathbf{J}$  is the current density,  $\mathbf{D}$  is the electric displacement field and  $\rho_f$  is the free charge density. The fields in the above equations are connected by the following macroscopic relations

$$\mathbf{D} = \epsilon_0 \mathbf{E} + \mathbf{P} = \epsilon \mathbf{E} \quad \text{and} \quad \mathbf{B} = \mu_0 \mathbf{H} + \mathbf{M} \quad (2.1.2)$$

valid for fields in arbitrary media. Here  $\epsilon$  ( $\epsilon_0$ ) is the (vacuum) permittivity,  $\mathbf{P}$  is the electric polarization,  $\mu_0$  is the free space permeability and  $\mathbf{M}$  is the magnetization. In this thesis, and commonly in fiber optics in general, one takes  $\mathbf{M} = \mathbf{J} = 0$ , because optical fibers are dielectric waveguides that do not become magnetized, nor do they conduct current. The polarization, which in essence describes the interaction between light and medium, will depend linearly on the electric field strength when it is not too strong, so that

$$\mathbf{D} = \epsilon_0 \mathbf{E} + \mathbf{P} = \epsilon_0 \mathbf{E} + \epsilon_0 \chi^{(1)} \mathbf{E} = \epsilon_0 (1 + \chi^{(1)}) \mathbf{E}. \quad (2.1.3)$$

where  $\chi^{(1)}$  is the linear, or first order, susceptibility and  $1 + \chi^{(1)} = \epsilon_r$  is sometimes referred to as the relative permittivity. Substituting Eq. (2.1.3)

into Maxwell's equations, one can derive a linear wave equation (see section 2.2.1). When the electric field strength is large enough however, as can happen in an optical fiber, when much light is confined to a small core, the polarization becomes nonlinear. This can be illustrated as,

$$\mathbf{D} = \epsilon_0 \mathbf{E} + \mathbf{P} = \epsilon_0 (1 + \chi^{(1)} + \chi^{(2)} \mathbf{E} + \chi^{(3)} \mathbf{E} \mathbf{E} + \dots) \mathbf{E}. \quad (2.1.4)$$

where  $\chi^{(j)}$ ,  $j = 1, 2, \dots$  is the  $j$ 'th order susceptibility tensor. Generally, the susceptibility tensor is time dependent, and a convolution between the electric field and the susceptibility should be included [6], but this is left out here for brevity. Inserting Eq. (2.1.4) in Maxwell's equations will lead to a complicated nonlinear tensorial differential equation for the electromagnetic field development that does not lend itself to solving easily. Instead, if it is assumed that light propagates in a single linearly polarized mode of the electromagnetic field, e.g., as in the fundamental mode of an optical fiber, then the problem can be shown to divide itself into two parts [6, 17]. One transverse part for the properties of the field distribution in the mentioned mode of the fiber, and one longitudinal part for the dynamical development of the electric field envelope in the direction of propagation. These two parts are solved separately and coupled together through the frequency dependent propagation constant  $\beta(\omega)$  and effective area  $A_{\text{eff}}(\omega)$ , which are outputs from solving the first part and inputs for the second, or dynamical part, of the problem.

## 2.2 The Linear Problem - Optical Fibers

The first part of the nonlinear pulse propagation problem, is to solve Maxwell's equations for the transverse field distribution in the fiber. This determines the linear guiding properties of the medium the electromagnetic field is developing in. There are various different kinds of optical fibers available for different applications, and they are generally divided into two classes depending on the underlying physical guiding mechanism. One class is the index guiding fibers while the other is photonic bandgap (PBG) guiding fibers.

In an index guiding fiber, light is guided by a refractive index difference that cause total internal reflection [1] to reflect light, diverging from the fiber core, back into the core region, and thus confining light to it. The step-index fiber (SIF) is the index guiding fiber type, which is primarily investigated in the following chapters. A schematic of a SIF cross section is shown in Fig. 2.1-left. It consists of a core with radius  $a$



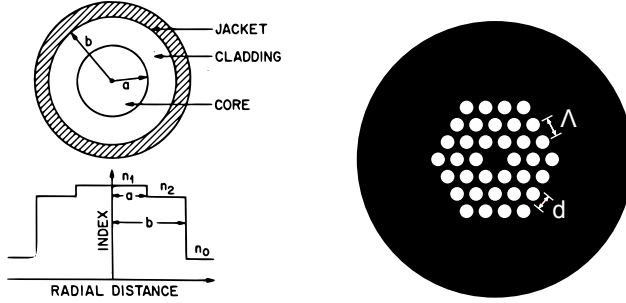


**Figure 2.1:** Left: Schematic of a SIF cross section with core (cladding) radius  $a$  ( $b$ ) and refractive index  $n_1$  ( $n_2$ ). The index profile is shown below the cross section. Right: Schematic of three-ring triangular lattice PCF showing the solid material (black) and air holes (white) with pitch  $\Lambda$  and air hole diameter  $d$ . (Left graphics is from [6], right is courtesy of Simon T. Sørensen).

that has a refractive index  $n_1 = n_1(\omega)$  and a cladding of radius  $b$  with refractive index  $n_2 = n_2(\omega) < n_1$ . The frequency dependence of  $n_1$  and  $n_2$  is referred to as material dispersion. The total internal reflection occurs for light propagating out of the plane of the paper in Fig. 2.1-left and diverging away from the core, at the interface where  $n_1$  changes abruptly to  $n_2$  [18, 19]. Outside the cladding, where the radial distance exceeds  $b$ , is a jacket material that provides protection and adds flexibility and robustness to the fiber. Basically, a SIF is manufactured by surrounding a bulk cane of core material by a cane of cladding material, heating the ensemble until it softens enough, and then drawing it into a fiber. The refractive index difference between core and cladding is typically achieved by doping the core material of the fiber with various elements that raise the refractive index. Along with the refractive indexes  $n_1$  and  $n_2$ , the core and cladding radii  $a$  and  $b$ , a SIF is characterized by the normalized frequency (or  $V$ -parameter) and the numerical aperture (NA) defined as

$$V = \frac{2\pi a}{\lambda} \text{NA} \quad \text{and} \quad \text{NA} = \sqrt{n_1^2 - n_2^2} \approx \sqrt{2n_1(n_1 - n_2)} = n_1 \sqrt{2 \left(1 - \frac{n_2}{n_1}\right)} \quad (2.2.1)$$

respectively. Instead of the NA, the difference between core and cladding refractive index is occasionally characterized by the relative index contrast  $\Delta = (n_1^2 - n_2^2)/(2n_1^2)$  [19]. It can be shown that a SIFs supports only one

single guided linearly polarized mode (the fundamental mode) below the so called cut-off frequency, i.e., below  $V \approx 2.405$  for a given wavelength, core radius  $a$ , and NA [18, 19]. The NA determines the maximum angle of incidence,  $\theta_{\max} = \sin^{-1}(\text{NA})$ , for a light beam that will become guided by the fiber [18]. As a rule of thumb, the larger the NA, the better the mode is confined to the core, but as the NA increases, so does the number of guided modes supported by the fiber. From the approximated result in Eq. (2.2.1), it is obvious that the magnitude of the NA increases linearly with the absolute value of the refractive index of the basic SIF material (here  $n_1$ ) for a given core-to-cladding index ratio. Practically this means that fibers, made from high refractive index materials, allows a larger NA for a given core-to-cladding index ratio.

Another class of index guiding fibers, are the PCFs, and the advent of these fibers, approximately half way through the nineteen nineties [20], lead to much interest in SCG in subsequent years after the first demonstration of SC in a PCF [21]. PCFs are particularly well suited for SCG because they offer very tight mode confinement with a small mode area leading to a large effective nonlinearity, they can be endlessly single-mode [22], i.e., only one single guided mode exist for any wavelength, and the dispersion properties can be engineered to a large extent [14, 23]. A schematic of a PCF is shown in Fig. 2.1-right where the black background represents solid glass with refractive index  $n = n(\omega)$ , and white circles mark air holes (with refractive index  $n_{\text{air}} = 1$ ) that stretch along the entire length of the fiber. The grid of air holes is placed in a periodic manner around a core, a defect in the periodic lattice, where an air hole is missing. The air holes provide a refractive index boundary, with a large effective index difference, surrounding the core, providing tight mode confinement, and causing the total internal reflection, even though the interface where reflection occurs is less well defined than in a SIF. The triangular lattice PCF is characterized by the hole-to-hole distance, or pitch,  $\Lambda$  and the hole diameter  $d$ , along with the number of air hole rings and the grid structure. Examples of other grid structures are, e.g., cobweb lattice [24] or suspended core/wagon-wheel [25, 26]. PCFs are commonly made from a single material, thus removing the need for a dopant, but the fabrication procedure however, is more complicated than for the SIFs (see Fig. 4.3, page 65 for an example of a drawn PCF).

An example from the category of PBG guiding fibers, is the hollow core fiber [17]. The PBG guiding fibers work by establishing a frequency region where propagation is forbidden transversally in the structure. In

this way, light, with a frequency in the PBG, cannot escape the core once inside it. Such fibers, however, are not treated here.

### 2.2.1 Finite Element Method Calculations in Comsol

An approximate analytical solution is available for the transverse field distribution in a SIF, and from this, much of the physics, e.g., the cut-off frequency mentioned in the last section can be deduced. The approximation, however, requires that the index difference between core and cladding is small, and this can become questionable for the fibers considered later on, particularly for the chalcogenide fibers investigated in chapter 5. Furthermore, since we also consider PCFs that do not have an analytical solution for the field distribution, a FEM solver is used in any case. The FEM solver is a commercially available software program called **Comsol** (version 3.5a), and it solves the frequency domain equation,

$$\nabla \times (n^{-2} \nabla \times \tilde{\mathbf{H}}) - k_0^2 \tilde{\mathbf{H}} = \mathbf{0}, \quad \tilde{\mathbf{H}} = \tilde{\mathbf{H}}(x, y) e^{uz} \quad (2.2.2)$$

for the eigenvalue  $u = -i\beta - \delta_z$  (**Comsol** uses the symbol  $\lambda$  for the eigenvalue, but this is avoided here) and the magnetic field profile  $\tilde{\mathbf{H}}(x, y)$  at the frequency specified through the input vacuum wavenumber  $k_0 = \omega/c = 2\pi/\lambda$ , where  $\omega$  is the angular frequency,  $c$  is the speed of light in vacuum, and  $\lambda$  is the free space wavelength. In Eq. (2.2.2),  $n^2 = \epsilon_r$  is the relative dielectric function, which is the mathematical representation of the actual waveguide structure, i.e., SIF or PCF. Eq. (2.2.2) is obtained by Fourier transform (FT) of Maxwell's equation, use of Eq. (2.1.3), and subsequent application of the curl operator. It is a hermitian eigenvalue problem, and is referred to as the *master equation* in [27], where it is treated extensively, because of its fundamental significance to electrodynamics. Once solved for the magnetic field, the electric field can be found from Maxwell's equations.

The diagrams in Fig. 2.2 show the calculation domains used when calculating the properties of SIFs (Fig. 2.2-left) and the truncated calculation domain used when calculating the properties of PCFs (Fig. 2.2-right). Only a quarter of the calculation domain is implemented since one can exploit the even and odd symmetry of the magnetic and electric fields, when the dielectric function has appropriate symmetry. Strictly speaking, it is most important to implement the quarter domain when calculating the properties of PCFs. The complicated structure of PCFs, containing many boundaries, lead to a very large number of elements for

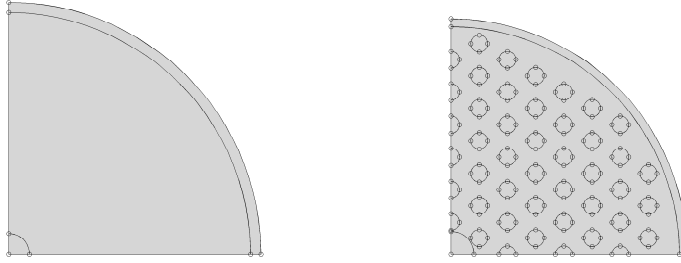


**Figure 2.2:** Example calculation domains for the FEM calculation in `Comsol`. Left: SIF Right: PCF.

the FEM calculation, and this in turn, leads to long calculation times and large memory consumption. The complexity is far less for the SIF. In Fig. 2.2-left, the inner circle marks the physical core domain of the SIF, while the largest domain is the cladding region. The outermost domain is a perfectly matched layer simulating a jacket material on the fiber. In Fig. 2.2-right the small domains represent the air holes, the smallest region centered at the origin, is artificial, and only used for approximating the fraction of light guided by the core. The large domain is the solid glass material, and the outer layer is a perfectly matched layer truncating the cladding domain.

Eq. (2.2.2) is solved in a wavelength loop traversing an entire range by specifying a single wavelength in each step of the loop. For each single wavelength then, the equation is solved by an iterative algorithm implemented by `Comsol`. The refractive index of the respective materials, composing the fiber is updated in each iteration, so material dispersion is correctly included in the calculation. The eigenvalue  $u$  yields the propagation constant  $\beta(\omega) = -\text{Im}(u)$ , and a guiding attenuation defined from Lambert Beer's law, and calculated as  $\alpha_g = -2\delta_z = -2\text{Re}(u)$ . Furthermore, the electric and magnetic fields distributions give the effective area for each wavelength, defined by [6, 28]

$$A_{\text{eff}} = \frac{(\int |\mathbf{E}(x, y)|^2 dx dy)^2}{\int |\mathbf{E}(x, y)|^4 dx dy} \quad (2.2.3)$$

where  $\mathbf{E}(x, y)$  is the transverse electric field profile. The denominator

above can be approximated by

$$\begin{aligned} |\mathbf{E}|^4 &= (\mathbf{E}\mathbf{E}^*)^2 = (|E_x|^2 + |E_y|^2 + |E_z|^2)^2 \\ &\approx |E_x|^4 + |E_y|^4 + |E_z|^4 \end{aligned} \quad (2.2.4)$$

for linearly polarized modes, because ideally, only one of the field components contain the entire field information. At a very early stage in the project, this approximative way of calculating the denominator in the effective area was implemented because only linearly polarized modes are considered. This was done even though the true approximation-free expression could equally well have been used without any noticeable change in computation time. It has been investigated, what are the implications of using the approximation, and as a representative of this, it can be mentioned that the relative difference in the effective area is  $\sim 0.006$  at  $\lambda = 15 \mu\text{m}$  in a  $2a = 20 \mu\text{m}$ ,  $\text{NA} = 0.5$  SIF, when comparing the approximation and the approximation-free expression. Furthermore it is found that the error increases with increasing wavelength and thus, the error of 0.006 represents the order of magnitude in the worst case considered here.

### 2.2.2 Dispersion of a Guided Mode

The propagation constant  $\beta = \beta(\omega)$ , or equivalently the effective refractive index  $n_{\text{eff}} = 2\pi\beta/\lambda$ , and the effective area  $A_{\text{eff}} = A_{\text{eff}}(\omega)$  of the guided mode, contain the information coupling the transverse and longitudinal parts of the pulse propagation problem. The effective area partly determine the nonlinear coefficient, (see Eq. (2.3.7)), while the propagation constant determine how light at different frequencies travel through the fiber. The dispersion properties of a waveguide is typically divided into two contributions, one contribution from the waveguide structure, and one from the material the waveguide is made from [18, 29]. As a rule of thumb, the waveguide dispersion increases with the amount of change caused to the bulk material by creating the waveguide. Thus, generally, the waveguide dispersion is smallest in a low index contrast SIF and increases via large index contrast SIFs over PCFs and to PBG guiding fibers where the waveguide dispersion is extreme. In the fibers considered here, the material dispersion enters through the frequency dependence of the refractive indexes,  $n(\omega)$ ,  $n_1(\omega)$  and  $n_2(\omega)$  as mentioned in the last section. Typically the refractive index of fiber materials are given in the form of a Sellmeier polynomial fit to measured data points, and generally

given by [6, 18]

$$n^2 = 1 + \sum_j \frac{A_j \lambda^2}{\lambda^2 - a_j^2}. \quad (2.2.5)$$

where parameters  $A_j$  and  $a_j$  can be found in the literature for various materials (see individual chapters 3, 4, and 5).

It must be noted at this point that whenever treating a SIF in this work, it has been assumed that the cladding material index ( $n_2$ ) has a dispersion determined by the appropriate Sellmeier equation, and that the core index ( $n_1$ ) is calculated from Eq. (2.2.1) using a given NA. Furthermore, the frequency dependence of the NA is ignored throughout, even though both  $n_1$  and  $n_2$  are functions of frequency.

Traditionally, one expands the propagation constant in a Taylor series, around an expansion frequency  $\omega_0$ , as

$$\beta(\omega) = \beta(\omega_0) + \sum_{j=1}^{\infty} \frac{1}{j!} \frac{d^j \beta}{d\omega^j} (\omega - \omega_0)^j \quad (2.2.6)$$

where the derivatives are also evaluated at  $\omega_0$ . Doing so allows for assessment of the significance of the individual terms in the expansion. Particularly  $\beta_1$  and  $\beta_2$  ( $\beta_j = d^j \beta / d\omega^j$ ) are mentionable. The group-velocity, i.e, the speed a light pulse travels down the fiber, is determined by  $\beta_1$  through

$$v_g = \frac{1}{\beta_1} \quad (2.2.7)$$

and knowledge of the group-velocity dispersion (GVD) parameter  $\beta_2$ , and in particular the location of the zero dispersion wavelength (ZDW), is important for the characteristics of SCG [14]. The GVD is often visualized in terms of the dispersion parameter,  $D$ , defined by [6]

$$D = -\frac{2\pi c \beta_2}{\lambda^2} = -\frac{c}{\lambda} \frac{d^2 n_{\text{eff}}}{d\lambda^2}. \quad (2.2.8)$$

It measures how much a pulse of a given spectral width broadens in time during propagation of the distance  $L$ . A large dispersion then, can be detrimental to a nonlinear process because it causes the content of a light pulse to diverge temporally, and thereby decreasing the field strength at a given instance of time. Particularly the ZDW wavelength, where  $\beta_2 =$

$D = 0$  is significant with respect to SCG, because it marks the boundary to the soliton dynamics regime (see section 2.4.2). For wavelengths with,  $D < 0$  ( $\beta_2 > 0$ ) the fiber is said to exhibit normal dispersion, and for wavelengths with  $D > 0$  ( $\beta_2 < 0$ ) the fiber is said to exhibit anomalous dispersion [6].

## 2.3 The Nonlinear Problem - Pulse Development

The longitudinal, or dynamical part, of the propagation problem presents itself in terms of the generalized nonlinear Schrödinger equation (GNLSE) for the complex electric field envelope development. The GNLSE has previously shown its applicability in modeling of SCG, and an extensive and well established review of the physics for SCG in silica PCFs is given in [14]. The derivation of the GNLSE is complicated but a comprehensive version is given in [6], where the equation is derived for the electric field envelope  $A = A(z, T)$ , with FT  $\tilde{A} = \tilde{A}(z, \omega)$ , normalized so that the instantaneous power in the electric field is [23]

$$P(T) = |A(T)|^2, \quad \text{with energy } E = \int |A(T)|^2 dT. \quad (2.3.1)$$

In this work however, a slightly different version of the GNLSE, than derived in [6] and reviewed in [14], is solved.

Before proceeding, a few notes are made to the reader at this point. The following definition for the FT and inverse Fourier Transform (iFT)

$$\tilde{f}(\omega) = \int f(t) e^{i\omega t} dt \quad \text{and} \quad f(t) = \frac{1}{2\pi} \int \tilde{f}(\omega) e^{-i\omega t} d\omega \quad (2.3.2)$$

are used throughout. Generally, in this work, integration with no boundaries specified is implied to mean integration from  $-\infty$  to  $\infty$ , i.e.,  $\int = \int_{-\infty}^{\infty}$  over whichever integration variable is in question. A review of the FT properties that are useful in connection to the GNLSE is given in appendix C page 107.

The GNLSE solved here, is based on a derivation by J. Lægsgaard [17] that explicitly includes the frequency dependence of the effective area. This is needed, because the effective area variation can be large over the wavelength range of interest for SCG in the mid-IR. The derivation leads to a slightly different version of the GNLSE than found in [6], and now

for the pseudo electric field envelope in the frequency domain  $\tilde{C}(z, \omega)$ , obtained from the frequency domain electric field envelope  $\tilde{A}$  by

$$\tilde{C} = \left[ \frac{A_{\text{eff}}}{A_{\text{eff}}(\omega_0)} \right]^{-\frac{1}{4}} \tilde{A}. \quad (2.3.3)$$

Furthermore, the GNLSE is transformed into the interaction picture (IAP) (see appendix A page 95) introduced by J. Hult [30] that requires the following definition

$$\tilde{C}_I = e^{-\tilde{L}z} \tilde{C} \quad (2.3.4)$$

where  $\tilde{C}_I$  is the pseudo electric field envelope in the frequency domain and IAP. It can be shown that the GNLSE can then be written as [31]

$$\begin{aligned} \frac{\partial \tilde{C}_I}{\partial z} = i\bar{\gamma}(\omega) e^{-z\tilde{L}} \left[ 1 + \frac{\omega - \omega_0}{\omega_0} \right] \times \\ \mathcal{F} \left\{ C \mathcal{F}^{-1} \left\{ \tilde{R}(\omega - \omega_0) \mathcal{F} \{ |C(T)|^2 \} \right\} \right\} \end{aligned} \quad (2.3.5)$$

or written very compactly, as it is presented in [32, 33]

$$\frac{\partial \tilde{C}_I}{\partial z} = i\bar{\gamma} \frac{\omega}{\omega_0} e^{\tilde{L}z} \mathcal{F} \left\{ C \mathcal{F}^{-1} \left\{ \tilde{R} \mathcal{F} \{ |C|^2 \} \right\} \right\} \quad (2.3.6)$$

where  $\mathcal{F} \{ \cdot \}$  denotes the FT. In this version of the GNLSE, the nonlinear coefficient is

$$\bar{\gamma} = \bar{\gamma}(\omega) = \frac{\omega_0 n_2 n_{\text{eff}}(\omega_0)}{c n_{\text{eff}} \sqrt{A_{\text{eff}} A_{\text{eff}}(\omega_0)}} \quad (2.3.7)$$

where  $n_2$  is the nonlinear refractive index of the fiber material and  $c$  is the speed of light in vacuum. The function  $\tilde{R}$  in Eq. (2.3.6) is the FT of the response function  $R(T)$  that includes both the instantaneous electronic response and the delayed molecular vibrational response (delayed Raman response) of the material. The linear operator is given by

$$\tilde{L} = \tilde{L}(\omega) = i \{ \beta(\omega) - [\beta(\omega_0) + \beta_1(\omega_p)(\omega - \omega_0)] \} - \frac{\alpha(\omega)}{2} \quad (2.3.8)$$

where  $\beta(\omega)$  is the propagation constant found from the transverse part of the propagation problem,  $\omega_0$  is the center frequency in the calculation domain (expansion frequency, see appendix D page 119),  $\omega_p$  is the frequency



of the pump source, and  $\alpha(\omega)$  is the total power attenuation. Notice that the pump frequency, which is generally different from the expansion frequency to allow the calculation domain to extend to wavelengths below half the pump wavelength, introduces a retarded time frame  $T$  that moves with the group-velocity  $v_g$  at the pump frequency. The formal derivation of this is given in appendix E page 123.

Notice that if the frequency dependence of the effective area and the effective index is ignored then

$$\tilde{C} = \tilde{A} \quad \text{and} \quad \bar{\gamma} = \frac{\omega_0 n_2}{c A_{\text{eff}}(\omega_0)} = \gamma \quad (2.3.9)$$

where  $\gamma$  is the, perhaps more familiar, nonlinear coefficient in the GNLSE derived in [6] and reviewed in [14]. In all numerical simulations of experimental conditions is used a chirp free input pulse given by a Gaussian shaped pump pulse (see Eq. (C.1.3)) of the form

$$A(0, T) = \sqrt{P_0} e^{-\frac{T^2}{2T_0^2}} + \text{OPPM} \quad (2.3.10)$$

as the initial condition, where  $P_0$  is the peak power and  $T_0$  is the temporal width of the pulse ( $T_0 = T_{\text{FWHM}}/(2\sqrt{\ln 2})$ ). The last term in Eq. (2.3.10) represents the one-photon-per-mode (OPPM) noise model that is used to model spectral fluctuations from shot-to-shot in the input pulse [14, 31]. The electric field is obtained from the envelope function by multiplication of a fast varying phase factor with a frequency corresponding to the central carrier wavelength, or here, pump wavelength  $\lambda_p = 2\pi c/\omega_p$ .

The GNLSE is solved using a fourth order Runge-Kutta integration scheme with adaptive step size [34], where the error accumulation is controlled by the local goal error method [35]. It can be shown that if loss is neglected, and the waveguide maintains its dispersion properties along its length (i.e. no fiber taper, etc.) the version of the GNLSE derived in [6] conserves a quantity called the photon number [36]. The introduction of the pseudo electric field envelope  $\tilde{C}$  warrants a small correction to the conserved quantity that becomes

$$P_N(z) = \frac{c\sqrt{A_{\text{eff}}(\omega_0)}}{n_2 n_{\text{eff}}(\omega_0)} \int n_{\text{eff}} \sqrt{A_{\text{eff}}} \frac{|\tilde{C}_I|^2}{\omega} d\omega \quad (2.3.11)$$

and the formal derivation of this, is given in detail in appendix F page 127. The conservation of the quantity in Eq. (2.3.11) is used to check the implementation of Eq. (2.3.5). The conservation is quantified through

the photon number error, given by  $\text{Err}(z) = |(P_N(z) - P_N(0))/P_N(0)|$ , and its development is investigated for a simulation where loss and noise is ignored.

### 2.3.1 Interpreting Results from Simulations

When a result is obtained from a simulation of the GNLSE, it is given in terms of a single-shot of the frequency domain pseudo electric field envelope in the IAP,  $\tilde{C}_I$ , which is then transformed to the complex electric field envelope  $\tilde{A}$  according to the transformation rule in Eq. (2.3.3). To visualize calculated spectra, however, the complex electric field envelope is plotted in terms of the energy spectral density (ESD) or equivalently the power spectral density (PSD) in the wavelength domain. These are calculated as

$$\text{ESD}(z, \lambda) = \frac{c}{\lambda^2} |\tilde{A}(z, \lambda)|^2 \quad \text{and} \quad \text{PSD} = f_{\text{rep}} \text{ESD}, \quad (2.3.12)$$

respectively, where  $f_{\text{rep}}$  is the seed laser repetition rate (see appendix C page 107).

A single-shot simulation, in this respect, means a single solution obtained from a simulation where the initial condition is imposed with one instance of random noise given by the OPPM-model from Eq. (2.3.10). This noise is imposed on the initial condition to model spectral fluctuations from shot-to-shot present in the seed laser. A typical spectrometer in a measurement setup will smooth such fluctuations in a measured result, because the spectrometer has a finite wavelength resolution, and all light in a wavelength region of width  $\Delta\lambda_{\text{res}}$  around the discrete measurement wavelength  $\lambda$  will be reported as corresponding to it. Furthermore, a typical data acquisition apparatus has a finite integration time  $\tau_{\text{int}} \gg 1/f_{\text{rep}}$ , and a measured spectrum is also correspondingly averaged over a number of consecutive shots from the seed laser. With a typical value of  $f_{\text{rep}} \sim 10$  MHz and, for example, an integration time of  $\tau_{\text{int}} = 100$  ms, a measured spectrum corresponds to an average over some  $10^4$  shots of the seed laser. If the repetition rate is on the order of kHz instead, the average typically corresponds to an order of hundreds of shots.

To mimic the finite spectrometer resolution, simulations of the GNLSE, which are directly comparable to laboratory measurements, are averaged using a rectangular box of width  $\Delta\lambda_{\text{res}} = 10$  nm for each realization of the noise seed, and afterwards ensemble averaged over a number of individual simulations to emulate the finite integration time. Hundreds to

tens-of-thousands of shots, however, will cause a tremendous amount of computer load, so in this work is used 30 shots in ensemble averages.

## 2.4 Propagation Effects in Nonlinear Optics

In this section a few key effects, often observed in nonlinear fiber optics, are introduced because they will be referred to in the following chapters. The descriptions are kept brief for convenient reference during later chapters.

### 2.4.1 Self-phase Modulation

The first effect to describe is self-phase modulation (SPM), where a propagating pulse modifies its own phase due to the nonlinear refractive index  $n_2$  of the fiber material. The equation that isolates this particular effect is the nonlinear Schrödinger equation (NLSE) [6]

$$\partial_z A = i\gamma|A|^2 A \quad (2.4.1)$$

where dispersive effects are neglected. This equation is obtained from Eq. (2.3.5) by assuming the frequency dependence of  $n_{\text{eff}}$  and  $A_{\text{eff}}$  can be ignored, by assuming a purely instantaneous material response, ignoring the optical shock effect, and ignoring loss.

By multiplication of the complex conjugate  $A^*$ , and adding the complex conjugate of the obtained result, it can be shown that the power  $P = |A|^2$  is a constant with regards to  $z$ , and one can derive that the electric field envelope solution is

$$A(z, T) = A(0, T)e^{i\gamma|A(0, T)|^2 z}. \quad (2.4.2)$$

From the phase factor in the solution, it is seen that the pulse itself induces a change to the phase of the input  $A(0, T)$ , and this causes the name, self-phase modulation. The phase change, however, do not influence the power distribution, while in the frequency domain, the effect of SPM is more complicated. It can be shown that SPM lowers the instantaneous frequency in the beginning of the pulse (leading edge) and increase the instantaneous frequency at the end of the pulse (trailing edge), which is generally referred to as a chirp across the pulse [6]. SPM manifests itself quite clearly in the frequency domain as a number of ripples on the ESD, symmetrically growing around the center frequency, as

the pulse propagates down the fiber, and consequently broadening it spectrally. Figs. 3.9-right and 3.10-right in chapter 3, show examples of SPM broadening, though here, the optical shock effect causes an asymmetry to the ripples. SPM is typically observed in the early stages of SCG.

### 2.4.2 Solitons

It can be shown that if the NLSE includes GVD  $\beta_2$ , so that Eq. (2.4.1) is modified to become [6]

$$\frac{\partial A}{\partial z} = -i\frac{\beta_2}{2}\frac{\partial^2 A}{\partial T^2} + i\gamma|A|^2 A \quad (2.4.3)$$

then one of its possible solutions is,

$$A(z, T) = \sqrt{P_0} \text{sech}\left(\frac{T}{T_0}\right) e^{-i\frac{|\beta_2|z}{2T_0^2}}$$

with FT  $\tilde{A}(z, \omega) = \pi T_0 \sqrt{P_0} \text{sech}\left(\frac{\omega \pi T_0}{2}\right) e^{-i\frac{|\beta_2|z}{2T_0^2}}$  (2.4.4)

if the peak power  $P_0$  and pulse width  $T_0$  is adjusted so that  $P_0 = |\beta_2|/(\gamma T_0^2)$ , and  $\beta_2 < 0$  (or  $D > 0$ ), so dispersion is anomalous. The solution (2.4.4) is called a fundamental soliton and it has the property that neither the power distribution  $|A(T)|^2$  nor the ESD  $|\tilde{A}(\omega)|^2$  change during propagation, physically because GVD and SPM counteract each other.

The fundamental soliton is one out of an infinite amount of solutions of (2.4.3) [6] characterized by the soliton number

$$N = \sqrt{\frac{L_D}{L_{NL}}} = \sqrt{\frac{\gamma P_0 T_0^2}{|\beta_2|}} = \sqrt{\frac{n_2 \omega_{\text{sol}}}{c A_{\text{eff}}(\omega_{\text{sol}})} \frac{P_0 T_0^2}{|\beta_2(\omega_{\text{sol}})|}} \quad (2.4.5)$$

where  $L_D = T_0^2/|\beta_2|$  is the dispersion length and  $L_{NL} = 1/(\gamma P_0)$  is the nonlinear length. If  $L_D \gg L_{NL}$  nonlinear effects will dominate the propagation, while if  $L_{NL} \gg L_D$  linear dispersive effects dominate. For the fundamental soliton, the peak power and pulse width is adjusted so that  $N = 1$ , while if they are adjusted so  $N \geq 2$ , then a higher order soliton is excited in the fiber. Higher order solitons do not propagate without changing shape as the fundamental soliton does, but under idealized conditions, as described by Eq. (2.4.3), they change shape in a periodic manner, thereby recovering their initial shape once each period. During SCG though, the governing equation is the full GNLSE, and the periodic dynamics is lost. An energetic seed laser in the anomalous dispersion

regime, can result in a large initial soliton number, and subsequently, the spectrum typically develops through pulse breakup, into a number of fundamental solitons that are often individually distinguishable in a well developed SC spectrum [14, 37].

### 2.4.3 Four-wave Mixing

The process of FWM is the nonlinear effect that caused the spectral broadening in the first SC observation [15]. In the process, two photons are annihilated, and two other photons are created while the total energy and momentum is conserved. The momentum conservation imposes a phase-matching condition on the FWM-process that determines the boundaries of the gain bands for degenerated FWM [38]

$$g(\lambda) = \text{Re} \left( \sqrt{-\Delta\beta \left[ \frac{\Delta\beta}{4} + \gamma P_0 \right]} \right) \quad (2.4.6)$$

where  $\Delta\beta = \Delta\beta(\lambda) = \beta(\lambda) + \beta(2\lambda_p - \lambda) - 2\beta(\lambda_p)$  is the accumulated difference between the phase of the signal, at wavelength  $\lambda$ , the idler at wavelength  $2\lambda_p - \lambda$ , and the pump. In degenerate FWM, where the annihilated photons are from the same pump, the gain bands are symmetrically placed in frequency on either side of the pump. The low (high) frequency gain band is called the (anti) Stokes band. FWM find applications in, e.g., optical parametric amplifiers [38], wavelength conversion [39], or a small niche application has been proposed, where FWM is used in a biosensor made from a PCF [40].

A typical feature of degenerate FWM is that when the pump is in the anomalous dispersion regime, the gain bands are wide and continuously connected across the pump, while the gain bands are narrow and separated from the pump, when it is in the normal dispersion regime [14]. In the time domain, FWM manifests itself as an instability of the power distribution amplitude as the pulse develops. The term modulation instability (MI) is used for this time domain analogue to FWM.

### 2.4.4 Effects From Delayed Raman Response

In the full GNLSE, the delayed response from the fiber material to an applied electric field, is included through the convolution term in (2.3.5). The response function is generally written on the form [6]

$$\tilde{R}(T) = (1 - f_R)\delta(T) + f_R h_R(T) \quad (2.4.7)$$

where the first term accounts for the instantaneous part of the material response, and  $\delta(T)$  is Dirac's delta-function. The second term is the delayed Raman response, described by  $h_R(T)$ , and  $f_R$  is the fractional Raman contribution. The delayed Raman response function  $h_R(T)$ , is derived from the Raman gain profile  $g_R(\Omega)$  in the specific fiber material, and the conversion from a measurement of the gain profile and to the mathematical function  $h_R(T)$  is reviewed in detail in appendix G page 133. Briefly summarized, the delayed material function is found from the equation [6]

$$g_R(\Omega) = 2\gamma f_R \text{Im} \left( \tilde{h}_R(\Omega) \right) \quad (2.4.8)$$

where  $\tilde{h}_R(\Omega)$  is the FT of  $h_R(T)$  and the fractional Raman contribution  $f_R$ , is found by imposing a normalization on  $h_R(T)$  so that  $\int h_R(T) dT = 1$ . In chapter 3 is presented the result of two measurements of the delayed Raman gain in ZBLAN that are compared, and also in chapters 4 and 5 are shown examples of the Raman response function for tellurite and chalcogenide respectively. In order to analyse the magnitude of different Raman gains, the quantity

$$f_R \text{Im} \left( \tilde{h}_R(\Omega) \right) = \frac{g_R(\Omega)}{2\gamma} \quad (2.4.9)$$

is compared, because  $g_R(\Omega)/(2\gamma)$  is the delayed Raman gain per effective nonlinearity. Thus, the left-hand side (LHS) above represents the magnitude of the delayed Raman gain, for a given fiber and a given pump that determines the nonlinearity, thus enabling comparisons of different Raman gain spectra.

The delayed Raman response establishes a gain region, which is responsible both for amplification, either spontaneous or stimulated, of light in the gain band, and can form a cascade of Stokes shifted lines in a laser spectrum [41]. Also, importantly in relation to SCG, is intra pulse Raman scattering, often called soliton self-frequency shift (SSFS) [42, 43]. This causes solitons to continuously shift their center frequency towards lower frequencies (red shift) because energy is transferred from the high energy part of the pulse spectrum to the lower energy part. This process is vital to the long wavelength edge of generated SC [14]. An example of a Raman gain is displayed in Fig. 3.5-left, and the SSFS is observed in Fig. 3.8 both from chapter 3.

### 2.4.5 Higher Order Dispersion

Higher order dispersion enters the NLSE by including more terms from the Taylor expansion in Eq. (2.2.6) than just the GVD  $\beta_2$ . In the full GNLSE all orders of dispersion are included through the definition of the linear operator in Eq. (2.3.8). Higher order dispersion perturbs the idealized soliton solutions of the NLSE, and particularly it causes higher order solitons to fission into their constituent fundamental solitons [14, 37], instead of allowing the periodic behaviour observed in idealized higher order solitons. This soliton fission process is particularly prominent for ultra fast fs-pulses, and is gradually replaced by SPM and FWM/MI caused breakup for longer pulses [14]. Furthermore, higher order dispersion enables a resonant energy transfer between a soliton redshifting due to the SSFS and a phase-matched wave in the normal dispersion regime [14], often denoted a dispersive wave or non-solitonic radiation [37]. The dispersive wave and a redshifting soliton are related through a potential that trap a redshifting soliton and blue shifted dispersive radiation together [44].

## 2.5 Summary of Chapter 2

In this chapter, the electrodynamic model used to simulate SCG is introduced, and it has been argued that the nonlinear pulse propagation problem is divided into two separate problems connected through the propagation constant  $\beta(\omega)$  and the effective area  $A_{\text{eff}}(\omega)$  of the fiber mode. In this respect, the two kinds of fiber optical waveguides considered during the remainder of this work are introduced. The most extensively used fiber type in the following is the SIF, but also the PCF is discussed and such fibers are considered in chapter 4. The propagation constant and the effective area are initially calculated using a commercially available FEM software package, before they are used in solving the GNLSE. The FEM calculation includes the material refractive index wavelength dependence by solving the transverse problem in an iterative manner over a range of wavelengths and using the appropriate value of the refractive index in each iteration. After introducing the transverse problem, the first two terms of the Taylor expansion of the propagation constant are given a little special attention. The first term containing  $\beta_1$ , signifying the group-velocity of a pulse travelling in the fiber, and the second term contains the GVD parameter  $\beta_2$ . The GVD parameter mark the boundary between normal

and anomalous dispersion regimes.

Continuing onwards from the transverse problem, the generalized nonlinear Schrödinger equation is introduced. The GNLSE is the nonlinear differential equation, describing the development of the electric field envelope, as a pulse travel down a fiber with a large effective nonlinearity. The version of the GNLSE solved in this work is based on a derivation by J. Lægsgaard that is further transformed into the IAP. It treats SCG in a single mode of the optical fiber, and this mode is always the fundamental mode in the present work. It is discussed how results from individually calculated spectra imposed with random noise, are averaged to emulate spectral fluctuations from a seed laser system, the finite wavelength resolution of a typical spectrometer and finite integration time of a data acquisition device.

Finally, a few of the most relevant isolated nonlinear effects and concepts are reviewed for reference in following chapters along with a brief mention of higher order dispersion influence on SCG. In the following chapters the theory is put into practice when simulating SCG in soft-glass fibers made from ZBLAN in chapter 3, ZBLAN and tellurite in chapter 4 and chalcogenide in chapter 5.





## Chapter 3

# Supercontinuum in a ZBLAN Soft-glass Fiber

From the onset of this project,  $\text{ZrF}_4\text{BaF}_2\text{LaF}_3\text{AlF}_3\text{NaF}$  (ZBLAN) was a natural choice to investigate as fiber material for a nonlinear fiber in an infrared (IR) SC source. The soft-glass is a fluor based composite glass material, and it has a nonlinear refractive index of  $n_2 \sim 2.2 \cdot 10^{-20} \text{ m}^2/\text{W}$  [7, 45], which is comparable to silica [6], whereas the transmission window of ZBLAN stretches significantly longer into the IR, due to lower phonon energy than that of silica [5, 26, 46]. Compared to silica though, ZBLAN is a much less well documented material.

The first challenge experienced during this work, in the endeavour to aid in obtaining a ZBLAN based mid-IR SC source, then, was to determine the material refractive index profile for ZBLAN, and because no measurement of the full profile of the delayed Raman response was available, perform such a measurement. Accurate information, particularly regarding the nonlinear refractive index, the delayed Raman response, and the dispersion properties of the fiber material, are essential in order to obtain reliable results from numerical modeling, which in turn is important, when the aim is to suggest a suitable nonlinear fiber for a SC source.

After obtaining information about the material itself, the second challenge was to measure and simulate SCG in a ZBLAN fiber using both normal and anomalous dispersion regime pumping. The achievable spectral widths from SCG can depend drastically on the pumping regime used, and so, it is important to establish what regime a pump system must aim at. Particularly a thulium (Tm) doped fiber laser, that has an emission wave-

length around  $2\text{ }\mu\text{m}$ , could initially seem like a viable source. Tm sources however, are less wide spread than erbium (Er) or ytterbium (Yb) doped fiber lasers, and thus more problematic to implement in a commercial system. Some recent publications on IR SC do focus on Yb or Er pump lasers, but based on a cascade of a silica fiber and a soft-glass fiber [47,48]. The SC is then initially generated in the silica fiber and then coupled into a soft-glass fiber that pushes the SC further into the IR. However, such coupling between nonlinear fibers, for improved redshift of solitons, pose requirements on the matching of the dispersion and nonlinear properties of the fibers [32,49], and this is discussed in chapter 4.

This chapter reviews the road from start, at a material name and a few available fibers, out of which one in particular was subject to massive testing, over measurement of the delayed Raman response, through simulations and measurements of full scale SCG, to an application and the final prototype product developed and created by our collaborators at NKT Photonics. The chapter is organized as follows: In section 3.1, available literature on the ZBLAN material properties is reviewed, and special emphasis is on material dispersion properties and attenuation. Also a measurement of the dispersion in an existing fiber is presented here. Then, in section 3.2 a measurement of the delayed Raman response in a ZBLAN fiber is presented, and it is compared to existing measurements of the Raman gain in ZBLAN. In section 3.3.1 the experimental setup for SC measurements is presented, and in section 3.3.2 measurements and simulations of SCG are compared. At the end of section 3.3, the debate about the delayed Raman response in ZBLAN from section 3.2 is shortly revisited. In section 3.4 a few suggestions for important considerations to be made when designing a SC source are put forward. Then, finally, in section 3.5 is presented an application for IR SC, developed by our collaborators from Aarhus University (AU), and last but not least, the celebrated overall outcome of the total collaboration, this project has been part of, is presented in section 3.6.

### 3.1 ZBLAN Optical Properties

Because ZBLAN is a composite glass, material dispersion can vary between manufacturers and even between production batches, from the same manufacturer, and this makes it hard to find accurate data describing its optical properties. Thus, a literature study was initiated early on, in the search for material parameters. Firstly, a measurement

of the material dispersion of ZBLA and ZBLAN was performed on bulk prisms by Brown *et al.* in 1985, where the refractive index curve is presented as a Wemple equation [50]. In this period, ZBLAN fibers were investigated for use as mainstream fibers in optical communications, at longer wavelengths than silica based fibers, but background attenuation levels were too high, above 4 dB/km [50] (even though lower loss was also reported, at wavelengths close to/inside the transmission window of silica [51]). The refractive index dispersion of ZBLAN reported in [50] resembles the shape of the material dispersion from another measurement, performed by F. Gan [52] ten years later in 1995, though shifted upwards to higher absolute values. Also in [50] it is illustrated that the absolute values of the refractive index are highly dependent on the amount of sodium (Na) in the ZBLAN. Compositional differences between [50] and [52] might explain the differences between the index values. In [53] Wetenkamp *et al.* also perform measurements on different bulk prism ingots, made from ZBLAN, with slightly changing compositions. The compositional changes result in vertical translation of the absolute value of the refractive index curve, but only small changes to the shape of the profile. The final paper to draw out in this respect, was already mentioned above, is a 1995 paper by F. Gan [52]. This review-paper reports the optical properties of multiple fluoride glasses, and presents refractive index profiles in terms of Sellmeier polynomials (see chapter 2). Finally a measurement by a fiber manufacturer, also giving a Sellmeier equation, has been obtained from iRphotonics [54]. To summarize the findings, the

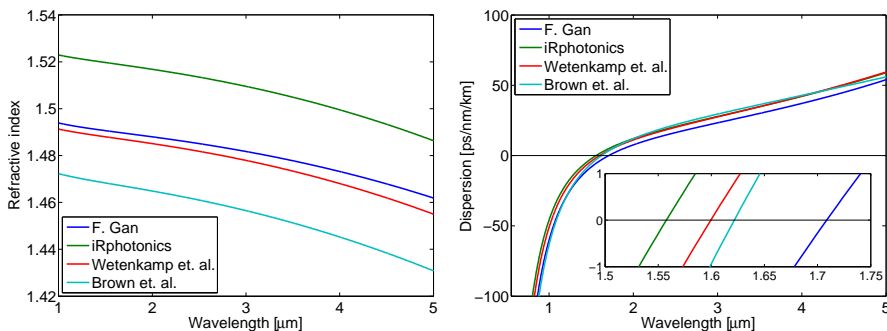


**Figure 3.1:** Left: Material refractive index profiles for ZBLAN from different measurements reported in literature and by one manufacturer of ZBLAN fibers. Right: Bulk dispersion calculated for the index profiles shown in the left panel. The inset shows a zoom at the ZD crossings.

index profiles are shown in Fig. 3.1-left, and here it is clearly seen how the different measurements show similar shapes, while the absolute values are different. The bulk ZDWs are calculated to be (see Eq. (2.2.8))

$$\begin{aligned} \text{F. Gan [52]: } \lambda_{\text{ZD}} &= 1.71 \text{ } \mu\text{m}, \\ \text{iRphotonics [54]: } \lambda_{\text{ZD}} &= 1.56 \text{ } \mu\text{m}, \\ \text{Wetenkamp } et al. [53]: \lambda_{\text{ZD}} &= 1.60 \text{ } \mu\text{m}, \\ \text{Brown } et al. [50]: \lambda_{\text{ZD}} &= 1.62 \text{ } \mu\text{m} \end{aligned}$$

respectively. There is a spread of  $\sim 150$  nm between the largest and the smallest of these possible material ZDWs. The significance of an uncertainty in the location of the ZDW is discussed in section 3.3.

As mentioned earlier, background losses in ZBLAN were measured to have a level of more than 4 dB/km [50], and even though fibers with such an attenuation are less suited for long haul optical communications, in competition with fused silica that has a minimum loss of  $\sim 0.2$  dB/km [6], it is a reasonable loss for SCG, where fiber lengths are on the order of meters. A measurement of the total attenuation  $\alpha = \alpha(\omega)$  for a drawn SIF is provided by FiberLabs [46], and it is shown in black in Fig. 3.2 [46]. This loss curve, which generally shows a loss level around 50 dB/km is measured soon after fiber drawing and the loss data between 700 nm and 3200 nm was measured by the cutback method for a multi-mode ZBLAN fiber. The values for wavelengths longer than  $3.2 \text{ } \mu\text{m}$  and shorter than 700 nm were estimated values [46]. The measurement resolution was 20 nm, but some degree of uncertainty is to be expected according to the manufacturer [46]. Similar to the measurement in Fig. 3.2, reference [5] shows a summary (Fig. 2 in [5]) of the multiphonon edge for different soft-glasses, where the loss edge rises abruptly around  $4.5 \text{ } \mu\text{m}$  for ZBLAN. Similarly the loss of ZBLAN is reported to increase after  $4 \text{ } \mu\text{m}$  in [55]. Even though a strict definition of a loss boundary preventing SCG from developing further into the IR is not exactly well defined, the tendency in the loss measurements in [5,55] and by FiberLabs [46] are clear. Loss rises sharply after a wavelength of around  $4 \text{ } \mu\text{m}$ , and will start to dominate a SCG process around  $4.5 \text{ } \mu\text{m}$ . Thus, a priori, one should not expect SC to develop much further into the IR than  $\sim 4.5 \text{ } \mu\text{m}$  in ZBLAN, just as the fused silica based SC sources, does not go beyond  $\sim 2.4 \text{ } \mu\text{m}$ .

Based on deficiencies between experiment and simulations, that will be presented in section 3.3.2, it is suspected that an attenuation band starting around  $2.7 \text{ } \mu\text{m}$  is present in experiments that is not accounted for by the measured (black) loss curve in Fig. 3.2, which is the default

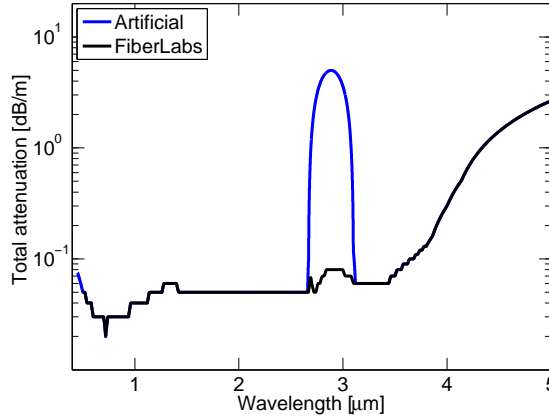


**Figure 3.2:** Black solid line is measured absorption in a multimode fiber (courtesy FiberLabs [46]), and blue is a loss profile with an artificially enhanced loss band, simulating a large absorption boundary due to an OH-stretch.

loss profile implemented in calculations. Furthermore, it is suspected that exactly such an attenuation band can be caused by water (OH) intruding the fiber, since water is known to cause absorption peaks in this particular wavelength range in fluoride based fibers [56, 57]. To examine this, an artificial loss peak is added to the measured loss, and simulations are redone (see section 3.3.2). This is one of the strengths of numerical simulations that the influence of significant quantities can be investigated without time consuming laboratory experiments, and a guesstimate for their impact can be made. Both Gaussian and parabolic band shaped additions of different peak values, and widths, have been investigated by rerunning simulations. It was found that a parabolic shaped loss (shown in blue in Fig. 3.2) with a peak value of 5 dB/m, coinciding with the small peak of the experimental loss curve, i.e., centered at  $2.9 \mu\text{m}$ , will give simulation results (shown in blue in the right panels of Figs. 3.12, 3.13, 3.16 and 3.17) that support the long wavelength edge trends exhibited by our measured PSDs.

### 3.1.1 A Particular ZBLAN Fiber

As reviewed in the last section, different possible descriptions of the refractive index wavelength dependence in ZBLAN are available. As discussed, these differences can, at least partly, be ascribed to different material

compositions, and it was not possible to find a profile that predicted the dispersion profile of all the fibers investigated during this project with complete accuracy. At one point in time though, a choice had to be made about what dispersion profile to continue working with. The finally accepted compromise was the most recent literature report by F. Gan [52].

To help substantiate that the material dispersion measured by F. Gan [52] is suitable to describe the dispersion properties of various ZBLAN fibers, imaginable for SCG, a numerical calculation, and a measurement on an existing fiber dispersion is compared. The fiber is the one presented in [33,58], and it is a commercially available ZBLAN (53%ZrF<sub>4</sub>-29%BaF<sub>2</sub>-3%LaF<sub>3</sub>-3%AlF<sub>3</sub>-12%NaF) SIF, with a core diameter  $2a = 10.7 \mu\text{m}$ , and a numerical aperture of  $\text{NA} = 0.20$  made by FiberLabs<sup>1</sup>. It is also the fiber used during measurement of the delayed Raman response [59] (see section 3.2) and during measurement of SCG [33] (see section 3.3). As mentioned earlier, the NA is considered independent of frequency, and this is also proposed by the fiber manufacturer [46]. The guiding loss and effective area found using Comsol (see chapter 2) is plotted in Fig. 3.3-right (a) and (b). The effective area increases by approximately a factor of 4 between 1 and  $4.5 \mu\text{m}$ , underlining the necessity of using a version

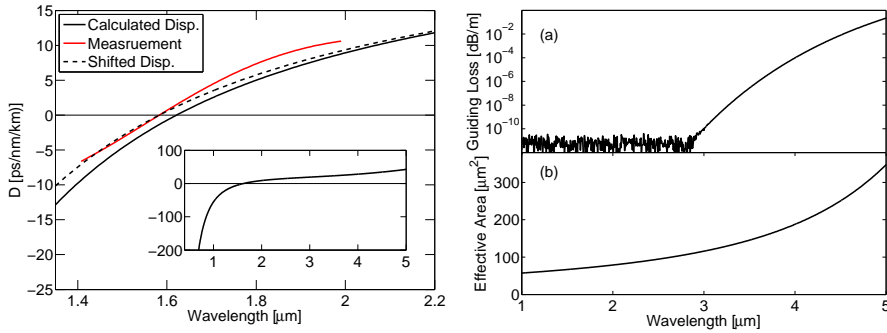


**Figure 3.3:** Left: Dispersion of the  $2a = 10.7 \mu\text{m}$ ,  $\text{NA} = 0.2$  ZBLAN fiber from FiberLabs. Black curve is calculated using Comsol and F. Gan [52] Sellmeier data, and red curve is measurement performed by H. Steffensen in collaboration with J. K. Lyngsøe of NKT Photonics. The inset shows the full calculated dispersion profile. Dashed line is the wavelength shifted dispersion curve discussed in section 3.1.1. Right: (a) Guiding loss and (b) effective area as function of wavelength for the same fiber as in left panel, calculated using Comsol.

<sup>1</sup>FiberLabs, product code: 03B-2-3(09C-27). Other manufacturers of ZBLAN fibers are, e.g., iRphotonics (Canada) or Le Verre Fluoré (France).

of the GNLSE that includes frequency dependence of the effective area for modeling broad band IR SC. The guiding loss starts to grow from numerical noise at roughly  $2.85 \mu\text{m}$  but for this fiber, it never dominates the loss curve shown in Fig. 3.2.

The dispersion measurement was made using an interferometric procedure [60] but, due to source and spectrometer limitations, it was done in a smaller wavelength region than the one of total interest for SCG. In a sense, one could argue that the dispersion measurement needs the light source, the measurement helps to achieve. The measured dispersion profile is shown in red in Fig. 3.3-left where the calculation, based on Sellmeier properties from F. Gan [52], is plotted in solid black. The dispersion measurement has some degree of uncertainty because the fiber is multi-moded below  $2.8 \mu\text{m}$  (see chapter 2.2 page 9). This uncertainty, along with the possible discrepancy between the fiber material and the literature reported refractive index wavelength dependence is manifested clearly in Fig. 3.3-left. The calculated ZDW is  $\lambda_{\text{ZD}}^c = 1.62 \mu\text{m}$ , while the measured is  $\lambda_{\text{ZD}}^m = 1.58 \mu\text{m}$ . In 1985 was published a letter by Monerie *et al.* [51] that measured the dispersion of the fundamental mode in a comparable ZBLAN SIF, with a NA of approximately  $0.175 - 0.180$ , and a core diameter of  $2a = 10 \mu\text{m}$ . The waveguide dispersion of this fiber is slightly weaker, than in our  $10.7 \mu\text{m}$  fiber, but the ZDW is still reported to be  $1.64 \mu\text{m}$ , or close to the value calculated for our fiber using F. Gan Sellmeier data.

Clearly, there is a discrepancy between measurements and predicted values of fiber ZDWs when considering ZBLAN, but during simulations of SCG, the difference of approximately  $\lambda_s = \lambda_{\text{ZD}}^c - \lambda_{\text{ZD}}^m = 40 \text{ nm}$  is addressed. This is done by also considering a second dispersion profile than the one found from the `Comsol` calculation. This second, and artificial dispersion profile, is found by shifting the calculated profile, such as to have a ZDW that coincides with the measured one, while having same shape as the `Comsol` curve. This is achieved by defining a wavelength shifted propagation constant  $\beta' = \beta'(\omega) = \omega n'_{\text{eff}}(\omega)/c$  where  $n'_{\text{eff}} = n_{\text{eff}}(\lambda + \lambda_s)$  is the corresponding wavelength shifted effective refractive index. Both the calculated propagation constant, and the wavelength shifted propagation constant is used in simulations, so as to investigate the influence of ZDW discrepancies. The dispersion profile calculated from the wavelength shifted effective refractive index is displayed as the black dashed line in Fig. 3.3-left.



## 3.2 Delayed Raman Response in the ZBLAN Fiber

As mentioned in chapter 2, that introduces the GNLSE, the delayed Raman response is another important input for prediction of SCG. Measurement of the Raman gain profile, originating from the delayed material response, however, is far from trivial, and only scarce and partial literature reports were available for the Raman gain in ZBLAN at the start of this project. Furthermore, these partial measurements do not agree on the magnitude of the effect, and finally reports of simulations of SCG in ZBLAN, most often do not quote a Raman response, even though it is stated one has been included in calculations. Thus no full Raman gain profile was documented when this work began, and this lack of a suitable expression to incorporate in the GNLSE lead to the measurement of the delayed Raman response presented in this section.

Before reviewing the results from the measurement though, it is beneficial to create an overview of existing literature [33] on Raman gain in ZBLAN. The Raman response in bulk samples of binary compositions of fluorozirconate glass ( $\text{ZrF}_4\text{-BaF}_2$ ) was analysed in 1981 in [61], and a strong Raman gain was identified between 17.0 and 17.9 THz, depending on the content of  $\text{ZrF}_4$  in the glass (52-74%). In 1985 a ZBLAN fiber with a core diameter of 18-30  $\mu\text{m}$  (from Le Verre Fluoré) was measured to have a peak Raman gain of  $a_1 = 1 - 3 \cdot 10^{-11}$  cm/W at a Stokes shift of  $\nu_1 = 17.7$  THz when pumping at 1.0  $\mu\text{m}$  [62]. The fibers used in this paper have an index contrast of  $\Delta n = 5 \cdot 10^{-3}$ , which roughly corresponds to  $\text{NA} \sim 0.15$ , and core diameters from 18 to 30  $\mu\text{m}$ , and are multimode at the considered wavelength (1064 nm). Also in 1985 a ZBLAN fiber with a core diameter of 65  $\mu\text{m}$  (60% $\text{ZrF}_4$ -30% $\text{BaF}_2$ -3% $\text{LaF}_3$ -4% $\text{AlF}_3$ -3% $\text{NaF}$ ) was measured at 514.5 nm to have a Raman peak at  $\nu_1 = 17.4$  THz with a maximum gain of  $6 \cdot 10^{-11}$  cm/W [63]. A smaller peak Raman gain of  $a_1 = (2 \pm 0.5) \cdot 10^{-11}$  cm/W at a Stokes shift of  $\nu_1 = 17.9$  THz was measured at 580 nm in a ZBLAN fiber with core diameter of 70  $\mu\text{m}$  (from Le Verre Fluoré) in 1993 [64]. Here a second broader local maximum gain was also observed at a Stokes shift of  $\nu_2 = 10.2$  THz [64]. These findings constituted the knowledge or the Raman response in ZBLAN when work began, and the reports generally agree that a prominent Raman gain located around 17 to 18 THz Stokes shift should be expected, along with one measurement that finds a gain located around 10 THz Stokes shift.

### 3.2.1 Measurement of Delayed Raman Response in the ZBLAN Fiber

The complete details regarding the measurement of the delayed Raman gain profile in the  $2a = 10.7 \mu\text{m}$ ,  $\text{NA} = 0.2$ , ZBLAN, SIF, also used for dispersion measurement, is presented in reference [59]. The experiment has been performed by our collaborators, primarily owing to work by C. Petersen and S. Dupont, from AU. The measurement is a pump-probe measurement, which in essence, compares the gain experienced by a broadband probe signal, when it is accompanied through the fiber under consideration by a pump beam, to the spectrum from when it is unaccompanied. The method proposed, uses a short piece of fiber,  $L = 35 \text{ cm}$ , which limits walk-off effects between pump and probe caused by dispersion, and renders attenuation a small concern. The measurement setup is displayed in Fig. 3.4 [59].

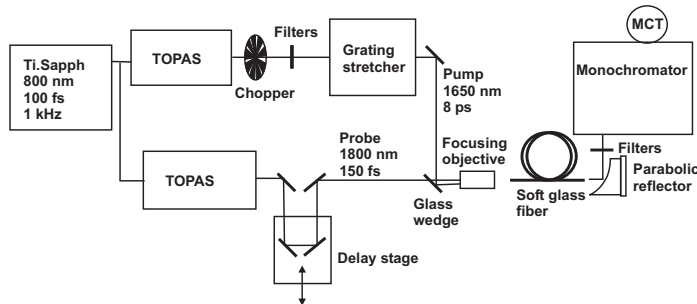


**Figure 3.4:** Schematic of experimental setup for the pump-probe measurement of the delayed Raman gain profile in the  $2a = 10.7 \mu\text{m}$ ,  $\text{NA} = 0.2$ , ZBLAN, SIF. Graphics is courtesy of C. Petersen [59].

The main laser system consists of a Ti:Sapphire regenerative amplifier, which gives 800 nm pulses with a full-width-at-half-maximum (FWHM) of 0.1 ps, a pulse energy of 1 mJ, and the laser has a repetition rate of  $f_{\text{rep}} = 1 \text{ kHz}$ . The output is divided into two beams directed into two tunable optical parametric amplifier systems (TOPAS, Light Conversion) that can be wavelength tuned separately, and thereby generate the pump and the probe at 1650 and 1800 nm respectively. A chopper in the pump laser arm is synchronized with the laser system and absorbs every second shot, so the spectra of the probe signal can be recorded either accompanied by or unaccompanied by the pump pulse at 1650 nm in consecutive shots. The pump pulse is stretched temporally by inducing a chirp from a grating, to

approximately 8 ps so nonlinear effects caused by the pump are avoided. The probe signal passes a delay stage, where the temporal overlap between pump and probe can be adjusted before the light beams are coupled into the ZBLAN SIF together, and the output spectra are recorded by a spectrometer.

The gain profile, that was recorded at AU, is shown as black dots in Fig. 3.5-left. This measurement confirm the gain peak at  $\nu_1 = 17.4$  THz

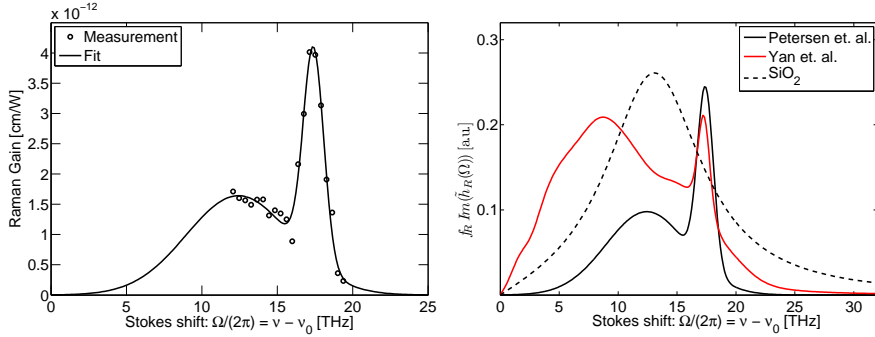


**Figure 3.5:** Left: Raman gain profile measured at AU with a pump wavelength of  $\lambda_p^R = 2\pi c/\omega_p^R = 1650$  nm. Dots are experimental data and solid line shows the fit given by Eq. (3.2.1) and Table 3.1 [59]. Right: Plot of  $f_R \text{Im}(\hat{h}_R(\Omega))$  for the two available full Raman profiles [59, 65], and for silica for comparison [6].

and also finds a second broader peak as in [64] but at  $\nu_2 = 12.4$  THz. In the co-propagating pump-probe experiment, it is not possible to measure the gain spectrum for small Stokes-shifts due to a strong background contribution from the pump. However, measurements of the spontaneous Raman scattering spectrum for ZBLAN display non-vanishing values of the scattering cross-section for low Stokes-shifts [63]. To accommodate this non-vanishing gain for small Stokes-shifts, the measured Raman gain is fitted to a sum of two Gaussian functions, so the gain profile takes the form [59]

$$g_R(\Omega) = a_1 e^{-\frac{(\Omega/(2\pi) - \nu_1)^2}{2w_1^2}} + a_2 e^{-\frac{(\Omega/(2\pi) - \nu_2)^2}{2w_2^2}} \quad (3.2.1)$$

where  $a_j$  is the amplitude,  $\nu_j$  is location and  $w_j$  is the width of the  $j$ 'th Gaussian fitted peak of the delayed Raman gain. The Gaussian fit is shown in solid black in Fig. 3.5-left and the coefficients for Eq. (3.2.1) are listed in Table 3.1. Recently bulk measurements of a ZBLAN glass with the same composition as the fiber investigated here, placed the

two peaks at 17.7 THz and 8.4 THz with identical amplitudes of  $1.15 \cdot 10^{-11}$  cm/W [65]. The parameters, adapted to the form of Eq. (3.2.1), for all the mentioned measurements, partial and full, of the Raman response of ZBLAN fibers (notice that reference [65] uses bulk ZBLAN) are summarized in Table 3.1 for comparison. Here the amplitudes values are

Ref.	$a_1$	$a_2$	$\nu_1$	$\nu_2$	$w_1$	$w_2$	$f_R$
	[ $10^{-11}$ cm/W]		[THz]		[THz]		
[59]	0.54	0.25	17.4	12.4	0.68	3.5	0.06
[62]	1 – 3	-	17.7	-	-	-	-
[63]	2.91	-	17.4	-	-	-	-
[64]	1.09	-	17.9	10.2	-	-	-
[65]	0.85	0.85	17.7	8.4	2.7	12.9	0.24
[66]	3.6	-	17.7	-	1.19	-	0.19

**Table 3.1:** Overview of literature values for the delayed Raman gain, adapted to the form of Eq. (3.2.1) and scaled to a measurement wavelength of 1060 nm for comparison [67].

scaled to a measurement wavelength of 1060 nm [67]. All measurements agree in that the main gain peak is around 17.4 THz, while, in contrast, there is a large spread in the location of the second and broader gain peak measured at AU to be located at 12.4 THz. The spread in the amplitude of the main gain peak value ( $a_1$ ) is a factor 7 and thus also quite significant. Here it is important to bare in mind that ZBLAN is a composite material with properties that depend on the specific composition. In addition, the process of fiber drawing may have a significant influence on the resulting material properties of ZBLAN as, e.g., shown in [68], where it was found that the drawing process reduces the refractive index on the order of  $10^{-3}$ . This could be one reason for the difference between the AU-measured fiber Raman gain and the bulk Raman gain measured in [65], where the same ZBLAN composition is used in both cases.

When a Raman gain profile  $g_R = g_R(\Omega)$  is given, the time response function  $h_R(T)$  is calculated as [6, 69] (see appendix G page 133 for a detailed derivation of this)

$$h_R(T) = \frac{\theta(T)}{f_R} \frac{c}{\pi n_2 \omega_p^R} \int_0^\infty g_R(\Omega) \sin(\Omega T) d\Omega \quad (3.2.2)$$

where  $\theta(T)$  is the Heaviside step-function that ensures causality,  $\omega_p^R$  is the frequency of the pump pulse (Petersen *et al.* used  $\lambda_p^R = 1650$  nm [59])

in the gain profile measurement experiment, and  $f_R$  is found as a normalization factor by requiring that  $\int h_R(T)dT = 1$ . This normalization is important, because simulations need not only the specific shape and fitting parameters of the gain profile, but also the integrated fractional Raman contribution,  $f_R$  derived from the normalization of Eq. (3.2.2). From the AU-measured gain profile and Eq. (3.2.2)  $f_R = 0.062$  is found. If we again compare with [65] then their value of  $f_R = 0.24$ , is four times larger than the value found at AU. In Fig. 3.5-right is shown a plot of

$$f_R \text{Im} \left( \tilde{h}_R(\Omega) \right) = \frac{g(\Omega)}{2\gamma} \quad (3.2.3)$$

for the measurement at AU and by Yin *et al.* [65], and also a representative gain spectrum for fused silica is plotted for comparison [6], and here it is clear, how the Raman response found by Yin *et al.* is stronger than found by AU, and particularly the low frequency broad gain peak is stronger than found in [59]. Furthermore, the value for the nonlinear refractive index is found to be  $n_2 = 5.4 \cdot 10^{-20} \text{ m}^2/\text{W}$  in [65], while in this work is used the generally accepted value of  $n_2 = 2.1 \cdot 10^{-20} \text{ m}^2/\text{W}$  [7, 45, 55, 66].

Finally, it must be noted that a general uncertainty in the value of  $f_R$  for ZBLAN is observed in the literature on numerical modeling. For example  $f_R$  is sometimes simply assumed to have a value close to silica,  $f_R = 0.2$  [7] or data from the ZBLAN Raman gain (with two main peaks) is inserted into a single oscillator model, e.g., giving  $f_R = 0.19$  [66].

Regardless of other measurements, the Raman gain profile measured at AU is implemented in simulations of SC through use of Eq. (2.4.7). In section 3.3.6, the debate of the Raman profile is briefly visited once more.

### 3.3 Supercontinuum Generation in the ZBLAN Fiber

Reasonable material parameters have been established, and the dispersion properties of the fiber available to measurements, have been calculated. The next step in the process is to measure the spectra of a generated SC in the  $10.7 \mu\text{m}$  fiber, also used in the two previous sections and compare it to simulations. Again, the measurements are made by our collaborators at AU, owing to C. Petersen and S. Dupont, while the role of the author has been to interpret the spectra in terms of the physical processes, based on simulations, and give suggestions as to what specifically to focus on, when designing a mid-IR SC laser.

Before investigating the experiment and results of simulations, a few other measurements of ZBLAN based SCG are examined. During this project, there has been a slight competition between ours and foreign research groups that also try to extend SC into the IR, and admittedly these groups had a head start. One of the early reports of ZBLAN based SCG, which is from 2006, is found in [48], where a concatenated silica-ZBLAN fiber system, pumped by an Er source, generates solitons that redshift from  $1.55\ \mu\text{m}$  and to approximately  $3\ \mu\text{m}$ . Both fibers used in [48] are SIFs, and the ZDW for the ZBLAN fiber is reported to be  $1.63\ \mu\text{m}$ , i.e., similar to the  $10.7\ \mu\text{m}$  fiber used in measurements at AU, and the fiber described in [62]. In [48] the Er source pump is at  $1.55\ \mu\text{m}$ , i.e., in the normal dispersion regime of the ZBLAN fiber, and the silica fiber acts like an intermediate passive step, between pump and soft-glass fiber, where the pump pulse is redshifted to cross the ZDW of the ZBLAN fiber before coupling it in.

Also in 2006 was presented an example for imitation [55]. The experimental setup, used in this letter, is the same as used in a paper from the same group the following year [70] and again in 2009 [47], and resembles the system from reference [48]. The pump system from [47, 55, 70] also build on passive concatenation of a silica and a ZBLAN fiber, so light crosses the ZDW of the ZBLAN fiber before in coupling. The widest SC achieved extends to approximately  $4.5\ \mu\text{m}$ , and an increasingly higher average power, culminating at 10.5 W is developed over the course of their achievements from 2006 to 2009. This large average power, however, is mostly caused by an increased repetition rate of the seed laser, and less because the individual shots from the seed laser are developed to become increasingly energetic. Quite recently though, the group published results, where an active element is implemented in their pump setup just prior to coupling light into a ZBLAN SIF [71]. The active element is a Tm doped fiber amplifier that boosts the power of wavelength components around  $2\ \mu\text{m}$  before continuing SCG in the ZBLAN fiber. The Tm amplifier causes more light to shift to wavelengths beyond  $3.8\ \mu\text{m}$  than when using the passive source, but also, it absorbs all light below  $1.8\ \mu\text{m}$  thus effectively a SCG between  $1.9\ \mu\text{m}$  and  $4.5\ \mu\text{m}$  is obtained. The Tm amplifier does not enable an extension of the  $4.5\ \mu\text{m}$  edge, which is caused by inherent material loss according to [71].

An optimistic paper from 2009 [45], finds that the upper limit for SCG in ZBLAN is determined solely by the fiber confinement loss, and if this can be controlled or neglected the long wavelength edge can be ex-

panded above  $4.5 \mu\text{m}$ . In fact it is found that by using a very short piece of ZBLAN SIF (0.9 cm and 2 cm respectively) from FiberLabs ( $2a = 9 \mu\text{m}$ ,  $\text{NA} = 0.2$  and  $\lambda_{\text{ZD}} = 1.65 \mu\text{m}$ ), losses are negligible, and the long wavelength edge can be extended as far as  $6.28 \mu\text{m}$  using normal dispersion regime pumping at  $1450 \text{ nm}$ , and it is speculated that SC as far as  $8 \mu\text{m}$  is achievable. This group is the same as made the Raman gain profile measurement from reference [65] discussed in the previous section.

This extract of measurements, composed the state-of-the-art reports of SC in ZBLAN-based fibers at the onset of this project, i.e., spectra to approximately  $4.5 \mu\text{m}$  had been produced and reproduced. Generally, references spice their measurements with numerical simulations only occasionally, and when they do, limited information about the calculations is provided and correspondence between measurement and simulation is not always perfect. Numerical simulations have helped tremendously in the development of silica based SC sources, and similarly numerical predictions might prove helpful to optimize mid-IR SC sources. With the aim of achieving SC to  $4.5 \mu\text{m}$ , the measurements and simulations that are presented in the following were performed.

### 3.3.1 Experimental Setup for Measurements of Supercontinuum

The experimental setup for SC measurements at AU is similar to the one used for the Raman measurement. It is slightly simpler though, because in principle, experimental SCG is basically a matter of forcing as much light as possible into the nonlinear fiber at once, without burning it. Thus, the system for the measurement of SCG, which is shown in Fig. 3.6 [33], is a

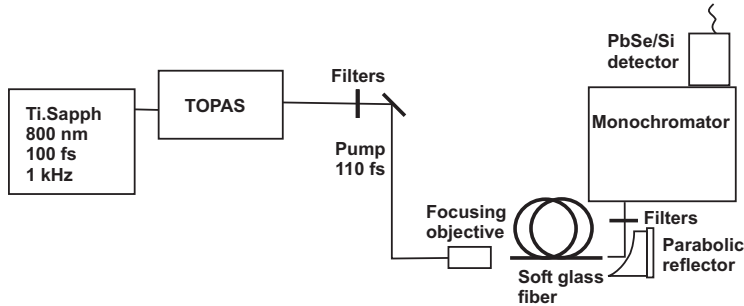


**Figure 3.6:** Experimental setup for our SC measurement. Graphics is courtesy of C. Petersen [59].

pump laser, some focusing optics, the nonlinear fiber under investigation, and a spectrometer to acquire the generated SC. The pump laser, which is the same as described in section 3.2, is directed into a single TOPAS that allows the pump wavelength to be tuned in the range from 1200 nm to 2600 nm, thus enabling pumping in both the normal and anomalous dispersion regime of the nonlinear fiber. Usually, the output from the TOPAS is strongly attenuated, yielding pulse energies on the order of 1  $\mu$ J. The pulse duration of the pump is determined by an intensity dependent autocorrelation, and the pump is coupled into the ZBLAN fiber with an efficiency around 30% using a  $\times 10$  focusing objective. The output from the fiber is collimated using a gold off-axis parabolic reflector with a focal length of 25 mm. The use of reflective optics ensures that the output from the fiber is not influenced by chromatic aberrations. The collimated output is sent to a scanning monochromator (Spectrapro2300i, Acton Research). The light is focused at the entry slit of the monochromator by a CaF<sub>2</sub> lens with focal length of 15 cm. The dispersed light at the exit slit is detected using a two-color detector (Si/PbSe, Hamamatsu) connected to a boxcar integrator synchronized with the laser system. Appropriate filters are inserted to suppress higher order diffraction artifacts. The spectrum is finally compiled from measurements with the various filters and gratings, as well as measurements with both Si and PbSe detectors to cover the entire wavelength range from the visible to the mid-IR. A correction is performed to account for the wavelength dependent efficiency of detectors and gratings. The output spectral density is normalized to the measured total output power [33].

### 3.3.2 Simulation of Supercontinuum Generation in the ZBLAN Fiber

Measured spectra of SC are presented below and compared to results from simulations. The measurements and simulations divide themselves into two categories. One part where pumping is performed in the normal dispersion regime at  $\lambda_p = 1450$  nm, and one where pumping is in the anomalous dispersion regime at  $\lambda_p = 2000$  nm. The pulse widths and peak powers for the pumping regimes are summarized as



- $\lambda_p = 1450$  nm: - The pulse width is  $T_{\text{FWHM}} = 145$  fs and two power levels are used.  
 - The lower peak power is  $P_0 = 710$  kW.  
 - The higher peak power is  $P_0 = 1180$  kW.
- $\lambda_p = 2000$  nm: - The pulse width is  $T_{\text{FWHM}} = 110$  fs and two power levels are used.  
 - The lower peak power is  $P_0 = 1110$  kW.  
 - The higher peak power is  $P_0 = 2130$  kW.

The fiber is  $L = 1.85$  m of the  $10.7$   $\mu\text{m}$ ,  $\text{NA} = 0.2$ , FiberLabs, ZBLAN, SIF already encountered above, with calculated ZDW of  $1.62$   $\mu\text{m}$ .

The initial condition for simulations, representing the pump pulses, is an unchirped Gaussian shaped function, given by Eq. (2.3.10). In all simulations the number of points on the frequency/time axis is  $N_t = 2^{17}$  and the GNLSE is solved in a wavelength window with  $\lambda_{\text{min}} = 0.45$   $\mu\text{m}$  and  $\lambda_{\text{max}} = 6$   $\mu\text{m}$ , which has a corresponding expansion wavelength of  $\lambda_0 = 2\pi c/\omega_0 = 837.2$  nm (see appendix D page 119). The time resolution is  $dt = 1.62$  fs, and the frequency resolution is  $d\omega = 2.25 \cdot 10^{15}$  rad/s, and the local goal-error is  $\delta_g = 10^{-6}$  [23, 35]. The nonlinear refractive index of ZBLAN is taken to be  $n_2 = 2.2 \cdot 10^{-20}$   $\text{m}^2/\text{W}$  in all simulations.

Using these numerical parameters that are fixed throughout the remainder of this section, ensures comparable results. Calculation time is on the order of a few days for a single shot, and thus to limit the computational effort, 30 independent runs for each ensemble average is used for the averaging procedure as discussed in chapter 2 section 2.3.1. To check the numerical implementation of the GNLSE, the photon number error [36] (see Eq. (2.3.11) page 18) is plotted in Fig. 3.7, for a typical simulation with  $P_0 = 1110$  kW,  $T_{\text{FWHM}} = 110$  fs and  $\lambda_p = 2000$  nm, corresponding to the simulation shown in Fig. 3.16, though neglecting loss and noise. Here it is seen that the relative error stays below  $5 \cdot 10^{-6}$ .

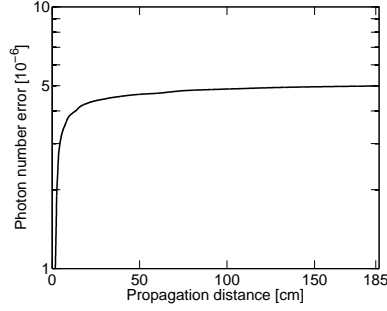


**Figure 3.7:** The photon number error as function of propagation distance for a typical simulation neglecting loss and noise.  $P_0 = 1110$  kW,  $T_{\text{FWHM}} = 110$  fs and  $\lambda_p = 2000$  nm.

### 3.3.3 Normal Dispersion Regime Pumping

A single shot contour plot of the spectral development for the two power levels used when pumping in the normal dispersion regime is shown in Fig. 3.8-left and right. The pulse quickly undergoes a large broadening and already after  $\sim 10$  cm of propagation, individual solitons that start redshifting due to the SSFS are clearly visible on the long wavelength side of the pump. To review the spectral development from the onset of propagation, single shot example power distributions and corresponding ESDs are shown, for the first  $\sim 7.5$  cm, in Figs. 3.9 and 3.10 for the low and high

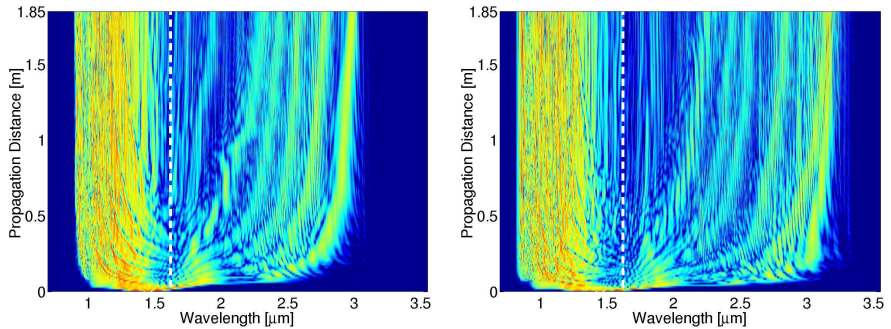


**Figure 3.8:** Single shot spectral development calculated for  $P_0 = 710$  kW (left) and  $P_0 = 1180$  kW (right) and  $\lambda_p = 1450$  nm. White dashed line marks the fiber ZDW. Both plots are normalized logarithmic plots truncated at  $-40$  dB.

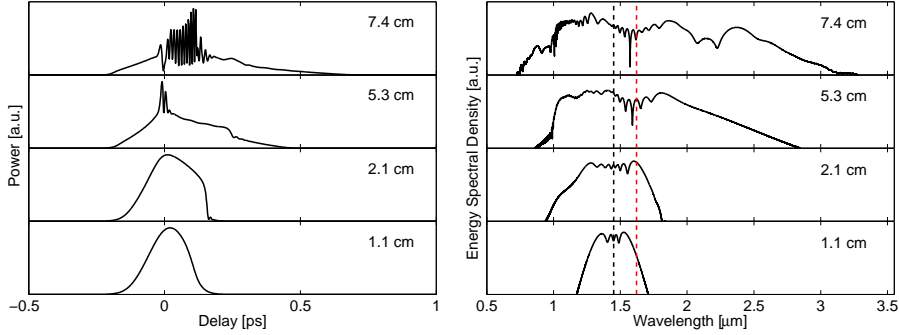


**Figure 3.9:** Left: Temporal profile in the first  $\sim 7.5$  cm of propagation. Right: Corresponding development of the ESD during propagation. Black (red) vertical line marks the pump (ZDW of the fiber).  $\lambda_p = 1450$  nm and  $P_0 = 710$  kW.

peak power level respectively. In both figures, it is observed how the pulse spectrum initially broadens due to SPM, and that light crosses the ZDW into the anomalous dispersion regime. This initial SPM is clearly noticed until  $\sim 2$  cm of propagation in both Figs. 3.9-right and 3.10-right. The ripples are characteristic of SPM and build up around the center of the pulse, though they are not symmetric, which is expected from pure SPM, but the asymmetry is caused by the optical shock effect [6]. The optical shock effect also causes the slanted power distributions observed in the corresponding temporal profiles. When SPM has broadened the pulse enough spectrally, GVD will cause it to break up temporally, and

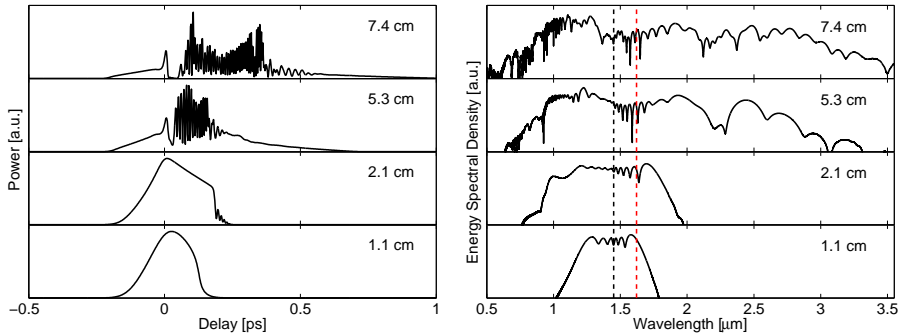


**Figure 3.10:** Left: Temporal profile in the first  $\sim 7.5$  cm of propagation. Right: Corresponding development of the ESD during propagation. Black (red) vertical line marks the pump (ZDW of the fiber).  $\lambda_p = 1450$  nm and  $P_0 = 1180$  kW.

this has just happened at 5.3 cm in Fig. 3.9-left, while in Fig. 3.10-left the break up is more pronounced at 5.3 cm. The light that has crossed the ZDW into the anomalous dispersion regime, forms solitons that radiate dispersive waves, phase-matched with the solitons across the ZDW. The solitons subsequently undergo redshift due to SSFS, all the while the dispersive waves blue shift slightly on the normal dispersion side of the ZDW [14, 37, 72, 73]. The soliton number (see chapter 2) is given by

$$N = \sqrt{\frac{n_2 \omega_{\text{sol}}}{c A_{\text{eff}}(\omega_{\text{sol}})} \frac{P_0 T_0^2}{|\beta_2(\omega_{\text{sol}})|}} \quad (3.3.1)$$

where  $\omega_{\text{sol}}$  is the frequency of the soliton, and as light passes the ZDW into the anomalous dispersion,  $N$  becomes large because  $\beta_2 \rightarrow 0$  at the ZDW. This means that a significant amount of solitons can be generated even though only a fraction of the pump energy passes the ZDW by SPM. After the initial approximately 10 cm of propagation the dynamics becomes less dramatic, and it is perhaps best displayed in Fig. 3.8-left and -right how the continued propagation is dominated by redshifting solitons and corresponding dispersive radiation in the normal dispersion regime.

Fig. 3.11 shows a single shot spectrogram (Fig. 3.11-left) and the corresponding ESD (Fig. 3.11-right) after  $L = 1.85$  m. At the output of the fiber, at least  $N = 6$  solitons, phase-matched with non-solitonic radiation (marked by vertical dotted lines in Fig. 3.11-left), are clearly

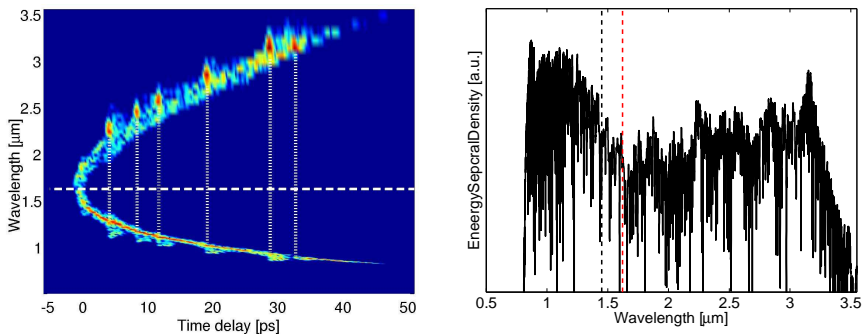


**Figure 3.11:** Left: Spectrogram after  $L = 1.85$  m. The vertical white lines mark distinguishable solitons phase-matched to non solitonic or dispersive wave radiation. Right: The corresponding single shot pulse ESD. White (red) dashed horizontal (vertical) line marks the calculated ZDW in the left (right) panel. In both plots, the pump wavelength is  $\lambda_p = 1450$  nm and  $P_0 = 1180$  kW.

distinguishable, and it is also clearly seen, how the redshifting solitons determine the long wavelength edge of the SC, while the phase-matched dispersive waves determine the short wavelength edge. Normal dispersion regime pumping can thus generate a broad SC, as was also found in [45] in ZBLAN and already in 1978 in silica [41].

### Dispersion Measurement - Intermezzo

As a small side note at this point, it can be mentioned that the curve shape observed in Fig. 3.11-left, is a representation of the group-velocity wavelength dependence experienced by light propagating in the fiber. In Fig. 3.11-left, a time delay of zero, corresponds to the arrival of the pump frequency component at the fiber end facet. A negative delay corresponds to frequency components arriving sooner than the pump, and frequencies with positive delays arrive later than the pump. The frequency component to arrive first is, by definition, the ZDW, since this designation is reserved for points of extreme on the group-velocity curve (see Eq. (2.2.7)). For the fundamental mode, this extreme means that the ZDW marks the fastest travelling frequency component in the fiber. Because the curve observed in Fig. 3.11-left is a simulated result, it is a representation of the numerically implemented group-velocity curve, obtained from the `Comsol` calculation. But a spectrogram as shown in Fig. 3.11-left can be obtained from measurements on existing fibers, by using frequency resolved optical gating (FROG) experiments [14]. The GVD in a fiber, can then be found by a FROG measurement and subsequent differentiation of the obtained group-velocity curve. The method could be a viable alternative to dispersion measurements by the interferometric procedure used in section 3.1.1 [60], which is strongly influenced by beatings between higher order modes in the fiber. Dispersion measurements on nonlinear fibers by FROG measurements have been proposed in 1997 in [74], though demonstrated in a relatively limited wavelength range. Quite recently, such measurements have been done at AU, with another aim than measuring dispersion, but seemingly, the method will be able to determine the dispersion of multiple modes excited in the fiber in one sitting and over a wide wavelength range.

### 3.3.4 Supercontinuum Generation - Continuing

The end results of simulations and measurements of normal dispersion regime pumping SCG are compared in Fig. 3.12-left and -right for a peak power of  $P_0 = 710$  kW and in Fig. 3.13-left and -right for  $P_0 = 1180$  kW. Measurements are displayed as black curves, while other curves are calculated ensemble averages. In Fig. 3.12-left the green curve is calculated using the propagation constant calculated using Comsol (shown as solid black in Fig. 3.3-left), while the red curve is calculated with the wavelength shifted dispersion profile (dashed black in Fig. 3.3-left), as discussed in section 3.1.1. The dashed vertical lines in Figs. 3.12 and 3.13 mark the pump wavelength (black), the calculated ZDW (green), and the wavelength shifted ZDW (red) respectively. In Figs. 3.12-right and 3.13-right the blue curve is calculated using the numerically enhanced loss including the artificial absorption band, marked in Fig. 3.2.

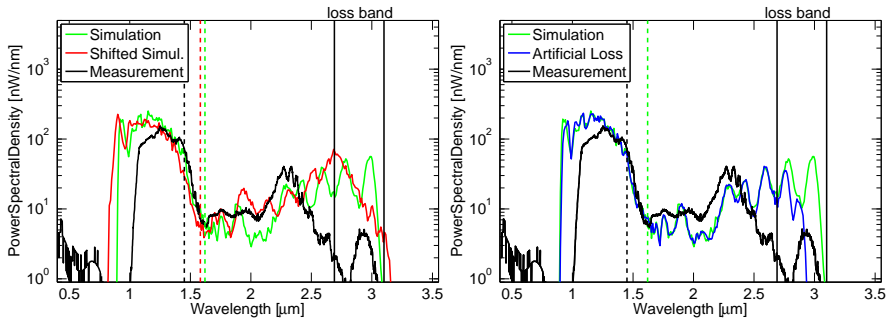


**Figure 3.12:** Left: Measurement (black) and simulations (green) of SCG for  $\lambda_p = 1450$  nm and  $P_0 = 710$  kW. The red spectrum is obtained for the wavelength shifted dispersion profile in Fig. 3.3-left. Right: Blue curve shows simulation using the artificially enhanced loss profile shown in blue in Fig. 3.2. Dashed vertical lines mark pump wavelength (black) and the ZDW (red, green) of the fiber.

Comparing the measurement and simulations in Fig. 3.12-left and right, the simulations generally show larger levels of the PSD at short wavelengths than the measurement observes. This fact gives an indication that the calculated dispersion is not exactly corresponding to the physical dispersion in the fiber, because the predicted group-velocity matching, displayed by the curve shape in Fig. 3.11-left, is different from the physical one. Another prominent feature from the comparisons, is that measurements show a significantly lower amount of light in the wavelength region

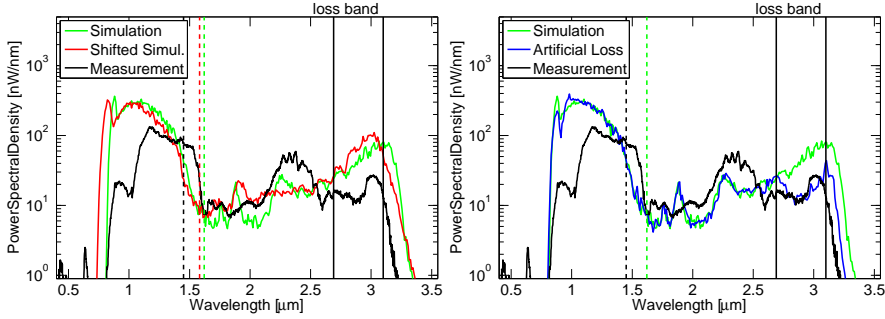


**Figure 3.13:** Left: Measurement (black) and simulations (green) of SCG for  $\lambda_p = 1450$  nm and  $P_0 = 1180$  kW. The red spectrum is obtained for the wavelength shifted dispersion profile shown in Fig. 3.3-left. Right: The blue curve shows the simulation with artificial loss shown in Fig. 3.2. Dashed vertical lines mark pump wavelength (black) and the ZDW (red, green) of the fiber.

above  $2.7 \mu\text{m}$  than what is found in simulations. As already mentioned in section 3.1, a possible explanation for this is an attenuation band caused by water absorbed in the fiber, and this band is qualitatively marked with vertical black solid lines in the figures presenting spectra. The SC spectra, plotted in blue in the right panel of Fig. 3.12 and 3.13, show simulated results that include the artificial loss. The loss band provides a barrier that halts the SSFS, and consequently simulations with no artificial loss predict a longer wavelength edge, and a larger level of the PSD in the absorption band, than the artificial loss simulation does.

By the group-velocity matching mechanism between redshifting solitons and the dispersive waves already mentioned, the overshoot of the predicted long wavelength edge of the generated SC, observed in the green and red curves of the left panels of Figs. 3.12 and 3.13, cause a similar overshoot of the short wavelength edge. Therefore the spectrum is predicted to be too wide in either end. This overestimation of the bandwidth is reduced slightly in the simulations with artificial loss, shown in blue in the right panels of Figs. 3.12 and 3.13, because the loss barrier halts the SSFS and consequently will predict a blue wavelength edge closer to the pump. Simulation including the artificial loss show a behaviour more similar to that of the measured SC spectrum. This is particularly clear in Fig. 3.13-right, while in Fig. 3.12-right it is seen that the loss is not completely explaining discrepancies between measurements and simulations.

From the calculated spectra in Figs. 3.12 and 3.13 the width of the SC spectral output can be measured, where the limit used is  $\text{PSD}(\lambda) > 1 \text{ nW/nm}$ . The bandwidths become  $\Delta\lambda^m = 2.05 \text{ }\mu\text{m}$ ,  $\Delta\lambda^c = 2.19 \text{ }\mu\text{m}$ , and  $\Delta\lambda_{\text{WS}}^c = 2.33 \text{ }\mu\text{m}$  for the measured ( $m$ ), calculated ( $c$ ) and wavelength shifted (WS) PSD, respectively, for pumping with  $P_0 = 710 \text{ kW}$ . Increasing the power to  $P_0 = 1180 \text{ kW}$  one finds  $\Delta\lambda^m = 2.40 \text{ }\mu\text{m}$ ,  $\Delta\lambda^c = 2.52 \text{ }\mu\text{m}$ , and  $\Delta\lambda_{\text{WS}}^c = 2.61 \text{ }\mu\text{m}$  respectively. The deviation between measured and calculated SC spectral widths are less than 15% in the worst case.

Finally, it is seen that the effect of wavelength shifting the dispersion profile to shorter wavelengths is to shift the edges of the PSD similarly while not affecting the width of SCG greatly, and thus, the exact location of the fiber ZDW is not crucial to prediction of this wide SC spectra. It is also observed that the SC from the wavelength shifted dispersion operator is the broadest when pumping in the normal dispersion regime. This is because the ZDW is moved closer to the pump, and consequently light is pushed into the anomalous dispersion regime at an earlier stage of propagation and soliton dynamics start sooner.

### 3.3.5 Anomalous Dispersion Regime Pumping

In the anomalous pumping regime, when pumping at  $\lambda_p = 2000 \text{ nm}$ , the spectral development of the SC is governed by soliton dynamics from the beginning of propagation. Contour plots showing the spectral development for the two power levels of  $P_0 = 1110 \text{ kW}$  and  $P_0 = 2130 \text{ kW}$

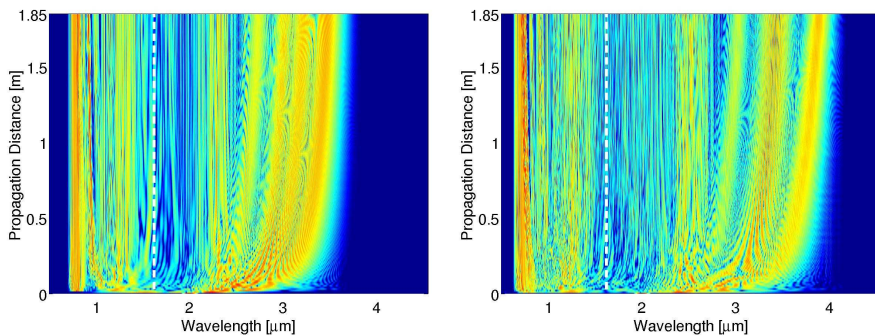


**Figure 3.14:** Spectral development calculated for  $P_0 = 1110 \text{ kW}$  (left) and  $P_0 = 2130 \text{ kW}$  (right) and  $\lambda_p = 2000 \text{ nm}$ . White dashed line marks the fiber ZDW. Both plots are normalized logarithmic plots truncated at  $-40 \text{ dB}$ .



are shown in Fig. 3.14-left and -right respectively. Also in this regime is observed a rapid broadening of the input pulse. To elaborate on the dynamics of the SCG, Fig. 3.15-left and -right illustrate the spectral development in the first  $\sim 5$  cm of propagation. In the anomalous dispersion regime, the pump laser excites a higher order soliton from the onset of propagation, and the soliton number is  $N \approx 14.1$  and  $N \approx 19.6$  for the low and high power case respectively. The soliton undergoes initial pulse compression of the power distribution while SPM broadens it in the frequency domain, and this is observed in the bottom of Fig. 3.15-right. The periodic recovery of the initial pulse shape exhibited by an ideal higher order soliton (see chapter 2) is lost because the propagation is perturbed by higher order dispersion and Raman scattering etc. Instead of returning to the initial pulse shape, the pulse fissions into a number of constituent fundamental solitons that are clearly visible in Fig. 3.15-left already after  $\sim 2$  cm of propagation [14,37]. The rapidly redshifting solitons are ejected from the main pulse due to the slow down in propagation speed caused by the GVD. As earlier discussed, the redshifting solitons emit phase-matched dispersive waves, during the fission process, at wavelengths shorter than the ZDW. This is similar to what was found for normal dispersion regime pumping. After the initial and dramatic soliton fission the propagation continues with prominent redshift much like in the normals dispersion pumping case, and this is observed in the contour plots of Fig. 3.14.

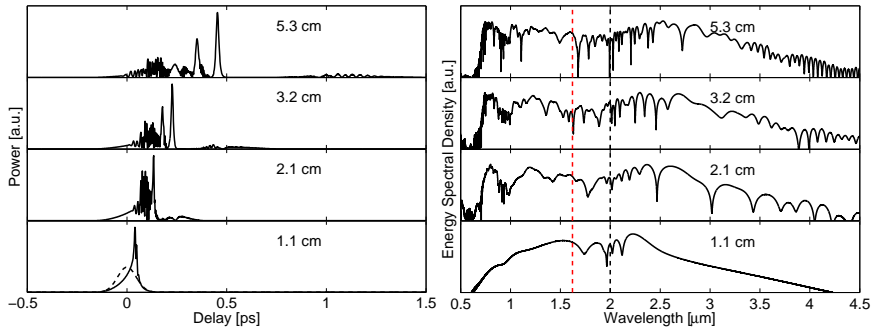


**Figure 3.15:** Left: Temporal profile in the first  $\sim 5$  cm of propagation. Dashed curved in bottom power distribution is the input pulse. Right: Corresponding development of the ESD during propagation. Black (red) vertical line marks the pump (ZDW of the fiber). The soliton number is  $N \approx 14.1$ , and  $\lambda_p = 2000$  nm and  $P_0 = 1110$  kW. Dashed black (red) vertical line marks pump wavelength (ZDW).

The comparisons between measurement and simulations for the two power levels used in the anomalous dispersion regime are shown in Fig. 3.16-left and -right for a peak power of  $P_0 = 1110$  kW and in Fig. 3.17-left and -right for  $P_0 = 2130$  kW respectively.

As in the last section the red, green and blue curves are ensemble averages, where the red curve is calculated using the wavelength shifted dispersion profile (dashed black in Fig. 3.3-left) and blue is calculated using the artificial loss, shown in Fig. 3.2. The same trend as in Figs. 3.12 and 3.13 is observed in Figs. 3.16 and 3.17, where the level of measured PSD is lower in the band from  $2.7$  to  $3.5 \mu\text{m}$  than the simulated level. However, the SSFS is so strong, when pumping directly in the anomalous dispersion regime, especially when pumping with  $P_0 = 2130$  kW that solitons can cross the loss band and shift to wavelengths longer than  $3.5 \mu\text{m}$ . The long wavelength edge is then ultimately determined by the fiber transmission window that stops around  $4.5 \mu\text{m}$ . In Fig. 3.16-right, the simulation including the artificial loss is shown in blue. The simulation confirms the trend that an attenuation band may be present in the experiment from around  $2.7 \mu\text{m}$ , which is not accounted for by simulations without the artificially enhanced loss. However, the attenuation introduced artificially do not exactly predict the location of the long wavelength edge of the SC.

From Figs. 3.16 and 3.17 the bandwidth of the measured and the calculated SC spectra can be found. The bandwidths become  $\Delta\lambda^m =$

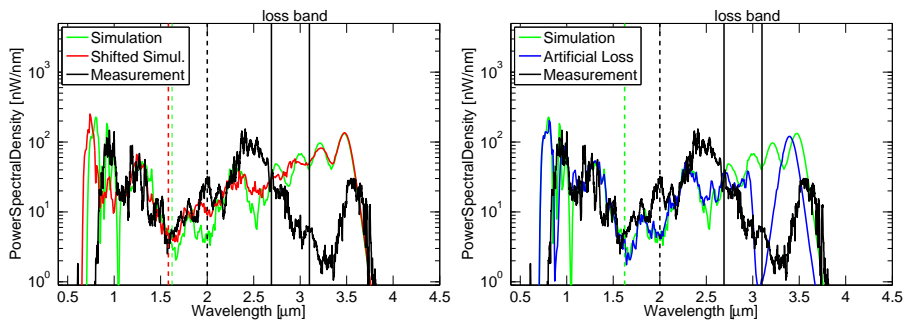


**Figure 3.16:** Left: Measurement (black) and simulations (green and red) of SCG for  $\lambda_p = 2000$  nm and  $P_0 = 1110$  kW. The red spectrum is obtained for the wavelength shifted dispersion profile shown in Fig. 3.3-left. Right: The blue curve shows the simulation with artificial loss shown in Fig. 3.2. Dashed vertical lines mark pump wavelength (black) and the ZDW (red, green) of the fiber.

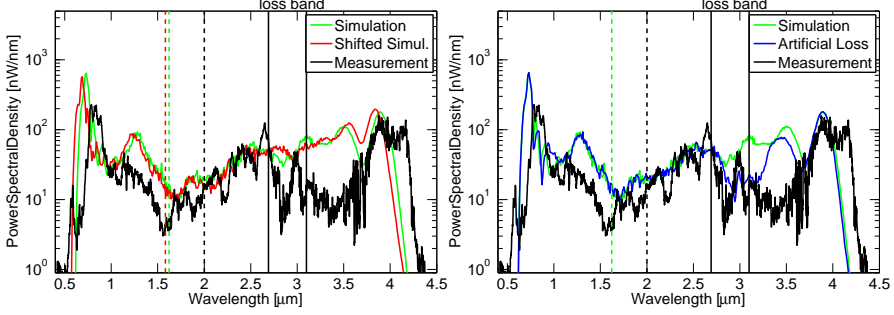


**Figure 3.17:** Left: Measurement (black) and simulations (green and red) of SCG for  $\lambda_p = 2000$  nm and  $P_0 = 2130$  kW. The red spectrum is obtained for the wavelength shifted dispersion profile shown in Fig. 3.3-left. Right: The blue curve shows the simulation with artificial loss shown in Fig. 3.2. Dashed vertical lines mark pump wavelength (black) and the ZDW (red, green) of the fiber.

$3.0 \mu\text{m}$ ,  $\Delta\lambda^c = 3.0 \mu\text{m}$  and  $\Delta\lambda_{\text{WS}}^c = 3.1 \mu\text{m}$  for low power  $P_0 = 1110$  kW and  $\Delta\lambda^m = 3.7 \mu\text{m}$ ,  $\Delta\lambda^c = 3.6 \mu\text{m}$  and  $\Delta\lambda_{\text{WS}}^c = 3.6 \mu\text{m}$  for high power  $P_0 = 2130$  kW. The deviation between the measured and calculated SC spectral widths is in this regime less than 5%. In the anomalous pumping regime, is also see a small shifting of the entire spectrum to shorter wavelengths, when applying the wavelength shifted dispersion profile.

### 3.3.6 Discussion of Spectral Predictions

There are several factors that can cause the observed discrepancies between the measured and calculated width of the generated SC. The discrepancies can first and foremost be related to uncertainty in the fiber attenuation and dispersion, as well as to the assessment of the peak power coupled into the fiber. Regarding the dispersion uncertainty, it has been verified that a shift of the dispersion profile on the order of tens to a hundred nm do not have great impact on the width of predicted SC. An uncertainty in the group-velocity matching, however, have a larger impact on the predicted widths, since the blue edge is determined by the dispersive waves linked to the redshifting soliton through the group-velocity matching. A measurement of the dispersion, e.g., by the FROG measurement technique discussed in section 3.3.3 might give good insight into the entire GVD profile of the fiber. It should also be mentioned that the diameter of the ZBLAN SIFs available to our measurements have been

found to vary quite significantly over relatively short distances. Cutting a piece of fiber in two different places on a fiber spool, from the same production batch, have been known to result effectively in two different fibers. This is ascribed to the immaturity of the ZBLAN fiber technology, and will inevitably cause discrepancies between measurements and idealized simulations.

The assessment of the power coupled into the fiber is based on an autocorrelation of the input pulse along with measurements of the average power in the beam before and after propagation through the fiber. This is an indirect way of estimating the input power, which can cause disagreement between measured and calculated SC spectral widths. In [33] are made simulations that check the influence of the input peak power by redoing the calculations presented in the last section, with a peak power reduced by 20%. Generally it can be concluded from this investigation that the estimated peak power has not been too low, and that this may also be a cause of overshoot for the predicted bandwidths by simulations. However, as the spectral width of the simulated SC is predicted to within 15% for normal dispersion regime pumping and within 5% for anomalous dispersion regime pumping, the estimation of the power coupled into the fiber has been reasonable.

To conclude the findings from simulations of SCG in ZBLAN, a final investigation is made to review the significances of differences between measurements of the delayed Raman response at AU [59] and by Yin *et al.* [65].

### Delayed Raman Response - Revisited

A tentative comparison between calculated SCG using the Raman measurement by AU [59] and measured by Yin *et al.* [65] is showed in Fig. 3.18-left and -right. In this section, the blue curves are calculated using the delayed Raman response measured by Yin *et al.* [65] and their value of  $f_R = 0.24$ . The nonlinear refractive index however, is kept at  $n_2 = 2.2 \cdot 10^{-20} \text{ m}^2/\text{W}$ . The simulations are ensemble averages using 30 shots as the green curves, however, to keep the computational load low, the blue curves are calculated using fewer grid points ( $N_t = 2^{15}$ ), and a smaller calculation domain (stretching from 0.6 and 5  $\mu\text{m}$ ), than used in the last section, while the value of the goal error was  $\delta_g = 10^{-6}$ . This means that cyclic effects in the time domain are observed, however no spurious temporal overlap occur. In both graphs of Fig. 3.18 the blue curve predicts a significantly extended long wavelength edge, particularly

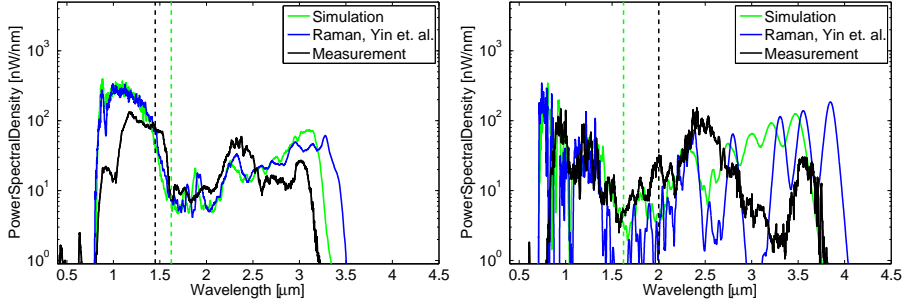


**Figure 3.18:** Comparison of measurement (black) and SCG calculated using Raman measured at AU [59] (green) or measured by Yin *et al.* [65] (blue). Left: Using  $\lambda_p = 1450$  nm and  $P_0 = 1180$  kW. Right: Using  $\lambda_p = 2000$  nm and  $P_0 = 1110$  kW.

in Fig. 3.18-right, and this wavelength edge will be extended even further, if the proposed value of  $n_2 = 5.4 \cdot 10^{-20}$  m<sup>2</sup>/W [65] is used.

Given these results, it seems adjacent to conclude that the magnitude of the measured Raman response by Yin *et al.* might be slightly overestimated. In the pump-probe technique employed by Petersen *et al.* at AU, it is troublesome to filter away the large background contribution from the pump and consequently it is hard to measure the delayed Raman gain for small Stokes-shifts. Thus it cannot be ascertained, with complete certainty, whether or not the spectrum by Yin *et al.* has the right shape, but it seems the measured magnitude, leading to  $f_R = 0.24$ , is somewhat too large.

### 3.4 Nonlinear Fiber and Seed Laser for Mid-infrared Supercontinuum Source

As clearly seen in the last section, the widest spectrum is achieved by pumping in the anomalous dispersion regime of the nonlinear ZBLAN fiber, and consequently a prototype mid-IR SC laser system should aim for this. Pumping in the normal dispersion regime, and having SPM cause light to cross the fiber ZDW, does create a SC, but it is not as broad, and the PSD level at long wavelengths is less, than if anomalous dispersion regime pumping causes soliton dynamics from the very beginning of propagation.

The ZDW of investigated ZBLAN SIFs has not been observed to be lower than  $1.55 \mu\text{m}$ , and Yb based lasers seem to be ruled out for being too deep in the normal dispersion regime. Tapering the ZBLAN fibers is a possibility for lowering the ZDW so it approaches the operating wavelength of Yb sources, and an extensive theoretical study of the dispersion properties of tapered ZBLAN SIFs, has been performed by M.Sc. student Irnis Kubat [75]. Tapering though, still rules out Yb based sources for pumping a ZBLAN fiber directly, but Er sources can prove useful [75]. Tapering will complicate the construction of a commercial system, and a first approach should be to aim for a seed laser above  $1.7 \mu\text{m}$  and no fiber taper. Such a system could be achieved by, e.g., using a Tm based source, or a concatenated fiber system, as studied in [47,48] and discussed in chapter 4, where a silica fiber acts like an intermediate redshifting agent between pump and ZBLAN fiber.

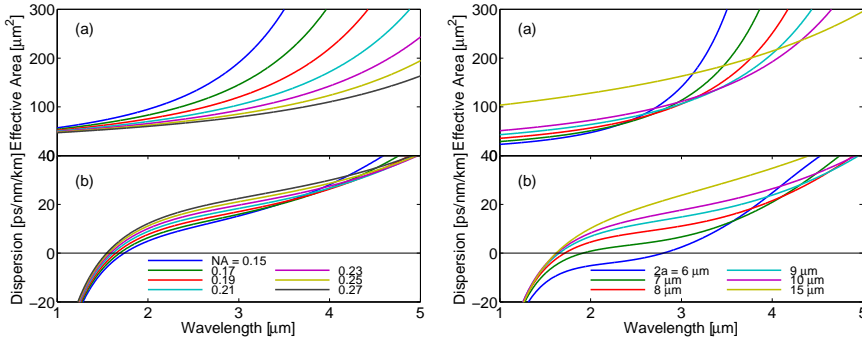


**Figure 3.19:** Left: Effective area (a) and dispersion (b) as function of wavelength for different NAs and core diameter  $2a = 10 \mu\text{m}$ . Right: Effective area (a) and dispersion (b) as function of wavelength for different core diameters and  $\text{NA} = 0.2$ .

Taking a closer look at Fig. 3.19, which displays effective area (a) and dispersion (b) of various ZBLAN SIFs, it is seen from Fig. 3.19-left(a) that a large NA is needed in order for the fundamental mode to stay well confined and guided by the core at long wavelengths. If the effective area becomes large, the nonlinear effects halt, because the field strength decreases (the nonlinear coefficient from Eq. (2.3.7) is inversely proportional to the effective area). Similarly, the right panel shows that using a smaller core fiber has a drastic impact on dispersion. Using a small core fiber will increase the effective nonlinearity, but too small a core will cause the guiding loss to increase (Fig. 3.19-right(a)). Thus, too

small a core can also be problematic for SCG to  $4.5 \mu\text{m}$ , and furthermore, it is often easier to achieve effective coupling between the pump fiber and the nonlinear fiber, if the core is reasonably large. Thus, the suggestion for a pump source and a nonlinear fiber, based on the measurements and simulations here, is a source in the anomalous dispersion regime ( $\lambda_p > 1.7 \mu\text{m}$ ) and a relatively large NA ( $\text{NA} > 0.20$ ) and with a small core  $2a < 10 \mu\text{m}$  ZBLAN SIF.

### 3.5 The Infrared Absorption Microscope

An application for mid-IR SC is developed at AU [13] and demonstrated in Fig. 3.20-(a) through (c). In Fig. 3.20-(a) an oil/water sample is placed

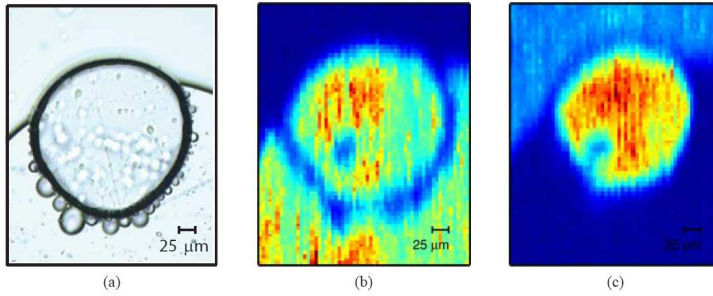
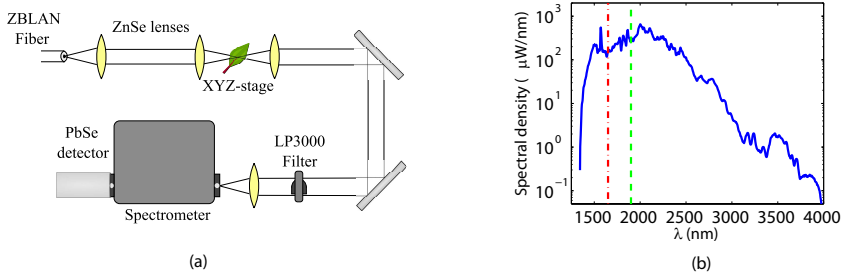


**Figure 3.20:** (a) Conventional microscope image of sample investigated by the IR absorption microscope. (b)  $3.05 \mu\text{m}$  (c)  $3.50 \mu\text{m}$ . Image size is  $300 \mu\text{m} \times 375 \mu\text{m}$  and each pixel is  $5 \mu\text{m} \times 5 \mu\text{m}$ . Graphics is courtesy S. Dupont [13].

under a conventional microscope to generate a visible image. Subsequently, the sample is illuminated using an IR SC source, and spatial absorption is recorded in a pixel-wise scanning (raster-scanning) fashion, by translating the  $XYZ$ -stage the sample is mounted on. The experimental setup is shown Fig. 3.21-(a), where focusing optics shine the IR SC onto the sample, and a spectrometer records the resulting spectrum [13]. The generated IR SC illuminating the sample, ranges from  $1.4 \mu\text{m}$  to  $4.0 \mu\text{m}$ , and is created in a ZBLAN SIF with core diameter of  $2a = 7.0 \mu\text{m}$  and a NA of 0.2. It is pumped by a fiber-laser emitting pulses of approximately 1 ps at  $\lambda_p = 1900 \text{ nm}$  with a repetition rate of  $f_{\text{rep}} = 40 \text{ MHz}$ . The spectrum of the SC is shown in Fig. 3.21-(b).

A detector records what wavelengths are being absorbed by the sample, by comparing the signal that has passed the sample, to a reference

measurement of the SC. Fig. 3.20-(b) and (c) shows regions of absorption at  $3.05\ \mu\text{m}$  and  $3.50\ \mu\text{m}$  respectively, where a blue color illustrates regions of high absorption and red region have large transmission at the particular wavelength. Because water absorbs at  $3.05\ \mu\text{m}$ , it is seen in



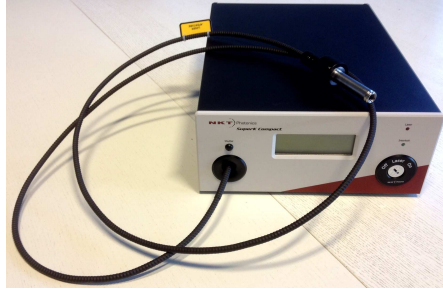
**Figure 3.21:** (a) Schematic of the experimental setup for the IR absorption microscope. (b) Spectrum of the SC used in the measurement. Graphics is courtesy S. Dupont [13].

Fig. 3.20-(b) that the top part of the picture contains water, while as oil absorbs at  $3.5\ \mu\text{m}$  it is seen from Fig. 3.20-(c) that the bottom part contains oil. The middle part transmits light both at  $3.05$  and  $3.5\ \mu\text{m}$  corresponding to an air-bubble. Because the molecular absorption of a sample can be measured in the entire range of the IR SC in a single shot (or a limited number of shots), the microscope shows promise in, e.g., real-time chemical analysis, e.g., in combustion or breath analysis.

### 3.6 The Mid-infrared Supercontinuum Laser Source

Finally, the mid-IR SC source, developed and built at NKT Photonics during this project, is shown in Fig. 3.22. The image shows the MIRCompact, but also a larger model, the MIRPower, exist. It is a portable turn-key prototype that produce the spectrum displayed in blue in Fig. 3.23. The MIRPower, which is of slightly different design, produces a more energetic spectrum than the MIRCompact. The spectrum of the MIRPower is displayed in green in Fig. 3.22. The bandwidths are from  $1.5$  to  $4.2\ \mu\text{m}$  and  $1.5$  to  $4.3\ \mu\text{m}$  for the MIRCompact and MIRPower respectively. Notice how the spectra from the MIR sources show a less pronounced dip in the level of PSD, than the loss band proposed in





**Figure 3.22:** Picture of the celebrated turn-key MIRCompact prototype constructed by P. M. Moselund and C. Petersen at NKT Photonics. Picture is courtesy of NKT Photonics.

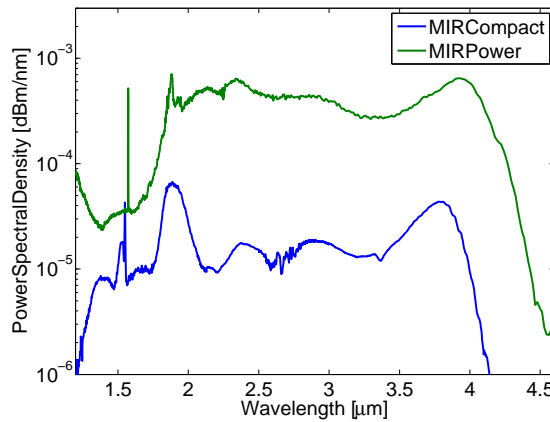


**Figure 3.23:** PSD of the MIRCompact and the MIRPower. Spectra are courtesy of NKT Photonics.

Fig. 3.2 justifies. The fibers used in the MIR sources are produced more recently, and drawing procedures and environment may have improved in the mean time.

This thesis is not the proper place to disclose exactly what fibers or pump sources are used by the MIR SC lasers, nor is it the place to disclose what auxiliary considerations are needed in order to choose them, but considerations like described in section 3.4 show some of the concerns to address during design of a ZBLAN based SC source.

### 3.7 Summary of Chapter 3

In this chapter, the linear propagation properties of the soft-glass ZBLAN has been review, and a suitable measurement of the bulk material refractive index dispersion has been found in literature. It has been argued that among the available profiles, the prediction of the overall shape of the dispersion profile of a drawn fiber is more crucial than knowing the exact location of the ZDW. An uncertainty in the ZDW will typically be on the order of 100 nm, and it has been substantiated that the predicted width of simulated SC spectra are not severely impacted by this. On the other hand, knowledge of the phase-matching between dispersive waves and redshifting solitons is important to predict the blue wavelength edge of the SC, and, it is proposed that a dispersion measurement using a FROG measurement technique in the entire range of SCG, can help retrieve such knowledge.

A loss measurement for a ZBLAN fiber, provided by the fiber manufacturer, was also presented, and it agrees with literature reports on the background attenuation in ZBLAN, while predicting that material absorption starts to increase around 4  $\mu\text{m}$  and dominating SCG at around 4.5  $\mu\text{m}$ . It is speculated that a loss band might be present in the fiber which is not accounted for by the loss measurement. Simulations of SCG are done both with and without an artificially enhanced loss curve that contain a loss barrier centered around 2.9  $\mu\text{m}$ , and results show, to some extent, a better correspondence to measurements, when the loss is included. Such a loss band, in the proposed wavelength region, can be caused by water absorbed in the fiber. To obtain better knowledge of the actual loss, a cutback measurement of the fiber loss in the entire range of interest could be performed.

Furthermore, a measurement of the Raman gain profile in a  $2a = 10.7 \mu\text{m}$ ,  $\text{NA} = 0.2$ , ZBLAN, SIF has been presented in this chapter. The measurement and literature does not agree completely on the magnitude and location of gain bands, and most significantly, another full profile measurement disagrees with the one measured at AU. This other measurement predicts a larger Raman gain for smaller values of the stokes shift and it finds a significantly enhanced value of the fractional contribution from delayed Raman response of  $f_R = 0.24$ , which should be compared to the value of 0.062 found at AU. Simulations performed using their reported Raman response suggests that it might be just slightly overestimated.

The chapter also reviews the spectral development of SC using fs-pumping both in the normal and anomalous dispersion regime, by comparing measurements and simulations of SCG. The fiber used for this is the same ZBLAN fiber also used for measurement of the delayed Raman gain. Simulations find that both normal and anomalous dispersion regime pumping will yield a broad SC spectrum, and that it develops from clear soliton fission in the anomalous dispersion regime. The broadening process is similar in the normal dispersion regime, but here SPM must cause enough light to cross the ZDW and into the anomalous dispersion regime before solitons that redshift are formed. In chapter 5 will be shown examples of ps pumped SCG, and here the main differences are discussed.

Finally, this chapter concludes with the presentation of a possible application for mid IR SC and the final end goal, a turn-key mid-IR laser is shown along with its achievable spectra.

## Chapter 4

# Concatenating Fibers for Continued Nonlinear Effects

As reviewed in chapter 3, the zero dispersion wavelength (ZDW) of bulk ZBLAN is  $1.7\ \mu\text{m}$  [52], and it was demonstrated that the expected ZDW of ZBLAN step-index fibers (SIFs) is often located around  $1.6\ \mu\text{m}$ . Furthermore, the widest supercontinuum (SC) spectra were achieved when pumping in the anomalous dispersion regime. Therefore ytterbium (Yb) and erbium (Er) based pump sources that operate at  $\sim 1.06\ \mu\text{m}$  and  $\sim 1.55\ \mu\text{m}$ , respectively, are not the ideal pump sources for ZBLAN based infrared (IR) SC, because they are in the normal dispersion regime. Fiber sources based on thulium (Tm) that have an operating wavelength range between 1650 and 2100 nm [76], is a more natural choice for a pump source, but the Tm technology is less developed, and lack of optical components make Yb and Er lasers more attractive in a commercial system.

In chapter 3 was pointed to a number of research publications, e.g., [47, 48], where it is suggested to use an Er based source in spite of it being in the normal dispersion regime of most ZBLAN fibers. It is suggested to overcome this by using a silica fiber, with anomalous dispersion at the Er wavelength, as an intermediate and passive component that redshifts the pump pulse, before it is coupled into the nonlinear fiber. The nonlinear soliton matching (NLSM)-scheme reviewed in this chapter, and introduced in [32], was conceived during a discussion of the design of such tunable laser sources for pumping ZBLAN fibers above their ZDWs, by use of standard Er fiber laser technology. The discussion was based on considerations about what was more important when choosing fibers, whether the

linear properties, e.g., mode-field diameter (MFD) matching and refractive index matching are more important than to consider the nonlinear properties of the fibers. When coupling light between two optical fibers, the linear properties are typically matched in order to avoid loss of power during the coupling [1,77]. When coupling solitons between two nonlinear fibers however, and expecting continued nonlinear dynamics, preservation of the soliton number becomes an equally important matching requirement.

In this chapter, it is reviewed how the NLSM-scheme gives a quantification of the expected behaviour of soliton related dynamics after coupling of solitons between nonlinear optical fibers. The proposed NLSM-scheme is generic, and it serves equally well for other wavelength ranges, or other fiber materials than used while demonstrating it here. The demonstration is done using suitable but imaginable fibers, because the scheme has not yet been demonstrated in practise. Also in this chapter is given an account for the second soft-glass material, tellurite, briefly considered during this project work, and its properties are discussed in section 4.1.1.

## 4.1 Coupling of Solitons Between Nonlinear Fibers

The generic concept of the NLSM between two nonlinear fibers is illustrated in Fig. 4.1 [32]. Here a fundamental soliton (soliton number  $N = N_1 = 1$ ) at pump wavelength  $\lambda_p$  is launched into fiber 1 where it undergoes an initial redshift (Fig. 4.1 bottom) until a desired coupling wavelength  $\lambda_c$ . Subsequently the redshifted soliton is coupled into fiber 2, where it has a corresponding soliton number  $N = N_2$ . There are then three scenarios depending on the soliton number  $N_2$ : (1) If  $N_2 < 1/2$  there is not enough power to excite a soliton in fiber 2 (Fig. 4.1 top left). In this case the spectral content of the pulse will not change, but the pulse will spread temporally due to linear effects only. (2) If  $1/2 < N_2 < 3/2$  (Fig. 4.1 top middle) the pulse will remain a fundamental soliton in fiber 2. This case of continued fundamental soliton propagation gives a large conversion of energy from the input pulse at the beginning of fiber 1 and to the redshifted soliton at the end of fiber 2. (3) If  $N_2 > 3/2$  (Fig. 4.1 top right) a higher order soliton is excited, which will undergo soliton fission or pulse breakup, and subsequent soliton self-frequency shift (SSFS) and dispersive wave generation. A breakup of the fundamental soliton caused

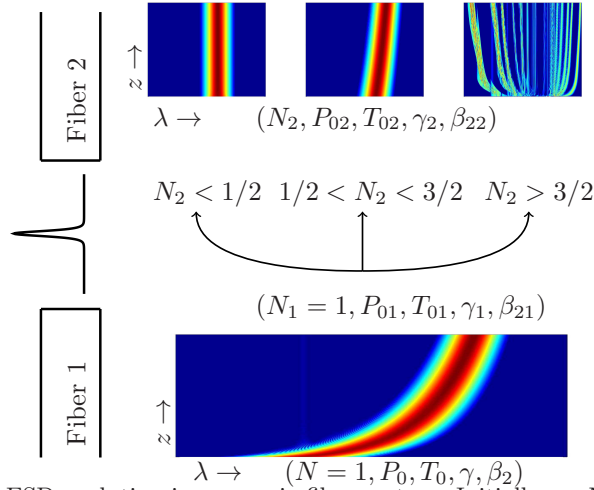


**Figure 4.1:** ESD evolution in a generic fiber system: Initially an  $N = 1$  soliton redshifts in fiber 1, and the output is coupled into fiber 2.

by soliton fission will reduce the amount of energy converted from the input soliton wavelength to the wavelength of the most redshifted soliton, but it increases the total amount of soliton redshift.

For demonstrating the NLSM-scheme two idealized systems of concatenated fibers are considered. In both systems, fiber 1 is taken to be a silica photonic crystal fiber (PCF) with a pitch  $\Lambda = 3.3 \mu\text{m}$ , seven rings of air-holes, and a ratio between air hole diameter  $d$  and pitch  $d/\Lambda = 0.52$  (see chapter 2). Material dispersion for fused silica is found in the literature [18]. The fiber has a calculated ZDW of 1033 nm, and the value for the nonlinear refractive index is  $n_2 = 2.6 \cdot 10^{-20} \text{ m}^2/\text{W}$  [6]. Fiber 2 is either a ZBLAN or a tellurite PCF, and in the following, fiber 2a is the designation for the ZBLAN PCF and fiber 2b is the tellurite PCF. Material dispersion for ZBLAN is found in [52], as in chapter 3, while material dispersion of tellurite is found from [78].

#### 4.1.1 Tellurite Soft-glass Material

Before continuing with the demonstration of the NLSM-scheme, it is appropriate to consider the second soft-glass material studied in this work, which is tellurite. Tellurite is also a composite material like ZBLAN, and the composition considered here is  $70\text{TeO}_2 - 10\text{Na}_2\text{O} - 20\text{ZnF}_2$  [78]. The refractive index is shown in Fig. 4.2-left, and here is also plotted the bulk material dispersion, calculated using Eq. (2.2.8) giving a ZDW of

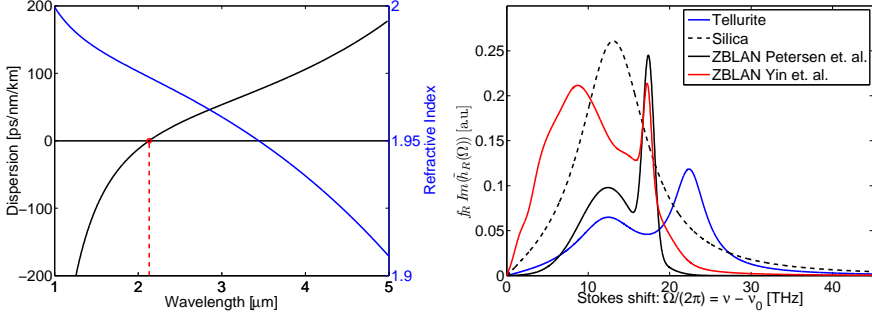


**Figure 4.2:** Left: Refractive index (blue) and dispersion (black) of bulk tellurite [78]. Right: Comparable delayed Raman response for tellurite [78], ZBLAN and silica.

2.13  $\mu\text{m}$ . A tellurite fiber preform that contains an air hole pattern can be created, e.g., by extrusion, and in this way tellurite PCFs have been demonstrated [79]. Creating a PCF from tellurite has been shown to decrease the ZDW from the bulk value, and a ZDW of 1780 nm has been found for a four ring triangular PCF [78]. The nonlinear refractive index of tellurite is  $n_2 = 5.9 \cdot 10^{-19} \text{ m}^2/\text{W}$  [8], and tellurite is thus approximately a factor of 25 – 30 more nonlinear than silica and ZBLAN, thus making it a promising candidate for supercontinuum generation (SCG). The tellurite modelled in this work has a fractional Raman contribution of  $f_R = 0.064$  and the Raman response given in [8], is fitted with a weighted sum of two damped harmonic oscillators of the form

$$h_R(T) = f_1 \frac{\tau_1^2 + \tau_2^2}{\tau_1 \tau_2^2} e^{-\frac{t}{\tau_2}} \sin\left(\frac{t}{\tau_1}\right) + f_2 \frac{\tau_3^2 + \tau_4^2}{\tau_3 \tau_4^2} e^{-\frac{t}{\tau_4}} \sin\left(\frac{t}{\tau_3}\right) \quad (4.1.1)$$

with weights  $f_1 = 0.36$ ,  $f_2 = 0.64$ , and time constants  $\tau_1 = 7.1 \text{ fs}$ ,  $\tau_2 = 66.6 \text{ fs}$ ,  $\tau_3 = 13 \text{ fs}$ , and  $\tau_4 = 34.3 \text{ fs}$  [78]. In Fig. 4.2-right is shown the comparable Raman gain per nonlinearity  $f_R \text{Im}(h_R)$  for tellurite along with the two proposed measurements of the delayed Raman gain in ZBLAN, reviewed in chapter 3, and silica [6] for comparison.

Somewhat similar to ZBLAN, tellurite should be able to guide light to approximately  $\sim 4.5 \mu\text{m}$ , but the material absorption is highly influenced by the fabrication environment, and a broad and large absorption band has been identified in tellurite centered at 3.3  $\mu\text{m}$ , with tails stretching both to longer and shorter wavelengths [78]. Indeed, extruded PCF preforms were obtained by the Technical University of Denmark (DTU)

from an institutional collaborator, and these were drawn into fibers at the DTU draw tower facility. An example of a drawn PCF is shown in the microscope image in Fig. 4.3. The core region is approximately  $5\ \mu\text{m}$ .

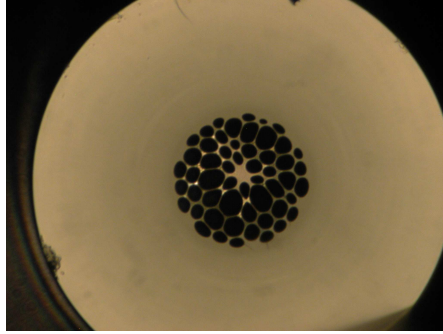


**Figure 4.3:** Microscope image of a tellurite PCF drawn from a preform at the DTU draw tower facility by Scott Yuan. The core diameter is approximately  $5\ \mu\text{m}$ .

Fiber samples were sent to our collaborators at Aarhus University (AU) for measurements of SCG, using the experimental setup discussed in chapter 3, but coupling light into the fibers proved extremely difficult, and furthermore, large loss as described in [78] impeded the material severely and it never was a success to use tellurite fibers. Nonetheless tellurite is considered for the theoretical demonstration of the NLSM-scheme, and wideband SCG has been demonstrated using tellurite, e.g., in [80], though under different conditions than considered here.

#### 4.1.2 Nonlinear Soliton Matching

The idealized equation, governing solitons is the nonlinear Schrödinger equation (NLSE), and the idealized soliton concept was briefly discussed in chapter 2. When influenced by the delayed Raman response, solitons redshift [42], and the governing equation is the generalized nonlinear Schrödinger equation (GNLSE). Thus, to demonstrate the NLSM-scheme, an ideal soliton is used as the input, or initial condition, for solving the GNLSE, firstly over  $L = 10\ \text{m}$  of propagation in fiber 1. The soliton is characterized by the soliton number, which was also defined in chapter 2,  $N^2 = \gamma P_0 T_0^2 / |\beta_2|$ , and the ideal fundamental soliton has a peak power adjusted so that  $N = 1$ . In the following is used a soliton with a central wavelength  $\lambda_p = 1550\ \text{nm}$ , and full-width-at-half-



maximum (FWHM) pulse duration of  $T_{\text{FWHM}} = 50$  fs, corresponding to an ultra fast Er laser source. Mathematically, the initial condition is given as

$$A(0, T) = \sqrt{P_0} \text{sech} \left( \frac{T}{T_0} \right) \quad (4.1.2)$$

where the peak power is  $P_0 = |\beta_2|/(\gamma T_0^2)$ , when  $N = 1$ . For the demonstration purpose of the NLSM-scheme considered here, no noise has been added to the input, thereby eliminating the need for ensemble averaging. Furthermore, since the essence of the NLSM is the coupling itself, and the wavelengths considered, at least until soliton fission occurs, are less than  $2 \mu\text{m}$ , propagation loss is ignored in both fiber 1 and 2, in spite of large losses for wavelengths longer than  $3 \mu\text{m}$  in tellurite. To determine the development of the electric field envelope, the GNLSE is solved, as proposed in chapter 2. The simulated result for soliton propagation in fiber 1 is shown in Fig. 4.4 (and in the bottom of the contour plots shown in Fig. 4.7-left and -right), where the redshift is clearly demonstrated by

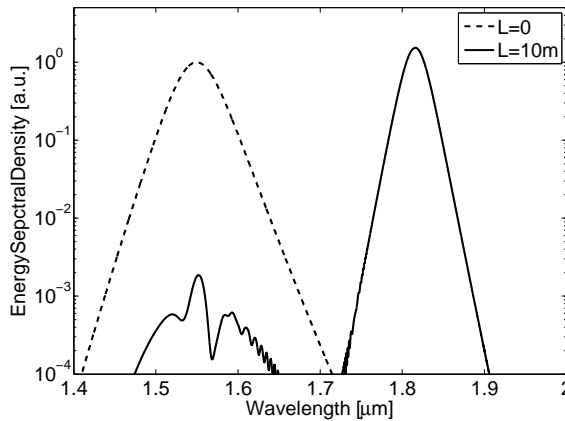


**Figure 4.4:** Input and output for an ideal fundamental soliton propagating in 10 m of fiber 1. The center wavelength changes from  $\lambda_p = 1550$  nm and to  $\lambda_c = 1816$  nm.

a change in central wavelength from 1550 nm and to  $\lambda_c = 1816$  nm after 10 m of propagation, while the soliton continuously adjusts its pulse width and peak power to preserve the soliton number, so at the output of fiber 1,  $N_1 = 1$  (see Fig. 4.1 for notation and Table 4.1 for values). Using

Fiber	$j$	$A_{\text{eff},j}$ [ $\mu\text{m}^2$ ]	$\beta_{2j}$ [ $\frac{\text{ps}^2}{\text{km}}$ ]	$T_{\text{FWHM},j}$ [fs]	$P_{0j}$ [kW]	$N_j$
1-in		14.2	-77.9	50.0	13.08	1.00
1-out	1	15.0	-134.2	122.5	4.58	0.99
2a-in	2	9.0	-53.2	122.5	4.58	9.73
2b-in	2	14.7	-77.2	122.5	4.58	1.22

**Table 4.1:** Pulse and derived parameters used in calculations [32]. See Fig. 4.1 for notation.

that  $N_1 = 1$ , one has the relation

$$N_1^2 = \frac{T_{01}^2 P_{01} \gamma_1}{|\beta_{21}|} = 1 \quad (4.1.3)$$

where  $T_{01}$  and  $P_{01}$  are the pulse width and peak power of the soliton at the output of fiber 1, respectively. An adiabatic soliton coupling is assumed, which preserves the pulse shape when passing the interface, but can decrease the peak power. Thus, it is reasonable to assume that,  $T_{02} = T_{01}$  where  $T_{02}$  is the soliton pulse width at the input of fiber 2. Linear loss mechanisms, e.g., Fresnel reflection and MFD mismatch dictates that  $P_{02} = \eta P_{01}$ , where  $0 \leq \eta \leq 1$  is the power coupling efficiency.

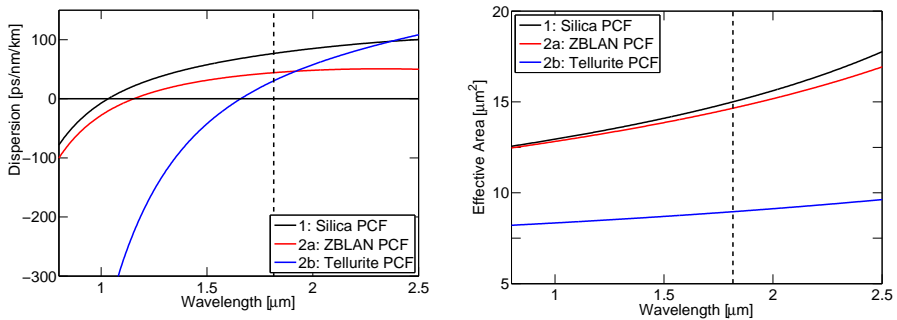


**Figure 4.5:** Left: The calculated dispersion of fiber 1, 2a and 2b. Right: Effective area  $A_{\text{eff}}$  of fiber 1, 2a and 2b. Vertical line marks the coupling wavelength  $\lambda_c = 1816$  nm.

Using this, a nonlinear coupling coefficient is defined as

$$\eta_{\text{NL}}^2 = \frac{N_2^2}{N_1^2} = \frac{T_{02}^2 P_{02} \gamma_2 / |\beta_{22}|}{T_{01}^2 P_{01} \gamma_1 / |\beta_{21}|} = \eta \left( \frac{\gamma_2 / |\beta_{22}|}{\gamma_1 / |\beta_{21}|} \right) \quad (4.1.4)$$

which is given in terms of material parameters, fiber dispersion, and the power coupling efficiency  $\eta$  only. The nonlinear coupling coefficient  $\eta_{\text{NL}}$  is then decoupled from the pulse width and peak power. In the case considered here, when coupling a fundamental soliton from fiber 1 into fiber 2,  $\eta_{\text{NL}}$  is equivalent to the factor by which the soliton number changes across the interface.

To calculate the nonlinear coupling coefficient for specific examples, fiber 2a is now taken to have a pitch of  $\Lambda = 3.3 \mu\text{m}$  and an air-hole to pitch ratio of  $d/\Lambda = 0.52$ . The ZDW of fiber 2a is calculated to be  $1.15 \mu\text{m}$ , and similarly fiber 2b is taken to have a pitch of  $\Lambda = 3.5 \mu\text{m}$  and  $d/\Lambda = 0.8$ . The ZDW of fiber 2b is calculated to be  $1.66 \mu\text{m}$ . The dispersion curves and effective areas for all fibers are plotted in Fig. 4.5-left and -right for comparison. Notice the locations of the ZDW and the difference in effective area. This difference, particularly between fiber 1 and fiber 2b, will cause a MFD mismatch. In Fig. 4.6 is shown the nonlinear coupling coefficient  $\eta_{\text{NL}}$  for fiber 2a and 2b as function of wavelength. Notice that

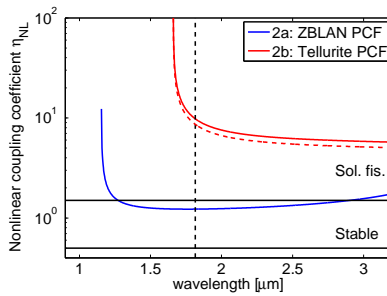


**Figure 4.6:** Nonlinear coupling coefficient,  $\eta_{\text{NL}}$  for fiber 2a and fiber 2b. Solid curves are for  $\eta = 1$  and dashed is for  $\eta = \eta_{\text{MFD}}(\lambda_c)$ . The dashed vertical line marks  $\lambda_c = 1816 \text{ nm}$ , and the horizontal lines mark the soliton propagation regimes.

$\eta_{\text{NL}}$  is singular at  $\beta_{22} = 0$ , thus  $\eta_{\text{NL}} \rightarrow \infty$  at the ZDW of fiber 2. The black horizontal solid lines in Fig. 4.6 mark the quantitative bands defined by the NLSM-scheme:

- Linear regime: - The nonlinear coupling coefficient  $\eta_{\text{NL}} < 1/2$ , and no further spectral changes is induced to the propagating pulse due to nonlinear effects.
- Stable regime: - Here,  $1/2 < \eta_{\text{NL}} < 3/2$ , and a stable soliton is expected to continue propagation and further redshift in fiber 2.
- Sol. fis. regime: - Finally,  $3/2 < \eta_{\text{NL}}$ , and soliton fission or pulse breakup is expected to occur.

Propagation is continued in fiber 2, by using the calculated pulse at the end of fiber 1, as initial condition for a restarted simulation of the GNLSE with fiber parameters for fiber 2a and 2b respectively. The full spectral development from input in fiber 1 and to the end of fiber 2a and 2b is shown in the contour plots of Fig. 4.7. From Fig. 4.6 it is clearly seen that the NLSM condition for stable continued propagation is satisfied for the fiber 1  $\rightarrow$  2a coupling where  $1/2 < \eta_{\text{NL}} < 3/2$  ( $\eta_{\text{NL}} = 1.22$ ). The stable propagation of a redshifting fundamental soliton is confirmed in Fig. 4.7-left. The central wavelength increases further from  $\lambda_c = 1816$  nm to 1857 nm, and approximately 83% of the energy from the input pulse is converted to this wavelength. For the matching between fiber 1 and 2b, however, it is found that  $\eta_{\text{NL}} \gg 3/2$  ( $\eta_{\text{NL}} = 9.73$ ) and consequently, soliton fission is expected to occur in fiber 2b. Simulation results for propagation in 10 m of fiber 1 and 8 m in fiber 2b are shown in Fig. 4.7-right. Also here it is clearly confirmed that after a short distance of propagation in fiber

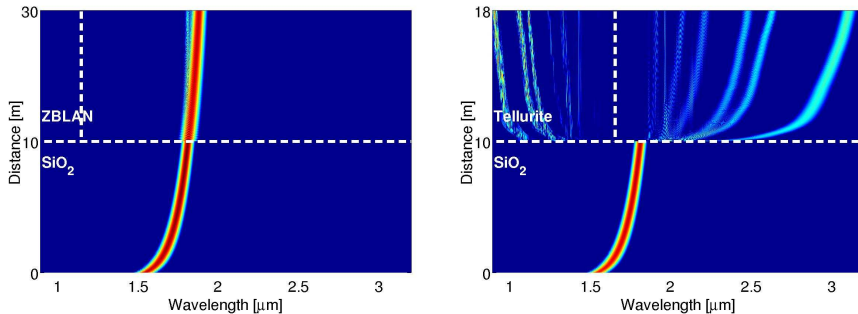


**Figure 4.7:** Left: Evolution of the ESD in fiber 1 and fiber 2a, where  $\eta_{\text{NL}} = 1.22$ , and a fundamental soliton propagates throughout the system. Right: Evolution of the ESD in fiber 1 and fiber 2b, where  $\eta_{\text{NL}} = 9.73 \gg 3/2$  and a higher order soliton undergoes soliton fission. In both simulations the power coupling efficiency is assumed to  $\eta = 1$ . White vertical line marks the ZDW of fiber 2.

2b, soliton fission causes a breakup of the pulse, and generates multiple separated solitons. The central wavelength of the most redshifted soliton becomes  $\lambda = 3103$  nm in this case, and approximately 18% of the energy in the input soliton has been converted to this wavelength.

In the calculation shown in Fig. 4.7-left and -right it has been assumed that  $\eta = 1$  and the power is coupled perfectly from fiber 1 and into fiber 2. The power coupling efficiency, however, depends on a number of factors, and a reduced power coupling can, e.g., be due to imperfect matching of the MFDs. For Gaussian shaped modes, the coupling loss from MFD mismatch can be estimated from [77]

$$\eta_{\text{MFD}} = 4 \frac{A_{\text{eff},1}^2 A_{\text{eff},2}^2}{(A_{\text{eff},1}^2 + A_{\text{eff},2}^2)^2} \quad (4.1.5)$$

but it should be noted that the modes in PCFs are not completely Gaussian shaped, but Eq. (4.1.5) is used as an approximation to the coupling efficiency. Furthermore, Fresnel reflections can occur when coupling between materials of different refractive indexes, and in a laboratory environment, there can be other causes, limiting the power coupling. However, using the effective areas from Table 4.1 gives a power coupling efficiency of  $\eta_{\text{MFD}} = 99\% \approx 1$  for the fiber 1 $\rightarrow$  2a coupling and  $\eta_{\text{MFD}} = 77\%$  for the fiber 1 $\rightarrow$  2b coupling, both calculated at  $\lambda = \lambda_c = 1816$  nm. As indicated by Eq. (4.1.4), inclusion of the power coupling efficiency lowers the NLSM curve by a factor of  $\sqrt{\eta_{\text{MFD}}}$ . In Fig. 4.6 is shown the NLSM curve for the fiber 1 $\rightarrow$  2b coupling both with  $\eta = 1$  and  $\eta = \eta_{\text{MFD}}$  calculated from Eq. (4.1.5) and it is seen to have limited effect, and does not decide the propagation regime in fiber 2. By design of the waveguide dispersion and choice of nonlinear fiber material, it is also possible to compensate for the linear power reduction from MFD mismatch, and it is thus concluded that NLSM takes precedence over MFD matching, and that matching of nonlinear properties are the first consideration that is needed when designing a system based on continued nonlinear dynamics by coupling between fibers.

Even though, it may seem an idealized situation to have coupling of a nearly fundamental soliton with  $N \approx 1$ , it is quite general because breakup of an energetic pulse, as often observed in SCG, will cause a higher order soliton, excited from the input of fiber 1, to break up into its constituent solitons [14, 37]. Thus, provided fiber 1 is long enough for the pulse break up to occur, Eq. (4.1.4) will predict the behaviour of continued soliton propagation quite generally.

The regimes defined by the NLSM-scheme can be used depending on the expected outcome of SCG in a concatenated fiber system. If a large redshift is wanted, where an energetic carrier wave, e.g., a pump, is wavelength shifted, the design of a concatenated system should aim for a nonlinear coupling coefficient in the stable regime defined above, i.e.,  $1/2 < \eta_{\text{NL}} < 3/2$ . This could be the case, when choosing fibers for an Er based fiber laser, redshifted to pump a ZBLAN SIF above its ZDW. If instead, a large redshift or a broad SC is wanted, then fibers should be designed to aim for a nonlinear coupling in the regime where  $\eta_{\text{NL}} \gg 3/2$ . Such considerations could be useful, e.g., when coupling an entire SC spectrum, developed in a ZBLAN fiber, into, e.g., a highly nonlinear chalcogenide fiber for further broadening into the mid-IR.

## 4.2 Summary of Chapter 4

In this chapter was proposed a quantity, the nonlinear coupling coefficient  $\eta_{\text{NL}}$ , that describes the coupling of fundamental solitons across a generic fiber interface. The proposed NLSM-scheme does not depend on specific pulse parameters, e.g., pulse duration and peak power, but instead it depends only on material and fiber parameters. In this sense, it is a specific design parameter that can be used for optimization of fiber waveguide systems for, e.g., large redshifts of stable solitons or for wide band SCG. The NLSM-scheme defines two regimes of expected nonlinear dynamics, i.e., the stable soliton regime, which can be used to obtain a large energy conversion from input to output, or, if a large redshift is wanted instead, the second regime should be employed. Numerical simulations on example fibers and a possible laboratory pump source are carried out, and confirm the validity of the defined regimes. Finally it is concluded that design of dispersion and nonlinear properties combined, take precedence over considerations leading to efficient power coupling when designing a concatenated laser system, even though such considerations might also be important.

In this chapter is also discussed the linear properties of tellurite, which is the second soft-glass material considered during this project work. As mentioned, PCF preforms were obtained for tellurite fibers, and fibers were drawn at DTU, but unfortunately large levels of loss and troublesome in-coupling of light prevented tellurite from being pursued any further. Instead, the focus is now changed to the final soft-glass material considered in this work, which is chalcogenide that is treated in chapter 5.



## Chapter 5

# Supercontinuum up to $12\ \mu\text{m}$ in Chalcogenide Fibers

In this chapter it is investigated if the long wavelength edge of light that is generated by supercontinuum (SC) can be extended beyond the  $\sim 4.5\ \mu\text{m}$  limit found in chapter 3. To achieve this, the last soft-glass material to be considered in this work is introduced. Chalcogenide glasses compose a series of compound glasses [81], but typically either  $\text{As}_2\text{S}_3$  or  $\text{As}_2\text{Se}_3$  or possibly germanium (Ge) doped combinations, are used in fiber optics. Particularly the compound  $\text{As}_2\text{Se}_3$  has a transmission window that has been reported to stretch as far as  $17\ \mu\text{m}$  [81]. Extending the long wavelength edge of SC light sources far into the mid-IR will open for numerous applications inaccessible to sources limited to  $\sim 4.5\ \mu\text{m}$ . Proteins and lipids show absorption from around  $3\ \mu\text{m}$  to above  $9\ \mu\text{m}$  [11], thus, provided sufficient average power is delivered, a SC source covering this range could be applicable to, e.g., quality control of agricultural, dairy, and pharmaceutical productions. Similarly, a SC source covering this wide a range may prove useful in biochemical analysis by enabling identification of bio-molecular spectral signatures, and it has been proposed that such a source can be used in devices for in-vivo and non-invasive optical biopsies, useful in early cancer detection [12].

Chalcogenide enables the generation of mid-IR SC to above  $10\ \mu\text{m}$  due to its wide transmission window, and because the nonlinear refractive index  $n_2$  is between 200 and 1000 times larger than for silica and ZBLAN, depending on the content of sulfur (S) or selenium (Se) [9,10]. One viable path suggested for obtaining a broadband SC in chalcogenide, is a low threshold SC generated in tapered chalcogenide fibers [82]. This leads



to small core fibers with limited power handling capabilities, and here, a path leading to higher average power levels, more ideally suited for applications, is pursued by using large core fibers.

In this chapter is presented the linear properties of chalcogenide (only  $\text{As}_2\text{Se}_3$  is considered) and both photonic crystal fibers (PCFs) and step-index fibers (SIFs) are studied for potential use in a SC source. Dispersion engineering of PCFs enables a large shift of the zero dispersion wavelength (ZDW) compared to the bulk material, thus enabling seed lasers at wavelength less than 3  $\mu\text{m}$  to pump in, or near to, the anomalous dispersion regime of such fibers. After PCFs have been considered, SIFs are investigated by modelling a  $\lambda_p = 4.5 \mu\text{m}$  praseodymium (Pr) doped chalcogenide fiber laser as pump source simulated for supercontinuum generation (SCG). It is predicted that infrared (IR) SC ranging between 4 and 12  $\mu\text{m}$  is achievable, and that the long wavelength edge of such SC will ultimately be determined by the long wavelength loss edge of a realised fiber.

## 5.1 Chalcogenide Fiber Design

As was reviewed in chapter 3, the material absorption becomes large for wavelengths longer than 4.5  $\mu\text{m}$  in ZBLAN, and the long wavelength edge of ZBLAN based SC cannot extend much further. A similar reason was valid for silica based SC sources that are limited to approximately 2.4  $\mu\text{m}$ . The transmission window of chalcogenide, however, has been reported to extend far into the IR, though different accounts have been given for the achievable IR transmission properties [83–85]. In [83] the loss is reported to increase after 12  $\mu\text{m}$  while [84] reports a loss of  $0.01 \text{ cm}^{-1}$  at  $\sim 17 \mu\text{m}$  and [85] finds the transmission window is between 1 and 10  $\mu\text{m}$  for  $\text{As}_2\text{Se}_3$ . Regardless, the chalcogenide fiber technology is a developing technology as the ZBLAN technology is, and here is used a frequency constant background material loss of 1 dB/m, because an institutional partner, from the University of Nottingham [86], show promising results for the possibility of producing SIFs from chalcogenide with material losses of this magnitude. Thus, in this chapter, the total attenuation used in simulations is calculated as

$$\alpha_{\text{tot}}(\omega) = \alpha_{\text{mat}} + \alpha_g(\omega) \quad (5.1.1)$$

where  $\alpha_{\text{mat}} = 1 \text{ dB/m}$  is the material loss and  $\alpha_g$  is the guiding attenuation calculated using Comsol (see chapter 2) for the particular fiber under

consideration.

Two measurements are available for the bulk material refractive index properties of chalcogenide [83,86], and Fig. 5.1 shows the wavelength

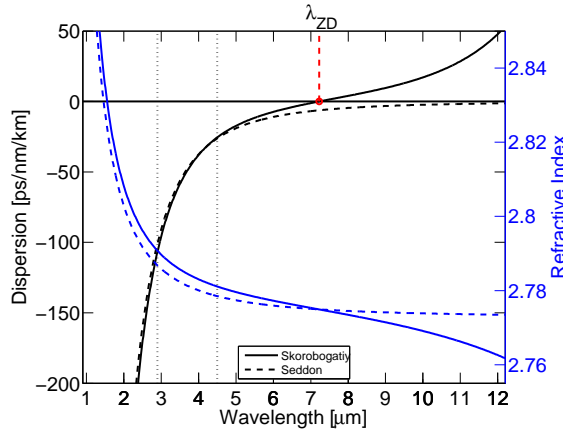


**Figure 5.1:** Blue: material refractive index wavelength dependence for chalcogenide ( $\text{As}_2\text{Se}_3$ ) [83,86]. Black: calculated bulk dispersion. Solid (dashed) line is for the Sellmeier polynomial by Skorobogatiy *et. al.* [83] (Seddon *et. al.* [86]). The bulk material ZDW is calculated to be  $\lambda_{\text{ZD}} = 7.22 \mu\text{m}$  [83]. The dotted vertical lines mark the two considered pump wavelengths at  $2.9 \mu\text{m}$  and  $4.5 \mu\text{m}$  respectively.

dependence of the refractive index obtained from these measurements as blue curves. Solid lines are for a measurement by Skorobogatiy *et. al.* [83], while dashed lines are for the measurement provided by A. Seddon *et. al.* from the University of Nottingham [86]. The measurements are fitted to a Sellmeier equation, given by Eq. (2.2.5), and the parameters for the Sellmeier fit for the two different measurements are listed in Table 5.1. Also shown in Fig. 5.1, in black curves, are the correspondingly calculated bulk group-velocity dispersion (GVD) curves (see Eq. (2.2.8)). The ZDW calculated from the measurement by Skorobogatiy *et. al.* is  $\lambda_{\text{ZD}} = 7.22 \mu\text{m}$ , while the measurement by Seddon *et. al.* [86] shows all normal dispersion in the bulk material. In chapter 3 it was demonstrated how it is advantageous to pump directly in the anomalous dispersion regime, preferably close to the ZDW, enabling soliton dynamics at an early stage of propagation. However, it was also observed that one can obtain a SC by normal dispersion regime pumping, if nonlinear effects shift enough light from an energetic pump pulse near the ZDW into the

Ref.	$j$	$A_j$ [ $\mu\text{m}^2$ ]	$a_j$ [ $\mu\text{m}$ ]
[83]	1	4.99487	0.24164
	2	0.12072	19
	3	1.71237	$2a_1$
[86]	1	0.61989	0.543873
	2	6.067837	0.277139

**Table 5.1:** Coefficients for the Sellmeier Eq. (2.2.5) [83, 86].

anomalous dispersion regime. Due to the large  $n_2$  and strong Raman response in chalcogenide, a higher order Stokes-shifted Raman line can cross the ZDW and generate light in the anomalous dispersion regime [87, 88]. This will be the exclusive case studied in this chapter, and to this end, two different model laser systems that are proposed to be developed during the future project collaboration of MINERVA [12], are modelled as pump sources. The location of the ZDW at a long wavelength rules out the conventional ytterbium (Yb), erbium (Er) and thulium (Tm) sources that are too deep in the normal dispersion regime to be candidates for generating SC as far as 12  $\mu\text{m}$ , and therefore one of the model lasers is a  $Q$ -switched Er:ZBLAN fiber laser pumping at  $\lambda_p = 2.9 \mu\text{m}$ . The second proposed laser is an actively mode-locked ns-pulsed fiber laser with a Pr doped chalcogenide fiber cavity operating at  $\lambda_p = 4.5 \mu\text{m}$  [12]. Power levels in the range of tens of kW's can be achieved from the well proven Er/Yb-technologies, and a peak power of 1 kW should be achievable in a mode-locked Pr laser, though the technology is an emerging technology [12].

### 5.1.1 Chalcogenide Photonic Crystal Fibers

Because the ZDW is at 7.22  $\mu\text{m}$  strong waveguide dispersion engineering is needed in order to enable a pump laser at  $\lambda_p = 2.9 \mu\text{m}$  to be near the ZDW. Chalcogenide, however, can be drawn into PCFs, and both PCFs with a chalcogenide-air cladding [89] and all solid PCFs have been demonstrated [90]. In Fig. 5.2-left is shown the dispersion properties for a triangular lattice air-hole PCF with  $d/\Lambda = 0.8$  for different values of the pitch  $\Lambda$  (see chapter 2) calculated using Sellmeier data from [83]. The tailoring of dispersion properties enabled by PCFs is clearly witnessed, and the ZDW is lowered significantly from the bulk value, which is marked

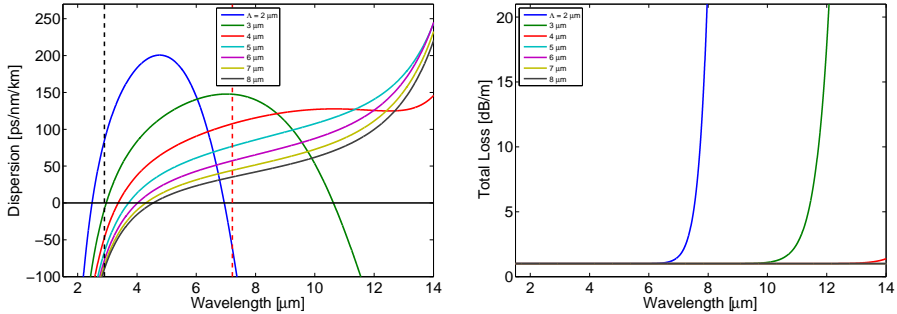


**Figure 5.2:** Left: Dispersion of PCFs with  $d/\Lambda = 0.8$  for different values of the pitch  $\Lambda$  calculated using material data from [83]. Vertical black (red) lines mark the a pump wavelength of  $\lambda_p = 2.9$   $\mu\text{m}$  (bulk material ZDW). Right: Confinement loss  $\alpha_g$  calculated for the fibers in the left panel.

by the red dashed vertical line in Fig. 5.2-left. The calculated confinement loss, displayed in Fig. 5.2-right dictates that for  $d/\Lambda = 0.8$  one should not go below a pitch of  $\Lambda = 4$   $\mu\text{m}$ , or the guiding loss will increase abruptly at wavelengths lower than 12  $\mu\text{m}$ . The fiber with a ZDW closest to  $\lambda_p = 2.9$   $\mu\text{m}$ , which is not impeded by guiding loss before 12  $\mu\text{m}$ , is the  $\Lambda = 4$   $\mu\text{m}$  fiber that have a ZDW calculated to be 3.37  $\mu\text{m}$ . Such a fiber could be useful with the proposed Er:ZBLAN fiber laser operating at 2.9  $\mu\text{m}$ , however, here is not performed any calculations of SCG in chalcogenide PCFs, but instead, focus is turned to SIFs.

### 5.1.2 Chalcogenide Step-index Fibers

The absolute value of the refractive index of chalcogenide is  $\sim 2.75$ , and this value facilitates the fabrication of SIFs with higher values of the numerical aperture (NA) (see Eq. (2.2.1)) than when comparing to silica and ZBLAN fibers, where the refractive index is  $\sim 1.45$ . Particularly a  $\text{NA} = 0.45$  chalcogenide SIF has been used in reference [10], and larger values of the NA are expected from the collaboration with Nottingham University [86]. The waveguide dispersion is not as strong in SIFs as it is in PCFs, and consequently a pump source for a SIF-based SC source must operate at wavelengths closer to the ZDW of the bulk material. For this purpose, the Pr-doped fiber laser, mentioned in section 5.1, that operate at 4.5  $\mu\text{m}$ , is considered. To find a suitable SIFs candidate for a nonlinear fiber at this pump wavelength, three different SIFs are studied

with core diameters of 5, 10 and 20  $\mu\text{m}$  respectively. The smaller core fibers facilitate a higher nonlinearity due to small core areas, but as also discussed above and in chapter 3, confinement loss will possibly impair the guiding properties at long wavelengths. A large core fiber enables easier in-coupling of the pump laser light and the power handling is improved, but at the expense of a decreased effective nonlinearity. Power handling is an important consideration for highly nonlinear materials like chalcogenide, because an increased nonlinear coefficient generally lowers the threshold for detrimental self-focusing effects [91].

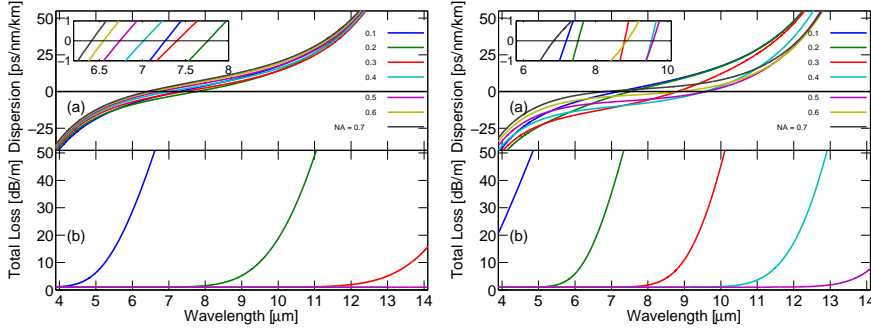


**Figure 5.3:** (a) Dispersion for the  $2a = 20 \mu\text{m}$  (left) and for the  $2a = 10 \mu\text{m}$  (right) chalcogenide SIF for different values of NA. The inset shows the ZD crossings. (b) Total loss for the  $2a = 20 \mu\text{m}$  (left) and for the  $2a = 10 \mu\text{m}$  (right), for different values of NA. All curves are calculated using the Skorobogatiy *et. al.* material dispersion [83].

In Figs. 5.3(a)-left and -right are shown the calculated dispersion in a  $2a = 20 \mu\text{m}$  and a  $2a = 10 \mu\text{m}$  SIF respectively, for different values of the NA using the Sellmeier reported by Skorobogatiy *et. al.* [83], and Figs. 5.3(b)-left and -right show the corresponding total attenuation given by Eq. (5.1.1). In Fig. 5.3(b)-left and -right is clearly seen that decreasing the core size increases the total loss for long wavelengths. Similar waveguide characteristics can be calculated for the  $2a = 5 \mu\text{m}$  fiber, and a summarizing comparison between the three fiber geometries is shown in Fig. 5.4. In Fig. 5.4(a) is shown the ZDW as function of NA, in Fig. 5.4(b) is shown the value of the dispersion  $D$  at the pump wavelength  $D_{4.5} = D(\lambda_p)$  and in Fig. 5.4(c) is plotted a figure of merit for the long wavelength attenuation edge, defined as the wavelength  $\lambda_{3\text{dB}}$  where the total attenuation is  $\alpha_{\text{tot}}(\lambda_{3\text{dB}}) = 3 \text{ dB/m}$ . Based on Fig. 5.4(c) it is found that loss dismisses the  $2a = 5 \mu\text{m}$  SIF as a candidate for SCG

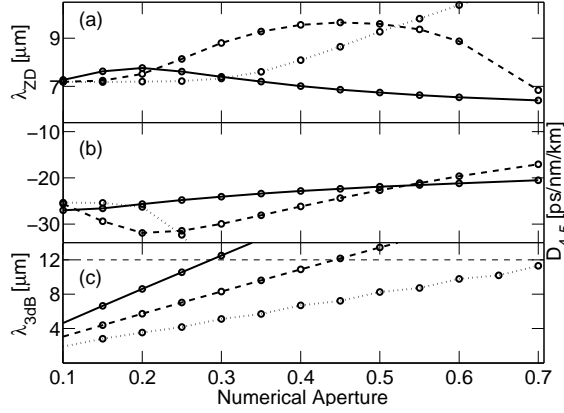


**Figure 5.4:** (a) ZDW  $\lambda_{ZD}$ , (b) Dispersion at pump wavelength  $D_{4.5} = D(\lambda_p)$ , and (c) the 3 dB/m total attenuation edge  $\lambda_{3dB}$  as function of NA. In all graphs, solid (dashed) [dotted] line is for  $2a = 20 \mu\text{m}$  ( $2a = 10 \mu\text{m}$ ) [ $2a = 5 \mu\text{m}$ ] and the circles mark data points that are calculated using the Skorobogatiy *et. al.* material dispersion [83].

between 4 and 12  $\mu\text{m}$ . The  $2a = 5 \mu\text{m}$  fiber also shows a ZDW strongly increasing with NA in Fig. 5.4(a). Above NA = 0.3 the  $2a = 20 \mu\text{m}$  SIF has low loss, the ZDW decreases for increasing NA, and  $D_{4.5}$  changes only slightly. At NA = 0.7 the  $2a = 10 \mu\text{m}$  SIF has a ZDW comparable to the  $2a = 20 \mu\text{m}$  fiber and lower absolute value of the dispersion at the pump wavelength  $D_{4.5}$ . A small core size will also give a larger nonlinearity thus making the  $2a = 10 \mu\text{m}$  and NA = 0.7 the optimal candidate, among the investigated, for SCG, and such a fiber should be manufacturable [86].

All in all it is concluded from Fig. 5.4 that a SIF with  $2a = 10 \mu\text{m}$  and NA = 0.7 is the best choice for SCG to 12  $\mu\text{m}$ . However, to consider a fiber with a less extreme value of NA, and better power handling properties, the primarily considered fiber for SCG is a  $2a = 20 \mu\text{m}$  SIF. The  $2a = 20 \mu\text{m}$ , NA = 0.5, fiber has a ZDW calculated to be 6.74  $\mu\text{m}$ , while the ZDW of the  $2a = 10 \mu\text{m}$  fiber is 6.85  $\mu\text{m}$  when using Sellmeier data by Skorobogatiy *et. al.*

The chosen fibers are also considered using the Sellmeier data by Seddon *et. al.* [86]. The dispersion curves using this data for the material refractive index are shown in Fig. 5.5(a) for the  $2a = 10 \mu\text{m}$  fiber and in Fig. 5.5(b) for  $2a = 20 \mu\text{m}$ . Most noticeable is that  $2a = 20 \mu\text{m}$ , NA = 0.7 is the only parameter configuration yielding anomalous dispersion (be-

tween 8.2 and 13.7  $\mu\text{m}$ ) and that the  $2a = 20 \mu\text{m}$ ,  $\text{NA} = 0.5$  fiber shows all normal dispersion. The  $2a = 10 \mu\text{m}$  fiber shows all-normal dispersion for any of the investigated values of NA. The calculated confinement loss found using the Sellmeier polynomial by Seddon *et. al.* is nearly indistinguishable from the corresponding loss curves shown in Fig. 5.3(b)-left and -right, and therefore not shown.

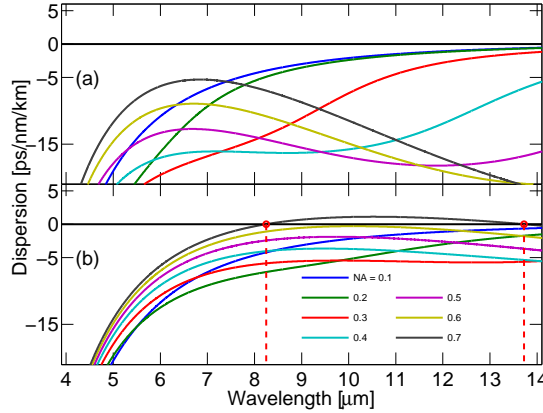


**Figure 5.5:** Dispersion curves for the (a)  $2a = 10 \mu\text{m}$  and (b)  $2a = 20 \mu\text{m}$  chalcogenide SIF for different values of the NA using the Sellmeier provided by Seddon *et. al.* [86]. Notice: One fiber (the  $2a = 20 \mu\text{m}$ ,  $\text{NA} = 0.7$  fiber) shows anomalous dispersion between 8.2 and 13.7  $\mu\text{m}$ .

## 5.2 Parameters for Modelling Supercontinuum Generation in Chalcogenide

To enable the prediction of the bandwidth of SCG in chalcogenide, the generalized nonlinear Schrödinger equation (GNLSE) is solved for the pseudo electric field envelope  $\tilde{C} = \tilde{C}(z, \omega)$  and an initial condition given by Eq. (2.3.10), as described in chapter 2. The quasi continuous wave (CW) ns-pulses expected from the Pr doped fiber laser, though, are so long that the calculation domain cannot be made large enough to encompass the pulse both in time and in frequency, when the expected broadening of the generated SC is so large. Thus, instead, pulse widths are taken to be  $T_{\text{FWHM}}$  of 10, 20 and 40 ps in order to illustrate a trend for the SC generated by increasingly broad and energetic pulses. The input pulse has a

central carrier wavelength  $\lambda_p = 4.5 \mu\text{m}$ , and the nonlinear refractive index of chalcogenide is taken to be  $n_2 = 2.4 \cdot 10^{-17} \text{ m}^2/\text{W}$  [10]. Light propagation in chalcogenide is influenced by two-photon absorption (TPA) that cause a nonlinear loss of energy. Generally the effect of TPA is modelled by including an imaginary part to the nonlinear coefficient  $\gamma$  from (2.3.7), and the energy loss it causes can influence the nonlinear dynamics, e.g., decreasing a soliton redshift [92, 93]. TPA is significant in the wavelength region around  $1.5 \mu\text{m}$ , and since pumping at  $4.5 \mu\text{m}$  in the following, TPA is not included when solving the GNLSE. The delayed Raman response is given on the form, previously encountered

$$\tilde{R}(\Omega) = (1 - f_R) + f_R \tilde{h}_R(\Omega) \quad \text{with} \quad \tilde{h}_R(\Omega) = \frac{\tau_1^2 + \tau_2^2}{\tau_2^2 - \tau_1^2(i + \tau_2\Omega)^2} \quad (5.2.1)$$

where  $f_R = 0.115$  is the fractional delayed Raman contribution, and  $\tilde{h}_R(\Omega)$  is the delayed Raman response function with time constants  $\tau_1 = 23.1 \text{ fs}$  and  $\tau_2 = 195 \text{ fs}$  [83]. With the given time constants, the delayed Raman response gain spectrum consists of a single peak at a Stokes shift of  $6.9 \text{ THz}$ . Fig. 5.6 shows  $f_R \text{Im}(\tilde{h}_R)$  for chalcogenide, for fused silica and

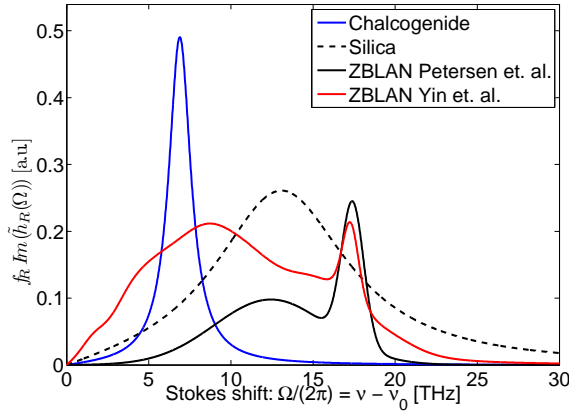


**Figure 5.6:** Comparable delayed Raman response  $f_R \text{Im}(\tilde{h}_R)$  as function of Stokes shift. The delayed Raman gain shows a single gain peak at  $6.89 \text{ THz}$  [83]. Also plotted for comparison are the Raman responses for silica [6] and for ZBLAN (see chapter 3).

for the two measurements of the Raman response in ZBLAN presented



in chapter 3 for comparison. The first two anti-Stokes- and four Stokes-shifted orders of a Raman cascade corresponding to a pump wavelength  $\lambda_p = 4.5 \mu\text{m}$  are listed in Table 5.2.

$\lambda_{aS}^{R_2}$	$\lambda_{aS}^{R_1}$	$\lambda_p$	$\lambda_S^{R_1}$	$\lambda_S^{R_2}$	$\lambda_S^{R_3}$	$\lambda_S^{R_4}$
$\mu\text{m}$	$\mu\text{m}$	$\mu\text{m}$	$\mu\text{m}$	$\mu\text{m}$	$\mu\text{m}$	$\mu\text{m}$
3.73	4.08	4.5	5.02	5.68	6.53	7.68

**Table 5.2:** The location of the first two Raman anti-Stokes and four Stokes lines when pumping at  $\lambda_p = 4.5 \mu\text{m}$ .

### 5.2.1 Time- and Frequency Grid and Extreme Broadening

The ps-pulses that are investigated during simulations on SCG in the chalcogenide SIFs, are initially narrow band. The spectral bandwidth of the initial condition decreases correspondingly as its temporal width is increased, when going through  $T_{\text{FWHM}}$  of 10, 20 and 40 ps. This is due to the constant time- bandwidth product of a Fourier transform (FT) limited pulse, and for all values of  $T_{\text{FWHM}}$ , a sufficient frequency resolution at the onset of propagation must be ensured, while also having a calculation domain with the proper bandwidth after the extreme spectral broadening has occurred during propagation. This imposes requirements on the number of grid points on the time- and frequency axes. If one expects  $b$  points within the input energy spectral density (ESD)  $|\tilde{A}(\omega)|^2$  frequency full-width-at-half-maximum (FWHM)  $\omega_{\text{FWHM}}$ , it means that one needs a frequency spacing of  $\Delta\omega = \omega_{\text{FWHM}}/b$ . The bandwidth of the generated SC is

$$\omega_B = 2\pi c \left( \frac{1}{\lambda_{\min}} - \frac{1}{\lambda_{\max}} \right) \quad (5.2.2)$$

where  $\lambda_{\min}$  ( $\lambda_{\max}$ ) is the minimum (maximum) wavelength edge of the SC after propagation. The number of points needed on the grids then, is

$$N_p = \frac{\omega_B}{\Delta\omega} = \frac{2\pi cb(\lambda_{\min}^{-1} - \lambda_{\max}^{-1})}{\omega_{\text{FWHM}}}. \quad (5.2.3)$$

For the Gaussian shaped input pulse used here, it can be shown from FT theory (see appendix C page 107), that the corresponding frequency width

of the ESD, is given by  $\omega_{\text{FWHM}} = 4 \ln 2 / T_{\text{FWHM}}$ . Thus, the number of grid points needed becomes

$$N_p = \frac{b\pi c(\lambda_{\min}^{-1} - \lambda_{\max}^{-1})T_{\text{FWHM}}}{2 \ln 2}. \quad (5.2.4)$$

To be certain that the effect of four-wave mixing (FWM) is included (see section 5.3) in the calculation, and to eliminate edge effects due to implicit periodic boundary conditions of the discrete Fourier transforms (DFTs), that can lead to numerical artifacts, the calculation domain is taken to stretch from  $\lambda_{\min} = 1.2 \mu\text{m}$  and to  $\lambda_{\max} = 18 \mu\text{m}$ . The largest number of grid points, that are tolerable is  $N_p = 2^{18}$  points, or computation time will be enormous, and for  $T_{\text{FWHM}} = 40 \text{ ps}$  one will thus have

$$b = \frac{2N_p \ln 2}{\pi c(\lambda_{\min}^{-1} - \lambda_{\max}^{-1})T_{\text{FWHM}}} \approx 12.4. \quad (5.2.5)$$

Ideally one should require a large value of  $b$ , but it is found that the value above, which represents worst case, give trustworthy results that are presented in section 5.3. The value of  $b$  is calculated for the different simulations performed and summarized in table 5.3. Even though the

$T_{\text{FWHM}}$	10 ps	20 ps	40 ps
$b$	49.6	24.8	12.4

**Table 5.3:** Number of grid points per ESD frequency FWHM,  $b$  for each value of  $T_{\text{FWHM}}$  investigated.

computational load is also significant using  $N_p = 2^{18}$  grid points (the computation time for the most dynamical simulation with the most energetic pulse has been between three and four weeks), this amount is used in all simulations to have exact comparable calculation domains. With the specified limits in the frequency domain and  $N_p = 2^{18}$ , the time domain width becomes 1.12 ns, with a grid spacing of  $dt \approx 4.3 \text{ fs}$ .

## 5.3 Results of Simulations

In all simulations the peak power is fixed at  $P_0 = 1 \text{ kW}$  and the pump wavelength is fixed at  $\lambda_p = 4.5 \mu\text{m}$  to model the Pr doped fiber laser. All spectra presented in the following are ensemble averages over 30 shots

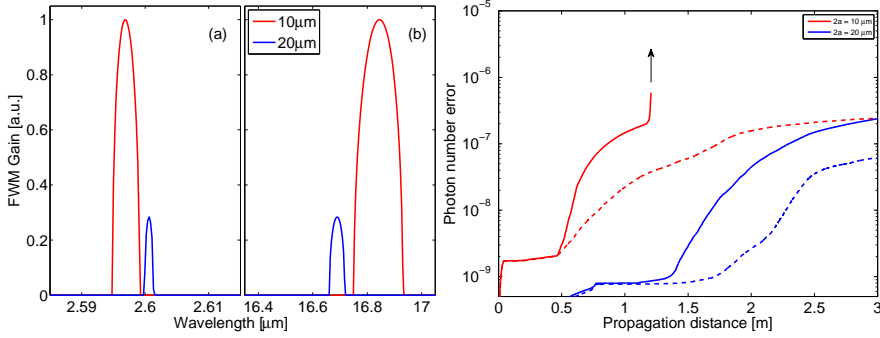


**Figure 5.7:** Left: Location of FWM gain band as function of wavelength for  $P_0 = 1 \text{ kW}$  and  $\lambda_p = 4.5 \mu\text{m}$  for the fibers considered. (a) Anti-Stokes and (b) Stokes gain band. Right: The photon number error as function of propagation distance for  $T_{\text{FWHM}} = 40 \text{ ps}$  and neglecting loss and noise. Solid (dashed) line is for simulation using Sellmeier data by Skorobogatiy *et al.* [83] (Seddon *et al.* [86]).

as described in chapter 2. The plots shown in Fig. 5.7-left reveal FWM gain (see Eq. (2.4.6)) at (a) anti-Stokes wavelengths around  $2.6 \mu\text{m}$  and (b) at Stokes wavelengths around  $16.7 \mu\text{m}$  for both the  $2a = 10 \mu\text{m}$  and the  $2a = 20 \mu\text{m}$  fiber. Notice that the gain bands are asymmetric, when plotted on a wavelength axis. Notice also that the peak gain is  $g_{\text{max}} = \gamma P_0$  and thus, the gain is largest for the  $2a = 10 \mu\text{m}$ , because a smaller effective area leads to a larger  $\gamma$ . Simulations made using the

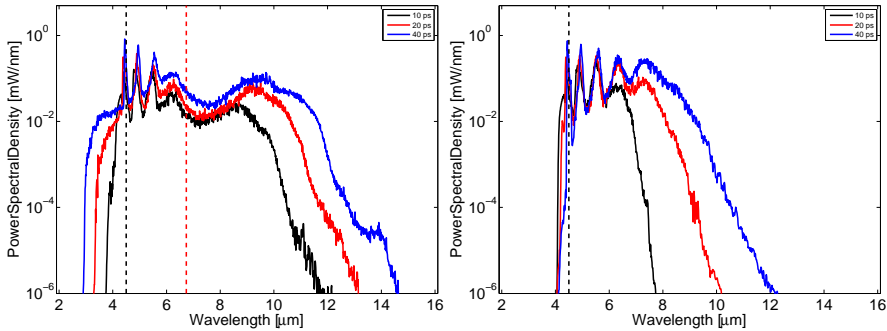


**Figure 5.8:** Left: SCG in the  $2a = 20 \mu\text{m}$ , NA = 0.5 SIF after  $L = 3 \text{ m}$  of propagation for different values of  $T_{\text{FWHM}}$  and Sellmeier data from [83]. Right: SCG in the  $2a = 20 \mu\text{m}$ , NA = 0.5 SIF and Sellmeier data from [86]. Dashed black (red) line marks  $\lambda_p$  (ZDW).

Sellmeier data provided by Seddon *et. al.* [86] show no sign of FWM. To include the effects of FWM, in the simulation based on Sellmeier data from Skorobogatiy *et. al.*, the calculation domain must be chosen to stretch below  $2.59 \mu\text{m}$  and above  $17 \mu\text{m}$ . As mentioned above though, all simulations use  $\lambda_{\min} = 1.2 \mu\text{m}$  and  $\lambda_{\max} = 18 \mu\text{m}$  to avoid edge effects from the periodic boundary conditions of the DFT,  $N_t = 2^{18}$  points on the time/frequency grid, and a goal error of  $\delta_g = 10^{-8}$ . To check the conservation of the photon number, the photon number error (see Eq. 2.3.11), is plotted in Fig. 5.7-right for all fibers in the case of  $T_{\text{FWHM}} = 40 \text{ ps}$  and neglecting loss and noise.

### 5.3.1 The Larger Core Fiber

The results of SC spectral development after  $L = 3 \text{ m}$  of propagation in the  $2a = 20 \mu\text{m}$ ,  $\text{NA} = 0.5$  SIF are shown in Fig. 5.8-left and -right using the Sellmeier data from [83] and [86], respectively. The widest spectrum found for the  $2a = 20 \mu\text{m}$  fiber corresponds to a pulse of width  $T_{\text{FWHM}} = 40 \text{ ps}$ , incident on the fiber with properties calculated using dispersion data from Skorobogatiy *et. al.* [83]. All the found bandwidths are measured numerically as the 30 dB drop from the ESD maximum value, and summarized in Table 5.4. The widest spectrum found for this fiber spans a wavelength region from  $3.1$  to  $12.8 \mu\text{m}$ , and thus two octaves in the IR.

Generally, the spectral development starts from the onset of propagation by slight broadening caused by self-phase modulation (SPM) followed by a very pronounced forming of a cascade of Raman Stokes and anti-Stokes waves [87,88]. The development of the Raman cascade is displayed in Fig. 5.9-left where green vertical lines mark the locations of anti-Stokes and Stokes lines (see Table 5.2). A very good correspondence between predicted values and cascade-peaks is observed. After the initial broadening of the spectrum due to the delayed Raman effect, which continues to dominate until  $L \sim 1 \text{ m}$ , and the fourth order Raman line has crossed the ZDW, soliton related dynamics begin to dominate. Light has shifted across the ZDW, and numerous nonlinear effects cause further spectral broadening. Spectrograms showing how the spectral development continues after the Raman cascade is created is shown in Fig. 5.9-right. After light has shifted into the anomalous dispersion regime individual solitons start to redshift due to the soliton self-frequency shift (SSFS) and after  $3 \text{ m}$  of propagation a wide SC is formed. A Raman cascade, similar to the one described here, has been experimentally observed in fused silica in

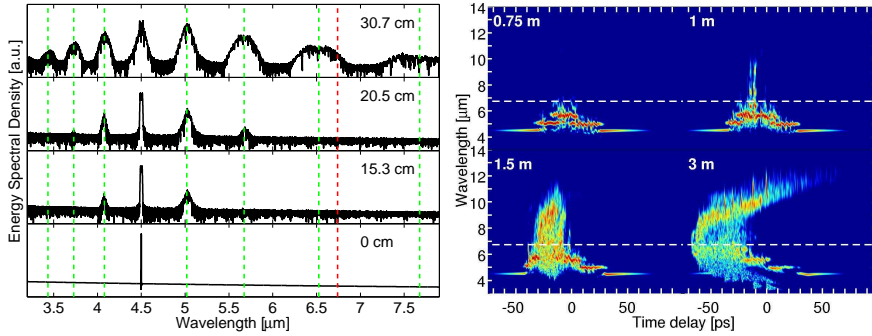


**Figure 5.9:** Left: Spectral development in the first approximately 30 cm of the  $2a = 20 \mu\text{m}$  SIF with an input pulse width of  $T_{\text{FWHM}} = 40 \text{ ps}$ . Green vertical lines mark the higher order Stokes and anti-Stokes Raman lines from Table 5.2, and red is the fiber ZDW. Right: Spectrograms showing the spectral development during propagation in the  $2a = 20 \mu\text{m}$  fiber. White dashed line marks ZDW.

1978 [16] where a  $Q$ -switched ns Nd:YAG laser at  $1.064 \mu\text{m}$  with  $\sim 50 \text{ kW}$  peak power coupled into a  $33 \mu\text{m}$  core Ge-doped silica fiber generated at least three Stokes shifted Raman lines. Similarly three Raman orders were observed from a  $1553 \text{ nm}$  laser, pumping ns pulses with  $\sim 2 \text{ kW}$  of peak power, into small core ( $< 6.5 \mu\text{m}$ ) chalcogenide fibers [87] and a large core chalcogenide fiber ( $2a = 65 \mu\text{m}$ ) pumped with ns pulses at  $1.9 \mu\text{m}$  generate four Stokes orders in [88]. Furthermore, a spectral development similar to the one observed, starting with the strong Raman cascade has been reported in [87, 94].

### 5.3.2 The Smaller Core Fiber

The results of SC spectral development in the  $2a = 10 \mu\text{m}$ ,  $\text{NA} = 0.7$  SIF are shown in Fig. 5.10-left and -right using the Sellmeier data from [83] and [86] respectively. For this fiber, the broadening is so violent and the nonlinearity so strong that the calculation domain can only house propagation until  $L \approx 0.75 \text{ m}$  for the simulation based on the Sellmeier data by Skorobogatiy *et. al.* This is manifested in Fig. 5.7-right where a sudden increase in photon number around  $L = 1.2 \text{ m}$  signifies a breakdown of trustworthy result. The increase in photon number is preceded by breakthrough of energy at the spectral boundaries of the calculation domain due to the periodic boundary conditions of the DFT, and for this reason, SC is not propagated further than  $L = 0.75 \text{ m}$  in the small core

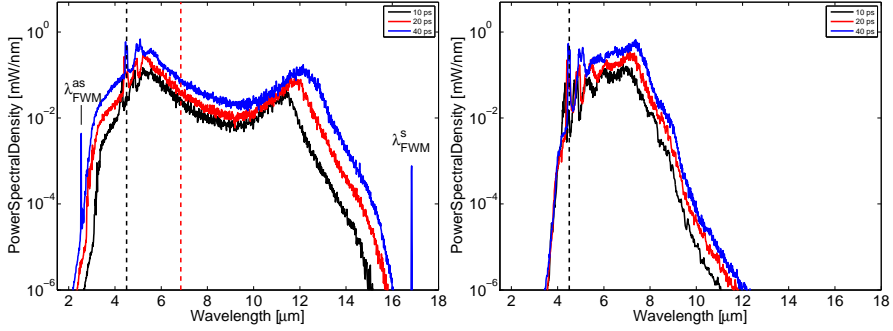


**Figure 5.10:** Left: SCG in the  $2a = 10 \mu\text{m}$ ,  $\text{NA} = 0.7$  SIF after  $L = 0.75 \text{ m}$  of propagation for different values of  $T_{\text{FWHM}}$  and Sellmeier data by [83]. Right: SCG in the  $2a = 10 \mu\text{m}$ ,  $\text{NA} = 0.7$  SIF and Sellmeier data by [86]. Dashed black (red) line marks  $\lambda_p$  (ZDW).

fiber. The mechanism behind the spectral broadening is the same as for the large core fiber, however it develops over a shorter length of fiber and extremely broad SC is demonstrated already after  $L = 0.75 \text{ m}$ . Notice the narrow FWM peaks marked in Fig. 5.10-left. The broadest spectrum for this simulation is stretching between  $3.0$  and  $15.3 \mu\text{m}$  is demonstrated for the pulse width of  $T_{\text{FWHM}} = 40 \text{ ps}$ .

### 5.3.3 Bandwidths and Fiber Length

The large nonlinearity of chalcogenide enables broad SCG in spite of pumping deeply in the normal dispersion regime of the SIFs, and in spite of using a rather modest peak power of  $1 \text{ kW}$ . The development of the band edges predicted by the calculations are shown in Fig. 5.11-left and -right for single shot simulations using  $T_{\text{FWHM}} = 40 \text{ ps}$  and the  $20 \mu\text{m}$  and the  $10 \mu\text{m}$  fiber respectively. In the ps-pumped regime, demonstrated here, the initial broadening mechanisms are SPM, as was also the case in chapter 3, but now accompanied by strong Raman amplification that forms the prominent Raman cascade observed in Fig. 5.9-left. These mechanisms do evidently not broaden the spectrum over distances as short as when compared to the fs-pumped soliton fissions witnessed in chapter 3 and longer fiber lengths are needed. The band edges of the generated SC, however, do show a tendency to saturate, and this is particularly clear for the solid blue and red curves in Fig. 5.11-right. The saturation means that SC is almost fully developed after  $30 \text{ cm}$  for the

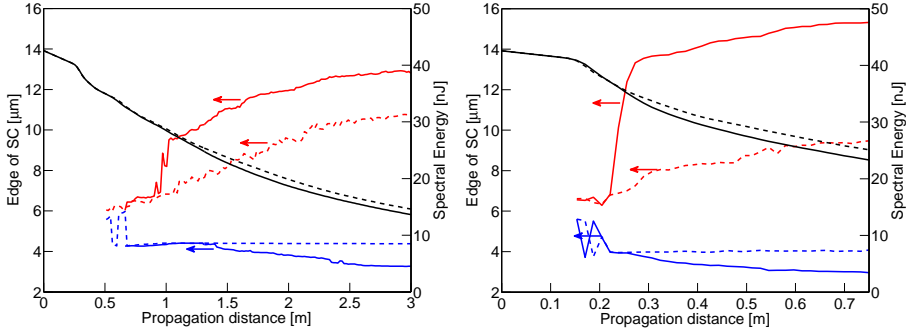


**Figure 5.11:** Black curves show the energy in a single-shot spectrum as function of propagation distance, while red (blue) curve is the long (short) wavelength edge of the generated SC using  $T_{\text{FWHM}} = 40$  ps. Solid (dashed) line is for Sellmeier data from [83] ([86]). Left panel is for the  $2a = 20$   $\mu\text{m}$  fiber, while right panel is the  $2a = 10$   $\mu\text{m}$  fiber.

10  $\mu\text{m}$  fiber, while the fiber length of 3 m of the 20  $\mu\text{m}$  is appropriate, though 2.5 m of propagation might possibly have sufficed (Fig. 5.11-left). Finding the optimal fiber length is important in regards to attenuation in a realized experiment, especially since simulations here employ a modest and frequency constant material loss, that do not included discrete absorption bands, and when considering there are different reports of

$T_{\text{FWHM}}$ [ps]	$\lambda_{\text{min}}$ [ $\mu\text{m}$ ]	$\lambda_{\text{max}}$ [ $\mu\text{m}$ ]	$T_{\text{FWHM}}$ [ps]	$\lambda_{\text{min}}$ [ $\mu\text{m}$ ]	$\lambda_{\text{max}}$ [ $\mu\text{m}$ ]
a: (Spectra in Fig. 5.8-left).			b: (Spectra in Fig. 5.8-right).		
10	3.9	10.7	10	4.1	7.4
20	3.5	11.9	20	4.2	9.1
40	3.1	12.8	40	4.4	10.4
c: (Spectra in Fig. 5.10-left).			d: (Spectra in Fig. 5.10-right).		
10	3.2	14.3	10	4.0	9.4
20	3.1	14.8	20	4.1	9.4
40	3.0	15.2	40	4.1	9.5

**Table 5.4:** Band edges of the simulated SC for the  $2a = 20$   $\mu\text{m}$  SIF, a: (b:) using Sellmeier data from [83] ([86]). Bandwidths of the simulated SC for the  $2a = 10$   $\mu\text{m}$  SIF, c: (d:) using Sellmeier data from [83] ([86]).

when the long wavelength material absorption edge becomes significant in chalcogenide. The curves showing the band edges of the SC fluctuates for small propagation distances, both in 5.11-left and -right, because a specific 30 dB band edge is not well defined at the early stage of SC development, when the Raman cascaded has not yet merged to a full SC.

The spectra calculated using material dispersion properties provided by Seddon *et. al.* [86] show significantly less broadening than spectra based on Sellmeier data from Skorobogatiy *et. al.* This is attributed to the complete absence of anomalous dispersion regime, and corresponding soliton dynamics. The full developed band edges calculated in all simulations are summarized in Table 5.4.

## 5.4 Summery of Chapter 5

In this chapter was considered the possibility of creating a broad band SC in chalcogenide ( $\text{As}_2\text{Se}_3$ ) fibers stretching beyond the  $\sim 4.5 \mu\text{m}$  limit achieved by ZBLAN based SC. Two laser sources, that are emerging technologies, one at  $2.9 \mu\text{m}$  and one at  $4.5 \mu\text{m}$  respectively, have been proposed for this purpose [12]. Suitable fiber designs have been suggested, and particularly, chalcogenide PCFs are candidates for pumping at  $2.9 \mu\text{m}$ , while SIFs are possible candidates for pumping at  $4.5 \mu\text{m}$ . Two particular SIFs are subject to further investigations, and numerical simulation of SCG show that these fibers are both very promising candidates for broadband IR SC in the range from  $4 \mu\text{m}$  to above  $12 \mu\text{m}$ .

The results of this chapter are supported by calculations only, and a rather modest material loss have been employed. It must be expected however that the long wavelength absorption edge in a realised fiber will ultimately determine the long wavelength edge of generated SC. Calculations show a very large broadening of the incident light pulses over propagation distances in the order of 1 m, and in this sense, a loss larger than modelled here, will impact the generated SC but will not be ruining to it, since fiber lengths can be kept short. In any case, the results of this chapter should be considered a tentative estimate of the achievable width of SCG in chalcogenide fibers.

To improve the numerical model, more accurate data is needed regarding the loss and the dispersion of chalcogenide. In particularly, a cut-back measurement of the loss from a drawn fiber could be useful, and perhaps dispersion measurement, e.g., by the frequency resolved optical gating (FROG) method, mentioned in chapter 3 could also be beneficial.





## Chapter 6

# Conclusion

During the course of this Ph.D.-project three different soft-glasses have been investigated, primarily by numerical simulations, for use in generating a wide band mid-infrared (IR) supercontinuum (SC). Firstly, the fluor based ZBLAN material was investigated thoroughly both using numerical simulations and measurements. Then tellurite was briefly considered, but material loss proved high in preform samples drawn into photonic crystal fibers (PCFs) at Technical University of Denmark (DTU), and this material was not pursued very far. The last material was chalcogenide that show great potential for supercontinuum generation (SCG) in the mid-IR.

The linear properties of ZBLAN demonstrate a bulk zero dispersion wavelength (ZDW) that cause conventional seed laser sources, based on Yb/Er doped fibers, to be less suited as pump sources than the more recently emerging Tm technology. It is demonstrated that an adequately energetic pulsed laser source pumping in the normal dispersion regime of a ZBLAN step-index fiber (SIF) will enable the generation of SC, but also that it is preferable to use a source pumping directly in the anomalous dispersion regime, to achieve a broader spectrum. During the review of ZBLAN the linear properties have been thoroughly discussed, and a measurement of the fiber dispersion and a measurement of the delayed Raman gain profile was presented. The Raman measurement was compared to existing partial measurements, and another full measurement, and based on simulations of fs-pumped SCG, it is concluded that the Raman response by Petersen *et al.* of Aarhus University (AU) show good correspondence with measurements, and gives an appropriate description of ZBLAN. The correspondence between measurements and simulations

lead to a short discussion of what fibers are suitable as suggestions for a SC source, and a prototype mid-IR SC laser has been manufactured by an industrial collaborator showing spectra with SC spanning the region between  $1.5\ \mu\text{m}$  and  $4.3\ \mu\text{m}$ .

To extend the long wavelength edge of SCG further, it has been investigated numerically if it is possibility to make a SC, stretching beyond  $12\ \mu\text{m}$ , by simulating a praseodymium (Pr) doped fiber laser pumping a highly nonlinear chalcogenide SIF. The results are very promising, though it should be kept in mind that they are solely based on numerical predictions and should be considered an optimistic estimate for the width of a possible mid-IR SC in chalcogenide. The long wavelength edge of a SC developing in a chalcogenide fiber, will eventually be determined by the long wavelength absorption edge in a realised fiber.

## 6.1 Future Perspectives in Mid-infrared Supercontinuum Generation

Further numerical studies and modelling of SCG in ZBLAN could potentially improve a second version of a mid-IR SC source. Particularly, more specific numerical investigations could be performed in regards to the spectral flatness and specific coherence properties of the SC, which has not been investigated here. In this respect, further measurements of the Raman response could be performed in order to give a final conclusion about the magnitude of the delayed Raman gain in ZBLAN. In addition to this, cut-back measurements of the loss in ZBLAN fibers could be made in the entire wavelength range practical for SCG, and further dispersion measurements could be performed, e.g., by the frequency resolved optical gating (FROG) measurement method proposed. The ZBLAN fiber drawing technology is characterized by less maturity when comparing to silica based fiber technology, and fibers obtained from manufacturers can show great deviations from batch to batch, and even from piece to piece on a fiber spool. In time, better characterization will be possible when fiber drawing technology improves.

During the Ph.D.-project the nonlinear soliton matching (NLSM) scheme was introduced. This scheme should be considered when designing a system of concatenated passive optical fibers for extended benefit of nonlinear effects in a system of multiple different nonlinear fibers. It was shown that matching the nonlinear properties of fibers takes precedence over linear properties, and in future work, a practical demonstration of

the scheme could be interesting. Particularly, it could prove exciting to use the NLSM-scheme to predict the development of a full SC coupled from a ZBLAN fiber, where it is initially created into a uniform or tapered chalcogenide SIF for further redshift into the IR. Doing so could prove a viable approach to obtaining a broad SC in the IR without designing an entirely new seed laser for pumping chalcogenide directly.

Pumping chalcogenide directly however, does show a promising future in mid-IR SCG, and it could be very interesting to witness the measurement of a realised SC spectrum in a chalcogenide SIF pumped by a novel  $4.5\text{ }\mu\text{m}$  Pr doped seed laser. Similarly, the investigations of  $2.9\text{ }\mu\text{m}$  pumped SCG in chalcogenide PCFs could be extended further to elaborate on the potential of such a setup, and also measurements could be very interesting as future research.

In regards to the numerical work done during this project, the results are largely built upon brute force calculations and vast amounts of computer power. It could be very beneficial for continued work, using different soft-glasses, to study and quantify the role of the local goal error,  $\delta_g$ , when changing between materials that have nonlinear properties that vary significantly, thereby determining what is an appropriate selection criterion that ensures reliable results while not draining computational resources. Similarly, it could also be investigated what significance the calculation domain width, and the number of samples per energy spectral density (ESD) full-width-at-half-maximum (FWHM), as discussed in chapter 5, has on results. During these studies, it has been observed that numerical artifacts sometimes find their way into calculated spectra if appropriate care is not taken to use a calculation domain that is wide enough or use an adequately large number of grid points. Instead of using brute force, as done here, to overcome these observed artifacts, it could be assessed whether they influence results significantly. Typically, the accumulated energy in spectral components that are ascribed as numerical artifacts can be many orders of magnitude lower than the energy of the entire signal, and perhaps they do not influence results in a significant way, so lower numerical tolerances are acceptable, but this needs further investigations.



## Appendix A

# The Generalized Nonlinear Schrödinger Equation in the Interaction Picture

In this appendix, conversion from the generalized nonlinear Schrödinger equation (GNLSE) for the complex electric field envelope  $A(z, T)$ , defined so that  $P(t) = |A(t)|^2$  is the instantaneous power [6, 23], via the frequency domain GNLSE for the pseudo electric field envelope  $\tilde{C}(z, \omega)$  and to the frequency domain interaction picture (IAP) GNLSE introduced by J. Hult [30], is reviewed in detail. The introduction of the IAP version of the GNLSE is significant because it represents a tiny paradigm shift in the way the GNLSE is simulated by Ole Bang's group at DTU. The method used in the Ph.D.-thesis by M. H. Frosz [23] and the method proposed in [6] to solve the GNLSE, both build on the split-step Fourier method (SSFM), while recent results both in this thesis and in [78, 95] transform the GNLSE to the IAP before solving it. Using the SSFM, the linear and nonlinear parts of the GNLSE are separated and individually propagated incrementally, whereas when solving the GNLSE in the IAP, both the linear and nonlinear part are propagated together in a single step.

## A.1 The GNLSE

The GNLSE for the time domain complex electric field envelope  $A(z, T)$  is [14]

$$\frac{\partial A}{\partial z} + \frac{\alpha}{2} A - \sum_{k \geq 2} \frac{i^{k+1}}{k!} \beta_k \frac{\partial^k A}{\partial T^k} = i\gamma \left( 1 + i\tau_{\text{shock}} \frac{\partial}{\partial T} \right) \left( A \int R(T') |A(T - T')|^2 dT' \right) \quad (\text{A.1.1})$$

where  $\alpha = \alpha(\omega)$  is the power attenuation,  $\beta_k = d_{\omega}^k \beta$  is the  $k$ 'th derivative of the propagation constant with respect to frequency  $\omega$ , and  $T = t - z/v_g$  is a retarded time frame moving with the group velocity  $v_g = 1/\beta_1(\omega_p)$  at the pump frequency  $\omega_p$  (see appendix E page 123). The nonlinear coefficient is

$$\gamma = \frac{n_2 \omega_0}{c A_{\text{eff}}(\omega_0)} \quad (\text{A.1.2})$$

where  $n_2$  is the nonlinear refractive index of the fiber material,  $c$  is the speed of light in vacuum, and  $A_{\text{eff}}(\omega_0)$  is the effective area of the mode at the expansion frequency  $\omega_0$ . The term with  $\partial/(\tau_{\text{shock}} \partial T)$  accounts for the optical shock effect with shock time  $\tau_{\text{shock}}$  which is often taken to be  $1/\omega_0$ . Finally  $R(T)$  is the material response function.

It has been argued, e.g., in [17] that Eq. (A.1.1) does not account accurately for modal dispersion in cases of strong wavelength dependence of the effective area. Such strong modal dispersion is particularly prominent in photonic bandgap (PBG) fibers around the band edges [17], but also when considering extremely broadband supercontinuum generation (SCG), the effective area variation can be large across a spectrum. This variation should be included in the GNLSE, but is ignored in Eq. (A.1.1). The considerations in [17] lead to a frequency domain equation for a pseudo electric field envelope  $\tilde{C}(z, \omega)$  and this equation has been used extensively during this Ph.D.-work. The GNLSE is then [31]

$$\begin{aligned} \frac{\partial \tilde{C}}{\partial z} - i \{ \beta(\omega) - [\beta(\omega_0) + \beta_1(\omega_p)(\omega - \omega_0)] \} \tilde{C} + \frac{\alpha(\omega)}{2} \tilde{C} \\ = i\bar{\gamma}(\omega) \left[ 1 + \frac{\omega - \omega_0}{\omega_0} \right] \mathcal{F} \left\{ C \int_{-\infty}^{\infty} R(T') |C(T - T')|^2 dT' \right\} \end{aligned} \quad (\text{A.1.3})$$

where  $\tilde{C} = \tilde{C}(\omega, z)$  is the Fourier transform (FT) of the pseudo field envelope  $C = C(z, T)$ . The nonlinear coefficient changes slightly from the definition in Eq. (A.1.2) and becomes frequency dependent

$$\bar{\gamma}(\omega) = \frac{n_2 n_0 \omega_0}{c n_{\text{eff}}(\omega) \sqrt{A_{\text{eff}}(\omega) A_{\text{eff}}(\omega_0)}}. \quad (\text{A.1.4})$$

Here  $n_0 = n_{\text{eff}}(\omega_0)$  is the effective refractive index of the mode  $n_{\text{eff}}(\omega)$  at the expansion frequency. Finally, the transformation between the FT of the pseudo electric field envelope  $\tilde{C}$  and the FT of the electric field envelope  $\tilde{A}$  is

$$\tilde{C}(z, \omega) = \left[ \frac{A_{\text{eff}}(\omega)}{A_{\text{eff}}(\omega_0)} \right]^{-\frac{1}{4}} \tilde{A}(z, \omega). \quad (\text{A.1.5})$$

Notice that if the frequency variation of the effective area and effective index is ignored so that  $A_{\text{eff}}(\omega) = A_{\text{eff}}(\omega_0)$  and  $n_{\text{eff}}(\omega) = n_0$  then

$$\tilde{C} = \tilde{A} \quad \text{and} \quad \bar{\gamma}(\omega) = \frac{n_2 \omega_0}{c A_{\text{eff}}(\omega_0)} = \gamma. \quad (\text{A.1.6})$$

## A.2 Transforming into the IAP

Equation (A.1.3) is a 1st order partial differential equation that can be written in terms of two operators, where one operator is linear while the other one is nonlinear. To see how Eq. (A.1.3) is transformed into the IAP, we start by writing it explicitly as the sum of operators

$$\frac{\partial \tilde{C}}{\partial z} = \left( \tilde{L}(\omega) + \tilde{N}(\omega) \right) \tilde{C}. \quad (\text{A.2.1})$$

The linear operator  $\tilde{L}$  is defined in Eq. (2.3.8) and  $\tilde{N}$  is a nonlinear operator representing the entire right-hand side (RHS) of Eq. (A.1.3). Now defining the transformation

$$\tilde{C}_I = e^{-z\tilde{L}} \tilde{C} \quad (\text{A.2.2})$$

inserting it into the left-hand side (LHS) above, and differentiating, one gets

$$\frac{\partial \tilde{C}}{\partial z} = \frac{\partial}{\partial z} \left( \tilde{C}_I e^{z\tilde{L}} \right) = e^{z\tilde{L}} \frac{\partial \tilde{C}_I}{\partial z} + \tilde{L} e^{z\tilde{L}} \tilde{C}_I. \quad (\text{A.2.3})$$



Inserting in the RHS of Eq. (A.2.1) then

$$e^{z\tilde{L}}\frac{\partial\tilde{C}_I}{\partial z} + \tilde{L}e^{z\tilde{L}}\tilde{C}_I = \tilde{L}e^{z\tilde{L}}\tilde{C}_I + \tilde{N}e^{z\tilde{L}}\tilde{C}_I \quad (\text{A.2.4})$$

and removing the equivalent terms, one gets

$$\frac{\partial\tilde{C}_I}{\partial z} = e^{-z\tilde{L}}\tilde{N}e^{z\tilde{L}}\tilde{C}_I = e^{-z\tilde{L}}\tilde{N}\tilde{C} \quad (\text{A.2.5})$$

so finally

$$\frac{\partial\tilde{C}_I}{\partial z} = i\bar{\gamma}(\omega)e^{-z\tilde{L}}\left[1 + \frac{\omega - \omega_0}{\omega_0}\right]\mathcal{F}\left\{C\mathcal{F}^{-1}\left\{\tilde{R}\mathcal{F}\{|C(T)|^2\}\right\}\right\}. \quad (\text{A.2.6})$$

The above equation is solved in a single step, e.g., by the `Matlab`-function `ode45()`, or another suitable numerical integration scheme. The one used in this work is a fourth order Runge-Kutta scheme that incorporates the local goal error method [35]. In appendix B, starting page 99, a code example is suggested that can solve Eq. (A.2.6) under very general conditions using the `ode45()` solver from `Matlab`.

## Appendix B

# Structuring a Matlab-code for Solving the Generalized Nonlinear Schrödinger Equation

In this appendix, I give a review of how a code for solving the generalized nonlinear Schrödinger equation (GNLSE) in the interaction picture (IAP) can be structured in a very versatile yet simple and comprehensive way. The appendix includes a code example, which is, to be quite clear, the boiled down essence of the practical experience I have gained in solving the GNLSE in this 3 years of Ph.D.-work. It must be stressed that structuring a code like in the example is very beneficial because it operates only on the most essentially needed input for solving the GNLSE. Each of these inputs are calculated in separate functions, and these functions are easily changed or substituted without any changes to the remaining code. This is very neat when investigating different fiber structures, fiber materials, pump systems or versions of the GNLSE. The code example is for `Matlab`, and relies heavily on the function concept here, but it is a good starting point for porting to an open-source language like `python`, or a more high-performance programming language, e.g., `Fortran` or `C++`, which could potentially reduce execution time.

The code example is a simplified version of the actual solver used throughout this work, and in particular, it does not include a random noise model to superimpose on the initial condition [31], nor does it deter-

mine the solution using an adaptive step size algorithm with a customized error control, e.g., like the local goal error method [35]. Instead, for simplicity, it uses a built-in function from `Matlab` (`ode45()`) for performing the numerical integration.

It is noted to the reader, that the code has produced the results shown in section B.2.2, but it requires properly defined auxiliary functions to work. To appreciate how these are defined and parsed to the solver, one must be familiar with the `struct`-type in `Matlab` (in object-oriented programming languages one can use classes). The `struct`-type is useful because an arbitrary amount of variables, function-handles or other `structs` can be stored in them, and parsed around among functions at will.

## B.1 Code for Solving the GNLSE (or NLSE)

```

1 function [t, omega, z, A]=Solve_a_NLSE(ForOps,ForInt)
2
3 global c_light
4 c_light=2.99792458*1e8; %% speed of light in vacuum.
5 s = struct();
6
7 %%%%%%%% parameters for input %%%%%%%%%
8 z=ForInt.z;
9 [Aini, s.t, s.Omega, s.w_0, s.w_p]=ForOps.EnvFunc(ForInt,
   ForOps.EnvParams);
10
11 [s.Aeff, s.Aeff_0, s.Aeff_p]=ForOps.AeffFunc(s,ForOps.
   AeffParams);
12 [s.neff, s.n0]=ForOps.nEffFunc(s,ForOps.nEffParams);
13 [s.L, s.beta2AtPump] = ForOps.LinOpFunc(s,ForOps.LinOpParams)
14 [ForOps.NLOpParams.R_Omega, s.fR]=ForOps.MatResFunc(s,ForOps.
   MatResParams);
15 ForOps.NLOpParams.gamma=ForOps.gammaFunc(s,ForOps.NLOpParams)
16 %%%%%%%%
17
18
19
20 %%%%%%%% Actual solution of problem %%%%%%%%%
21 C_tilde_IAP=gotoC_tilde_IAPfromA(Aini,z(1),s);
22 [~,C_tilde_IAP]=ode45(ForInt.WhatEqn,z,C_tilde_IAP,[],s,
   ForOps.NLOpParams);
23 %%%%%%%%
24
25
26
27 %%%%%%%% Return values %%%%%%%%%
28 A=gotoAfromC_tilde_IAP(C_tilde_IAP.',z,s);
29 t=fftshift(s.t);
30 omega=fftshift(s.Omega)+s.w_0;
31 %%%%%%%%
32 end

```

## B.2 Structure of Code

Line 1: The return values are the time axis **t**, the physical angular frequency axis **omega**, the propagations distances **z** and a corresponding array containing the electric field envelope **A** in the time domain. Notice the functions in line 23 and 30 that perform the conversion

back and forth between electric field envelope and pseudo electric field envelope. The electric field envelope could equally well have been returned in the frequency domain, but it will be redundant to return both. The Matlab-structs `ForOps` and `ForInt` are two `structs` where the first contains function handles and `structs` with parameters needed for execution of lines 10-17. The second `struct`, `ForInt`, contains information regarding the numerical integration, e.g., wanted propagation distances, number of points on time-/frequency grid, wavelength window, what equation to solve, etc.

Line 5: In this line is defined a simple holding container where parameters calculated in the scope of the solver are stored. From a speed/memory perspective, parsing `s` and all its content around among functions that need variables from the scope of the solver, is not very effective, because it leads to redundant parsings, and is perhaps not advisable. However, in the case considered here, it simplifies the code, because all auxiliary functions (lines 10 through 17) can be defined with a small number of input arguments.

Line 10: The `struct`, `ForOps`, contains a function `EnvFunc` that take two `structs` as input arguments, and returns the initial condition, `Aini` in the time domain, the time, `t`, and pseudo frequency, `Omega`, axes, the expansion frequency `w_0` and the pump frequency `w_p`. The function `EnvFunc` is stored in `ForOps` by issuing `ForOps.EnvFunc = @myEnvFunc`, and parsing `ForOps` to the solver. Here, `myEnvFunc.m` must be a valid Matlab-function. It may seem arbitrary that it is the envelope function that returns the time and frequency axes for the calculation, and that the axes are not returned and independent function. This is actually advisable though, because physically, the sample times, where the envelope is known, defines the time axis, that defines the frequency axis. Finally, it should be noticed, that the envelope must be returned with the proper chirp, so it is correctly positioned in the pseudo-frequency window (see appendix D page 119).

Strictly speaking, the pump frequency, which is returned by the envelope function, is insignificant in the eye of the solver, but generally, it is good measure, that the auxiliary functions (in lines 10-17) return significant variables to the scope of the solver, because they can be needed in calculations, e.g., if one wants the solver to de-

termine the soliton number at the onset of simulation, or find the group velocity dispersion at the pump frequency etc. etc.

Line 12-17: These lines execute functions, all stored in `ForOps` as illustrated above, that return, the effective area, the effective index, the linear operator, the full material response, and nonlinear coefficient as function of the frequencies returned by the envelope function. As in line 10, the variables, `s.Aeff_p`, `s.beta2AtPump` and `s.fR`, which are  $A_{\text{eff}}(\omega_p)$ ,  $\beta_2(\omega_p)$  and  $f_R$  receptively, are not necessarily significant to the solver, but often needed for secondary calculations along with the pump frequency.

These lines are where the true strength of the proposed code structure reveals itself. If one wants to change fiber material, e.g., shifting from silica to ZBLAN or chalcogenide, just parse the appropriate Raman response in a `Matlab`-function to the solver. Similarly, different fibers can be loaded by appropriately changing the content of the functions in lines 12 through 14.

Line 23: This line converts the electric field envelope in the time domain, to the pseudo electric field envelope in the frequency domain and IAP before inputting it to the solver.

Line 24: This is the line where the numerical integration is done. It is also where the bottle neck lies, and where vast amounts of calculation time can be spent. In this simple example the simple and built-in `Matlab`-function `ode45()` is implemented. This function should be substituted with a special-tailored integration scheme incorporating a customized adaptive step size algorithm (e.g., like the local goal error method [35]) in a more elaborate solver. Obviously, the integration scheme needs an implementation of the equation the solver should operate on, and the equation is parsed to the integration scheme as a function handle stored in `ForInt.WhatEqn`. Below, in section B.2.3 and B.2.4, is printed two examples of implementations, one of the GNLSE and one of the nonlinear Schrödinger equation (NLSE), respectively. What equation is simulated can then be defined simply by storing the correct function handle in `ForInt.WhatEqn` at call time and defining the appropriate material response and nonlinear coefficient calculating functions. Again, this versatility reveals the strength of the code structure proposed here.

Line 30-32: Results are transformed from the pseudo electric field envelope in

the frequency domain and IAP and to the time domain electric field envelope and returned along with the time and physical frequency axis.

### B.2.1 Speed Optimizing

As mentioned above, the bottleneck is in line 24, and this is no matter what numerical integration scheme is used. In this line, the GNLSE is evaluated a large number of times and a large number of discrete Fourier transforms (DFTs) are performed, so the function implementing the GNLSE-evaluation itself, shows a great potential for speed optimizing. In this respect, the use of `fftshift()` and scaling of FT (see appendix C, section C.4, page 113), should be avoided internally in the solver, until the very end, when results are returned. This can be achieved by starting the calculation in the same domain where it ends, and not perform any intermediate scaling. As a final remark, data files can be large when the number of samples is large (e.g.,  $\geq 2^{17}$ ). Therefore, it may be preferable to save data regarding the pulse, e.g., energy, peak power or photon number (see appendix F page 127), in many locations along the calculation, while only storing the entire pulse in few places. Furthermore, it is advisable not to return the time (or frequency) axis with each pulse, but only once and storing it separately.

### B.2.2 Small Example

The solver function from section B.1 is tested with a small assignment used in teaching sessions on solving the GNLSE. The full GNLSE ignoring frequency dependence of  $A_{\text{eff}}$  and  $n_{\text{eff}}$  is solved for a silica fiber with  $\beta_2 = -1.6334 \cdot 10^{-27} \text{ s}^2/\text{m}$  and  $\beta_3 = 6.4520 \cdot 10^{-41} \text{ s}^3/\text{m}$ , and  $\tilde{L} = i(\beta_2\Omega^2/2 + \beta_3\Omega^3/6)$ , with material response given by

$$R(T) = (1 - f_R)\delta(T) + f_R \frac{\tau_1^2 + \tau_2^2}{\tau_1\tau_2^2} e^{-\frac{T}{\tau_2}} \sin\left(\frac{T}{\tau_1}\right) \theta(T) \quad (\text{B.2.1})$$

where  $\tau_1 = 12.2 \text{ fs}$ ,  $\tau_2 = 32 \text{ fs}$ ,  $f_R = 0.18$  and  $\theta(T)$  is the Heaviside step function and  $\delta(T)$  is Dirac's delta-function. The nonlinear coefficient  $\gamma = 0.02942 \text{ (Wm)}^{-1}$ ,  $n_2 = 2.4 \cdot 10^{-20} \text{ m/W}$ , and  $A_{\text{eff}} = 2\pi n_2/(\lambda_p \gamma)$ . The initial condition is a Gaussian shape given by Eq. (C.1.3) with  $P_0 = 5552 \text{ W}$ ,  $T_0 = 10 \text{ fs}$ , and  $\lambda_p = 1064 \text{ nm}$ . The calculation domain stretches from,  $\lambda_{\text{min}} = 535.8 \text{ nm}$  to  $\lambda_{\text{max}} = 75.29 \text{ }\mu\text{m}$ . Care must be taken to

ensure  $\omega_p = \omega_0$ , because the given values of  $\beta_2$  and  $\beta_3$  are calculated at this expansion frequency. The time step is  $dt \approx 1.8$  fs and  $N_t = 2^{10}$  points are on the time-/frequency grids. Finally, the propagation distance is  $L = 10$  cm. The results are shown on Fig. B.1-left and right.

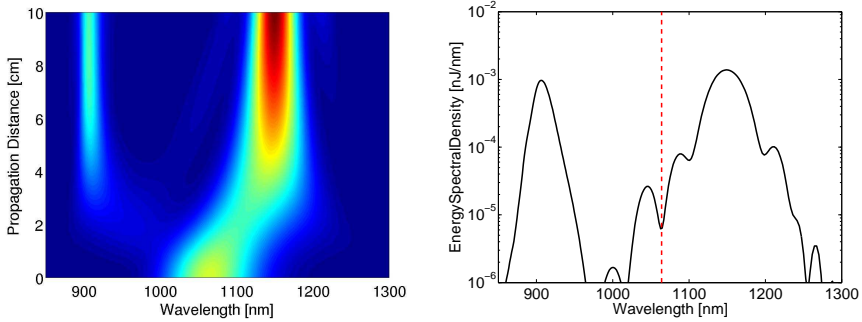


**Figure B.1:** Left: Contour plot of spectral development as function of propagation distance. Right: Spectrum after  $L = 10$  cm. Red vertical dashed line marks pump.

### B.2.3 GNLSE Implementation

```

1 function dC_tilde_IAP_dz=GNLSE(z,C_tilde_IAP,s,NLOParams)
2
3 L=s.L;R_Omega=NLOParams.R_Omega;gamma=NLOParams.gamma;
4 w0=s.w_0;W=s.Omega; % axes and data is loaded in scope of
   GNLSE
5
6 C_tilde = C_tilde_IAP.*exp(L*z);
7 C = fft(C_tilde);
8 Int = abs(C).^2;
9
10 convol = C.*fft(R_Omega.*ifft(Int));
11 dC_tilde_IAP_dz=1i*gamma.*(1+W/w0).*ifft(convol).*exp(-L*z);
   % RHS of full GNLSE in the IAP.
12
13 end

```



### B.2.4 NLSE Implementation

```
1 function dC_tilde_IAP_dz=NLSE(z,C_tilde_IAP,s,NLOpParams)
2
3 % axes and data is loaded in scope of GNLSE
4 L=s.L;gam=NLOpParams.gamma; w0=s.w_0;W=s.Omega;
5
6 C_tilde = C_tilde_IAP.*exp(L*z);
7 C = fft(C_tilde);
8
9 dC_tilde_IAP_dz=1i*gam.*ifft(C.*abs(C).^2).*exp(-L*z); % RHS
   of NLSE in the IAP.
10
11 end
```

# Appendix C

## Fourier Transforming

It is essential, when working with the generalized nonlinear Schrödinger equation (GNLSE), and building a numeric code that solves it, to be well familiar with both continues Fourier transform (FT) and discrete Fourier transform (DFT)<sup>1</sup>. The continues FT pair, transforming between time and angular frequency, used in this thesis is defined in Eq. (2.3.2) but repeated here for convenience

$$\tilde{f}(\omega) = \mathcal{F}\{f(t)\} = \int f(t)e^{i\omega t}dt \quad \text{and}$$

$$f(t) = \mathcal{F}^{-1}\{\tilde{f}(\omega)\} = \frac{1}{2\pi} \int \tilde{f}(\omega)e^{-i\omega t}d\omega.$$

As a note to the reader of this text, integration with no specified boundaries is implied to mean integration from  $-\infty$  to  $\infty$ , i.e.,  $\int = \int_{-\infty}^{\infty}$  over whichever integration variable is in question.

Numerical implementations of FTs are inherently DFTs, and working with DFT requires a certain amount of experience. Gaining this experience, and in particular making results of DFT comparable to results of continues FT, can cause serious frustrations and be exhaustively time consuming.

In this appendix, I will walk through some of the basics of the FT, starting with a few properties of common continuous functions found in nonlinear optics and some basic useful relations of FTs. After this, a

---

<sup>1</sup>One should keep a mental footnote that the framework of understanding the analytical mathematics and physics related to the GNLSE builds on the continues FT. Thus, typically, the researchers mind imagine a world of continues variables and FTs. The computer world, however, is discrete.

short review of Parseval's theorem is given because its physical meaning is significant in this setting. Parseval's theorem defines the energy spectral density (ESD), and it can be used to check that results from DFTs are scaled to be consistent with expected results from continuous FTs. In section C.4 and onwards `Matlab`'s DFT algorithm is reviewed, definitions of time and frequency axes are given, and implementation examples are printed along with a corresponding demonstration. This appendix, and in particular the last sections, can be very beneficial to read for people struggling with DFTs in `Matlab`.

## C.1 Common Pulse Shapes

In nonlinear optics one often encounters two types of bell-shaped functions used to describe the complex electric field  $A(t)$  in the time domain. The envelope function  $A(t)$  is defined in such a way that  $P(t) = |A(t)|^2$  is the instantaneous power [6, 23], and due to this definition the energy carried by such a pulse is  $E = \int |A(t)|^2 dt$ , i.e., the area under the  $|A|^2$ -curve.

### C.1.1 The Gaussian Shape

The temporal power distribution of the electric field envelope of a spatially coherent laser pulse is often modelled as a chirp-free FT-limited Gaussian function. A laboratory measurement will typically measure the power-distribution of such a pulse, and define it as

$$|A(t)|^2 = P(t) = P_0 e^{-\frac{t^2}{t_0^2}} \quad (\text{C.1.1})$$

where  $P_0$  is the peak power. Such a laser pulse will often be characterized by its full-width-at-half-maximum (FWHM) power-level, and in this case it is found from even symmetry of the Gaussian, to be  $t_{\text{FWHM}} = 2t_+$ , where  $t_+ > 0$  is the positive solution to  $P(t_+) = P_0/2$ . Thus,

$$P_0 e^{-\frac{t_+^2}{t_0^2}} = \frac{P_0}{2} \quad \Rightarrow \quad t_+ = \sqrt{\ln 2} t_0 > 0 \quad \text{and} \quad t_{\text{FWHM}} = 2\sqrt{\ln 2} t_0 \approx 1.665 t_0. \quad (\text{C.1.2})$$

The (phase-free or chirp-free) field envelope of the laser pulse is

$$A(t) = \sqrt{P(t)} = \sqrt{P_0} e^{-\frac{t^2}{2t_0^2}}. \quad (\text{C.1.3})$$

Notice here, the factor of 2 that appears in the denominator of the exponential of the electric field envelope above, and does *not* appear in the power distribution (C.1.1). This factor of 2 can easily become a source of confusion. By usual convention it belongs in the electric field envelope.

The FT of the electric field envelope is given by

$$\tilde{A}(\omega) = \int A(t)e^{i\omega t} dt = \sqrt{P_0} \int e^{-\left(\frac{t^2}{2t_0^2} - i\omega t\right)} dt = \sqrt{2\pi P_0 t_0} e^{-\frac{(\omega t_0)^2}{2}} \quad (\text{C.1.4})$$

where Eq. (18.75) from [96] was used in the last equality. The ESD (see section C.3 about Parseval's theorem) is given by

$$\text{ESD}(\omega) = |\tilde{A}(\omega)|^2 = 2\pi P_0 t_0^2 e^{-(\omega t_0)^2}. \quad (\text{C.1.5})$$

The FWHM of the ESD is then found by the same manipulations as in the time domain to give

$$\omega_{\text{FWHM}} = \frac{2\sqrt{\ln 2}}{t_0} = \frac{4 \ln 2}{t_{\text{FWHM}}}. \quad (\text{C.1.6})$$

By using Eq. (18.72) from [96], the energy in a Gaussian pulse is found to be (for the second equality see Eq. (C.3.3))

$$E = \int P_0 e^{-\frac{t^2}{t_0^2}} dt = \frac{1}{2\pi} \int 2\pi P_0 t_0^2 e^{-(\omega t_0)^2} d\omega = \sqrt{\pi} P_0 t_0. \quad (\text{C.1.7})$$

### C.1.2 The sech Shape

In the scope of nonlinear optics, a soliton is usually referred to as one of the solution to the nonlinear Schrödinger equation (NLSE), which can be found analytically. The most simple (or the fundamental) soliton is given by a secant hyperbolic function. The (phase-free) electric field envelope and power distribution of a fundamental soliton is [6]

$$A(t) = \sqrt{P_0} \text{sech}\left(\frac{t}{t_0}\right) \quad \Rightarrow \quad P(t) = P_0 \text{sech}^2\left(\frac{t}{t_0}\right). \quad (\text{C.1.8})$$

By definition it holds that  $\text{sech}(x) = 1/\cosh(x) = 2/(e^{-t/t_0} + e^{t/t_0})$ , where  $\cosh$  is the cosine hyperbolic function. As for the Gaussian function, symmetry dictates that  $t_{\text{FWHM}} = 2t_+$ , where it can be derived that  $t_+$  is

found from the solution to  $u^2 - 6u + 1 = 0$  with  $u = \exp(2t_+/t_0)$  that leads to  $t_+ > 0$ . The end result is

$$t_{\text{FWHM}} = 2t_+ = \ln(3 + 2\sqrt{2})t_0 \approx 1.7627t_0 \quad (\text{C.1.9})$$

which is the same as in [6]. The FT of the sech is

$$\begin{aligned} \tilde{A}(\omega) &= \int \sqrt{P_0} \text{sech}\left(\frac{t}{t_0}\right) e^{i\omega t} dt = 2\sqrt{P_0} \int_0^\infty \frac{\cos(\omega t)}{\cosh\left(\frac{t}{t_0}\right)} dt \\ &= \pi \sqrt{P_0} t_0 \text{sech}\left(\frac{\omega \pi t_0}{2}\right) \end{aligned} \quad (\text{C.1.10})$$

where it was used that  $\exp(i\omega t) = \cos(\omega t) + i \sin(\omega t)$ , that  $\text{sech}(t/t_0) = 1/\cosh(t/t_0)$  is an even function, that a product of two even functions is even, and finally Eq. (18.113) [96]. The ESD is

$$\text{ESD}(\omega) = |\tilde{A}(\omega)|^2 = \pi^2 P_0 t_0^2 \text{sech}^2\left(\frac{\omega \pi t_0}{2}\right). \quad (\text{C.1.11})$$

By same reasoning as in the time domain, the frequency FWHM ESD level is

$$\omega_{\text{FWHM}} = \frac{2 \ln(3 + 2\sqrt{2})}{\pi t_0}. \quad (\text{C.1.12})$$

The energy carried by a soliton is

$$\begin{aligned} E &= \int P_0 \text{sech}^2\left(\frac{t}{t_0}\right) dt = \\ &= \frac{1}{2\pi} \int \pi^2 P_0 t_0^2 \text{sech}^2\left(\frac{\omega \pi t_0}{2}\right) d\omega = 2P_0 t_0 \end{aligned} \quad (\text{C.1.13})$$

where it was used that  $\int \text{sech}^2(u) du = 2$ . For the second equality above see Eq. (C.3.3).

## C.2 A Few Needed Relations

### C.2.1 The $\delta$ -function

The Dirac delta function is given by

$$\begin{aligned} \delta(\omega) &= \frac{1}{2\pi} \int e^{i\omega t} dt, \quad \text{and has the property} \\ \tilde{f}(\omega_0) &= \int \tilde{f}(\omega) \delta(\omega - \omega_0) d\omega. \end{aligned} \quad (\text{C.2.1})$$

In particular for  $\tilde{f}(\omega) = 1$  then  $\tilde{f}(\omega_0) = 1 = \int \delta(\omega - \omega_0) d\omega$  is the area under the  $\delta$ -function for any  $\omega_0$ .

### C.2.2 Transforming the Differential Operator

With the used definition of the FT pair, the differential operator  $\partial_t$  transforms as

$$\mathcal{F} \left\{ \frac{\partial A}{\partial t} \right\} = \int \frac{\partial A}{\partial t} e^{i\omega t} dt = [Ae^{i\omega t}]_{-\infty}^{\infty} - i\omega \int A e^{i\omega t} dt = -i\omega \tilde{A}. \quad (\text{C.2.2})$$

where the  $[Ae^{i\omega t}]$ -term vanishes if  $A$  is a square integrable function, which is a requirement for it to have a FT. The process can be repeated  $k$  times to yield  $\partial^k / \partial t^k \rightarrow (-i\omega)^k$ . The reverse will also be true, so that

$$\mathcal{F}^{-1} \left\{ -i\omega \tilde{A} \right\} = \mathcal{F}^{-1} \mathcal{F} \left\{ \frac{\partial A}{\partial t} \right\} = \frac{\partial A}{\partial t} \quad (\text{C.2.3})$$

and  $-i\omega \rightarrow \partial / \partial t$ .

### C.2.3 FT of Real Valued Function

For a real valued function  $f(t)$  of the real variable  $t$ , one has

$$\tilde{f}^*(\omega) = \left[ \int f(t) e^{i\omega t} dt \right]^* = \int f(t) e^{i(-\omega)t} dt = \tilde{f}(-\omega) \quad (\text{C.2.4})$$

and from this it follows that

$$\begin{aligned} \tilde{f}'(\omega) - i\tilde{f}''(\omega) &= \tilde{f}'(-\omega) + i\tilde{f}''(-\omega) \Rightarrow \\ \tilde{f}'(\omega) &= \tilde{f}'(-\omega) \quad \text{and} \quad \tilde{f}''(\omega) = -\tilde{f}''(-\omega) \end{aligned} \quad (\text{C.2.5})$$

so the real part,  $\tilde{f}'$ , of  $\tilde{f}(\omega)$  is even and the imaginary part,  $\tilde{f}''$ , is odd.

## C.3 Parseval's Theorem

Parseval's theorem is very important to bare in mind, because it defines the ESD, and because it can be used to check that ones implementations of DFTs are consistent with what is expected from continues FTs. At first sight the mathematical formulation can seem cumbersome; for two

complex-valued functions  $f(t)$  and  $g(t)$  of the real variable  $t$  one can calculate

$$\begin{aligned}\int f(t)g^*(t)dt &= \int \frac{1}{2\pi} \int \tilde{f}(\omega)e^{-i\omega t}d\omega \left[ \frac{1}{2\pi} \int \tilde{g}(\omega')e^{-i\omega' t}d\omega' \right]^* dt \\ &= \frac{1}{(2\pi)^2} \int \tilde{f}(\omega)\tilde{g}^*(\omega')e^{-i(\omega-\omega')t}d\omega d\omega' dt. \quad (\text{C.3.1})\end{aligned}$$

Integrating over  $t$ , recognizing the Dirac  $\delta$ -function (see Eq. (C.2.1)), and then integrating over  $\omega'$  will give

$$\begin{aligned}\int f(t)g^*(t)dt &= \frac{2\pi}{(2\pi)^2} \int \tilde{f}(\omega) \left[ \int \tilde{g}^*(\omega')\delta(\omega' - \omega)d\omega' \right] d\omega \\ &= \frac{1}{2\pi} \int \tilde{f}(\omega)\tilde{g}^*(\omega)d\omega. \quad (\text{C.3.2})\end{aligned}$$

Now one can comprehend why Parseval's theorem is important. In the special case when  $f = g = A(t)$ , Parseval's theorem straight forwardly states that the energy in a pulse

$$E = \int |A(t)|^2 dt = \frac{1}{2\pi} \int |\tilde{A}(\omega)|^2 d\omega = \int |\tilde{A}(\nu)|^2 d\nu \quad (\text{C.3.3})$$

is the same in both the time- and frequency ( $\nu = \omega/(2\pi)$ ) domain. This physical interpretation, that may seem obvious, makes a simple and very powerful mnemonic for the theorem. In another formulation, Parseval's theorem states that the area under the power distribution  $|A(t)|^2$  must be the same as the area under the  $|\tilde{A}(\omega)|^2$ -curve (albeit the factor of  $1/(2\pi)$ ). Parseval's theorem thus defines the energy spectral density  $\text{ESD}(\omega) = |\tilde{A}(\omega)|^2$  as the frequency domain analogue to the time domain power distribution. Calculating the energy in both time- and frequency domain by integration of  $|A(t)|^2$  and  $|\tilde{A}(\omega)|^2$  respectively can be used to check if the results of DFTs are scaled correctly to be compared with results from continues FTs.

Finally, one should take care not to confuse the ESD with the FT of the power-distribution  $\tilde{P}(\omega) = \mathcal{F}\{P(t)\} \neq |\tilde{A}(\omega)|^2$ . The *only place*, I have encountered, where one needs to calculate the FT of the power distribution is when finding the convolution integral in the GNLSE including the delayed Raman response.

### C.3.1 ESD in Wavelength Domain

The ESD is often visualized, as a function of wavelength, i.e., as  $\text{ESD}(\lambda)$ . To keep the definition of  $\text{ESD}(\lambda)$  in thread with Parseval's theorem, so

that the area under the  $\text{ESD}(\lambda)$ -curve is the total energy in the spectrum, then

$$E = \int_0^\infty \text{ESD}(\lambda) d\lambda = \frac{1}{2\pi} \int_0^\infty |\tilde{A}(\omega)|^2 d\omega \quad (\text{C.3.4})$$

where only positive wavelengths are included. To identify  $\text{ESD}(\lambda)$  the following transformation is needed

$$\lambda = \frac{2\pi c}{\omega} \Rightarrow \frac{d\lambda}{d\omega} = \frac{d}{d\omega} \left( \frac{2\pi c}{\omega} \right) \Rightarrow d\omega = -\frac{2\pi c}{\lambda^2} d\lambda. \quad (\text{C.3.5})$$

Inserting this in (C.3.4) while the integration limits transform as  $\omega = 0 \Rightarrow \lambda = \infty$  and  $\omega = \infty \Rightarrow \lambda = 0$  then

$$E = \int_0^\infty \text{ESD}(\lambda) d\lambda = - \int_\infty^0 c \frac{|\tilde{A}(\lambda)|^2}{\lambda^2} d\lambda = \int_0^\infty c \frac{|\tilde{A}(\lambda)|^2}{\lambda^2} d\lambda. \quad (\text{C.3.6})$$

Thus, the ESD in the wavelength domain can be read off above to be  $\text{ESD}(\lambda) = c|\tilde{A}(\lambda)|^2/\lambda^2$ . The ESD is a characteristic of a single spectrum, or equivalently a single shot in a pulsed system. The power spectral density (PSD), i.e., the ESD per time instead of per shot, is given by  $\text{PSD} = f_{\text{rep}} \text{ESD}$ , where  $f_{\text{rep}}$  is the seed laser repetition rate.

## C.4 Fourier Transform in Matlab

When a function is sampled, and known function values are separated by a constant amount  $\Delta t$  (or  $\Delta\omega$ ), the continuous FTs are replaced by DFTs. The sampling causes the following substitutions to be made,  $dt \rightarrow \Delta t$  (or  $d\omega \rightarrow \Delta\omega$ ) and  $\int \rightarrow \sum$  so that

$$\tilde{f}(\omega_k) = \int f(t) e^{i\omega_k t} dt \approx \sum_n f_n e^{i\omega_k t_n} \Delta t = \tilde{f}_k \quad \text{for } k, n = 1, \dots, N \quad (\text{C.4.1})$$

i.e., the  $k$ 'th point in the vector  $\tilde{f}_k$  is an approximation of the value  $\tilde{f}(\omega = \omega_k)$  of the continuous FT.

The DFT implemented by default in **Matlab** is known as the fast Fourier transform (FFT), with function names **fft()**, and **ifft()** for inverse Fourier Transform (iFT). By definition they are given by [97]

$$X_k = \sum_{j=1}^N x_j e^{-\frac{2\pi i(j-1)(k-1)}{N}} \quad \text{and} \quad x_j = \frac{1}{N} \sum_{k=1}^N X_k e^{\frac{2\pi i(j-1)(k-1)}{N}} \quad (\text{C.4.2})$$



respectively, where  $j$  and  $k$  are summation variables and  $N$  is the number of samples in the vectors  $x_j$  and  $X_k$ . The DFT-algorithms have implicit periodic boundary conditions, i.e, the  $k = n + N$ 'th ( $j = n + N$ 'th) point is the same as the  $k = n$ 'th ( $j = n$ 'th), where  $n$  is some integer in the range from 1 to  $N$ , which can be realized by insertion. These boundary conditions can cause cyclic effects in the calculation domain during solution of the GNLSE.

Because Eq. (C.4.2) differ slightly from the sum in Eq. (C.4.1) that approximates the continuous FT used here, an implementation of **Matlab**'s DFTs, that cause output to be directly comparable to results from the continuous FT, require a few manipulations:

1. The sign convention in Eq. (2.3.2) is opposite of the one implemented by **Matlab**. Strictly speaking this is a pedantic concern, and not so significant, but can be overcome by using `ifft()` for FT and `fft()` for iFT.
2. The normalization by the number of samples  $N$  in the last expression in Eq. (C.4.2) should be replaced by proper normalization with  $2\pi$ .
3. The end result should be correctly scaled with the sample spacing  $\Delta t$  ( $\Delta\omega$ ) for FT (iFT).

In a hybrid formulation, that mixes **Matlab**-syntax and regular math slightly, the above points are summarized as

$$\tilde{f} = \text{ifft}(f)N\Delta t \quad \text{and} \quad f = \text{fft}(\tilde{f})\frac{\Delta\omega}{2\pi} \quad (\text{C.4.3})$$

where  $f$  ( $\tilde{f}$ ) is the vector for FT (iFT).

A final word of notice; by inserting  $j = 1$  ( $k = 1$ ) in Eq. (C.4.2), it is seen that the first element of the vector for FT (iFT) corresponds to the  $\omega = 0$  ( $t = 0$ ) -component. This means that when arranging a vector for FT the first element *must* be the element corresponding to  $t = 0$  ( $\omega = 0$ ). If a vector is transformed in **Matlab**, and the first element does not correspond to  $t = 0$  ( $\omega = 0$ ), the result will be imposed with a phase factor corresponding to the displacement. This is realized from the following calculation, illustrating the FT of a function with a time

domain displacement,

$$\begin{aligned} \int f(t - t_0) e^{i\omega t} dt &= \int f(q) e^{i\omega(q+t_0)} dq \\ &= e^{i\omega t_0} \int f(q) e^{i\omega q} dq = e^{i\omega t_0} \tilde{f}(\omega). \end{aligned} \quad (\text{C.4.4})$$

A similar phase factor will be imposed on the iFT of a vector with a frequency domain displacement. It is usually for rearranging vectors, with the purpose of bringing the  $t = 0$  ( $\omega = 0$ ) element into the first slot of the vector before transforming it, that one uses Matlab-functions `fftshift()` and `ifftshift()`.

### C.4.1 Making the Time and Frequency Axes

When finding the FT of a discrete signal, where samples are spaced by  $\Delta t$ , a corresponding discrete grid of frequencies must be calculated to ensure a correct spectral representation of a FT. This section describes how.

The normalized frequencies corresponding to a DFT,  $u$ , given by

$$u = \frac{\omega}{\omega_s} = \frac{\omega \Delta t}{2\pi} \quad (\text{C.4.5})$$

are imposed with the requirement  $|u| \leq 1/2$  [98]. In the above expression  $\omega_s = 2\pi F_s$ , where  $F_s = 1/\Delta t$  is the sampling frequency, and  $\omega$  is the physical frequency. This gives a bandwidth of  $u_B = 1$  or  $\omega_B = \omega_s$ . With  $N$  samples, the normalized frequency step is  $\Delta u = 1/N$ , while the physical angular frequency separation becomes

$$\Delta\omega = \frac{\omega_B}{N} = \frac{2\pi F_s}{N} = \frac{2\pi}{N\Delta t}. \quad (\text{C.4.6})$$

The  $N$  normalized frequencies defining the axis, are then placed equidistantly from  $u = -1/2$  in increments of  $\Delta u$ . The physical axis is then obtained from multiplication by  $\omega_B = N\Delta\omega$ . All in all, one ends with the general definition of a zero-centered axis (the  $N/2 + 1$ 'th element is zero), here in Matlab-notation:

```
x = -(N/2):(N/2-1)* dx;
```

where  $\mathbf{x}$  can be any of the axes variables needed. Notice, that  $N/2$  is an integer, if one takes  $N = 2^k$ , with positive integer  $k$ . This is a wise choice

because *Matlab* will pad a vector for FT with zeros until nearest larger  $2^k$  number of samples. Notice, that the definition above is zero-centered, and must be rearranged using `fftshift()` (or `ifftshift()`) before issuing the DFT or the phase mentioned in Eq. (C.4.4) will be imposed on the result.

### C.4.2 Using the Provided Matlab Functions

In sections C.4.3 and C.4.4 are provided two *Matlab*-functions that perform a DFT on samples from a continues function and scale the results, so they are comparable to the expected result from FT of a continues function. The functions take a zero-centered axis-vector, and corresponding function values, and return the correctly scaled FT (iFT). If need be, the functions will also return the corresponding axis for the FT (iFT). The performance of the functions are illustrated in Fig. C.1, where a Gaussian and sech function (see Eqns. (C.1.3) and (C.1.8)) are defined in the time domain, transformed to the frequency domain and transformed back again. The data shown can be generated by running:

```
t0_g = 1;t0_s = 1/2*t0_g;P0 = 1;Nt = 2^8;Tp = 20;dt = Tp/Nt;
t = (-(Nt/2):(Nt/2-1)).' * dt;
y_analy = sqrt(P0) * exp(-t.^2/(2*t0_g^2));
y2_analy = sqrt(P0)*sech(t/t0_s);
[y_tilde omega] = funcAgrawalFT(t,y_analy);
y2_tilde = funcAgrawalFT(t,y2_analy);
y_tilde_analy = sqrt(2*pi*P0)*t0_g*exp(-(omega*t0_g).^2/2);
y2_tilde_analy = pi*sqrt(P0)*t0_s*sech(omega*pi*t0_s/2);
y = funcAgrawaliFT(omega,y_tilde);
y2 = funcAgrawaliFT(omega,y2_tilde);
```

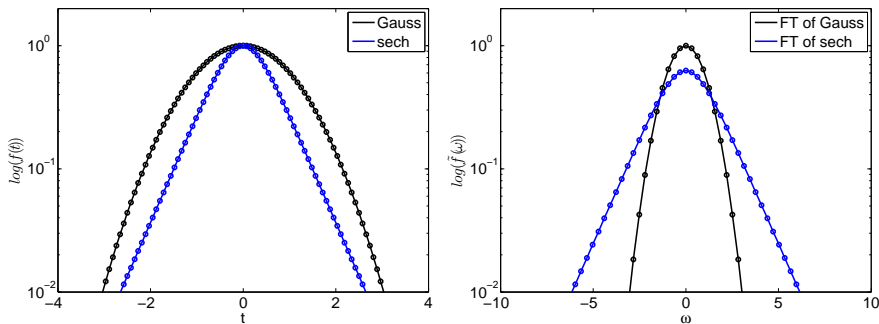


**Figure C.1:** Left: Gaussian and sech functions given by (C.1.3) and (C.1.8) plotted along with results of  $\mathcal{F}^{-1}\mathcal{F}\{f(t)\} = f(t)$  from *Matlab*. Right: Expected analytical results from (C.1.4) and (C.1.10) and results of  $\mathcal{F}\{f(t)\}$  from *Matlab*.

## C.4.3 funcAgrawalFT.m

```

1 function [f_tilde, omega]=funcAgrawalFT(t,f)
2
3 %%% Function for performing the Fourier Transform (FT)
4     according to
5     %%% the definition of the continues FT in in this work.
6
7 Nt=length(t); % Number of points on time grid
8 Dt=abs(t(2)-t(1)); % Time step
9
10 Domega=2*pi/(Nt*Dt); % Angular freq. step.
11 omega=(-(Nt/2):(Nt/2-1)).'*Domega; % Angular freq. axis
12
13 f=fftshift(f); % manipulating position of t=0-element
14 f_tilde=ifft(f)*Nt*Dt; % Performing transform and scaling
15 f_tilde=ifftshift(f_tilde); % re-manipulating position of
16     omega = 0-element
17 end

```

## C.4.4 funcAgrawaliFT.m

```

1 function [f, t]=funcAgrawaliFT(omega,f_tilde)
2
3 %%% Function for performing the inverse Fourier Transform (FT
4     )
5     %%% according to the definition of the continues FT in this
6     work.
7
8 Nomega=length(omega); % length of signal
9 Domega=abs(omega(2)-omega(1)); % anuglar freq. step
10
11 Dt=2*pi/(Nomega*Domega); % time step
12 t=(-(Nomega/2):(Nomega/2-1)).'*Dt; % time axis
13
14 f_tilde=fftshift(f_tilde); % Manipulating position of DC-
15     element
16 f_tilde=fft(f_tilde)*Domega/(2*pi); % Performing transform
17 f=ifftshift(f_tilde); % Re-manipulating position of DC-
18     element
19 end

```



## Appendix D

# Expansion Frequency and Pseudo Frequency Axis

In the literature it is often times found that the expansion frequency  $\omega_0$  of the calculation domain used in solving the generalized nonlinear Schrödinger equation (GNLSE), coincides with the frequency of the pump  $\omega_p$  [6, 14]. In this appendix it is investigated why  $\omega_p$  is not always useful as the expansion frequency, and it is reviewed, how to determine an expansion frequency that is always useful.

### D.1 Identical Expansion and Pump Frequency

Firstly, the expansion frequency  $\omega_0$  is the center or mean frequency of the calculation domain, or equivalently, it is the zero-frequency component of the pseudo frequency axis  $\Omega$ , because of the definition  $\Omega = \omega - \omega_0$ , where  $\omega$  is the physical angular frequency. When solving the GNLSE, Fourier transforms (FTs) are performed between the retarded time frame  $T$  and pseudo frequency  $\Omega$  (see appendix E page 123). A pulse envelope, e.g., defined as in (C.1.3) and used as initial condition for solving the GNLSE, has a spectrum given by Eq. (C.1.4), and repeated here

$$A = \sqrt{P_0} e^{-\frac{T^2}{2t_0^2}} \quad \Rightarrow \quad \tilde{A}(\Omega) = \sqrt{2\pi P_0 t_0} e^{-\frac{(\Omega t_0)^2}{2}}. \quad (\text{D.1.1})$$

It is clearly seen that the spectral maximum is at  $\Omega = 0$  or  $\omega = \omega_0$ , and so, if one has defined the calculation domain with  $\omega_0 = \omega_p$ , the spectrum peaks at  $\omega_p$  and it is correctly placed on the pseudo frequency axis directly

from its FT. A requirement on the calculation domain however, must be, that the smallest frequency  $\omega_{\min}$  is positive. This means that

$$\omega_0 = \frac{\omega_{\max} + \omega_{\min}}{2} \Rightarrow 0 < \omega_{\min} = 2\omega_0 - \omega_{\max} \Rightarrow \omega_{\max} < 2\omega_0 \quad (\text{D.1.2})$$

and thus, if  $\omega_0 = \omega_p$  and one has a pump wavelength of, e.g.,  $\lambda_p = 2\pi c/\omega_p = 2 \mu\text{m}$  then the calculation domain can never stretch below  $\lambda_p/2 = 1 \mu\text{m}$ . A priori, one can easily expect broad band supercontinuum (SC) generated by a pump at  $\lambda_p = 2 \mu\text{m}$  to stretch below  $\lambda_{\min} = 1 \mu\text{m}$ , and thus one cannot always allow a calculation domain with  $\omega_0 = \omega_p$ .

## D.2 Non-identical Expansion and Pump Frequency

Another, and more general approach to finding an expansion frequency  $\omega_0$ , than just taking  $\omega_0 = \omega_p$  as outlined above, is to define a desired wavelength range for the calculation domain at the onset of a simulation, and letting this determine the expansion frequency. Such a procedure is highly intuitive and also practical, because the linear propagation properties of the fiber under investigation is often only known in a finite wavelength range, and the calculation domain should be contained in this range of known properties. Fig. D.1 illustrates how the conversion from a physical wavelength window to the pseudo frequency axis is performed, while ensuring purely positive physical frequencies (if  $\lambda_{\max} > \lambda_{\min} > 0$ ). Generally this procedure will lead to  $\omega_0 \neq \omega_p$ .

As in the last section, however, the FT of the initial condition, e.g., given by (D.1.1), returns a pulse with an energy spectral density (ESD) maximum at  $\omega_0$ , which is now different from the desired pump frequency  $\omega_p$ . To correct this, so the ESD maximum of the initial condition is positioned correctly at the pump frequency on the pseudo frequency axis, a chirp must be added to it, according to the frequency domain analogue of the rule in Eq. (C.4.4). The situation is illustrated in Fig. D.1 where an initial condition is translated from the center on the pseudo frequency axis and to  $\Omega = -(\omega_0 - \omega_p)$ .

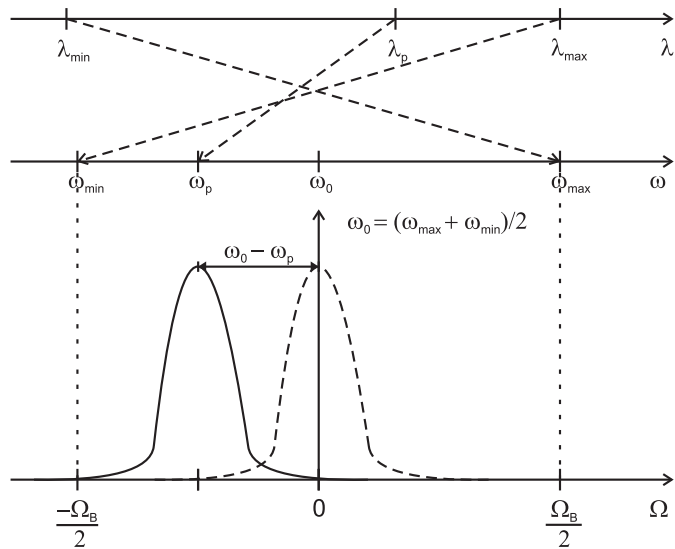


**Figure D.1:** Illustration of the relation between the wavelength and the pseudo frequency axes with bandwidth  $\Omega_B = \omega_{\max} - \omega_{\min}$ .





## Appendix E

# Why the Pump Frequency Appears in the Linear Operator

At a first glance when inspecting the generalized nonlinear Schrödinger equation (GNLSE) (Eq. (2.3.5)) and corresponding definition of the linear operator (Eq. (2.3.8))

$$\tilde{L}(\omega) = i \{ \beta(\omega) - [\beta(\omega_0) + \beta_1(\omega_p)(\omega - \omega_0)] \} - \frac{\alpha(\omega)}{2}$$

it seems that the pump frequency  $\omega_p$  appears out of place in a Taylor-series expansion

$$\beta(\omega) - [\beta(\omega_0) + \beta_1(\omega_0)(\omega - \omega_0)] = \sum_{k \geq 2} \frac{\beta_k(\omega_0)}{k!} (\omega - \omega_0)^k \quad \text{with } \beta_k = \frac{d\beta}{d\omega}$$

of the propagation constant  $\beta$ . The statement in Eq. (2.3.8), however, is correct, and in this appendix, I give a short derivation of why this is the case. It must be noted here, that the expansion frequency  $\omega_0$  is the mean frequency in the calculation domain (see appendix D page 119), and in this work, it is defined from the wavelength window desired in a given simulation, while the pump frequency  $\omega_p$  is physically determined by whatever pump source is investigated.

## E.1 The Retarded Time Frame

A comprehensive way to see how the pump frequency  $\omega_p$  enters the linear operator in the GNLSE (Eq. (2.3.5)), is to follow the derivation for the frequency domain electric field envelope  $\tilde{A}(z, \omega)$  found in [6]. Starting from Eq. (2.3.22) in [6], we have

$$\frac{\partial \tilde{A}}{\partial z} = i[\beta(\omega) - \beta_0] \tilde{A} + i\Delta\beta \tilde{A} \quad (\text{E.1.1})$$

where  $\beta_0 = \beta(\omega_0)$  and  $\Delta\beta$  is a term that will become the nonlinear operator [6]. The term  $i[\beta - \beta_0]$  accounts for the phase change accumulated during propagation caused by dispersion, and will become the linear operator. In this derivation, attenuation is ignored entirely, and this can be done without loss of generality. Furthermore, also the nonlinear effects can be ignored without loss of generality, and this amounts to  $\Delta\beta = 0$  ( $\gamma = 0$ ). With  $\Delta\beta = 0$  Eq. (E.1.1) accounts only for dispersion induced changes to  $\tilde{A}$ , during propagation.

The propagation constant  $\beta(\omega)$  can be Taylor-expanded around any arbitrary  $\omega_0$  by

$$\beta(\omega) = \beta_0 + \sum_{k \geq 1} \frac{\Omega^k}{k!} \left. \frac{d^k \beta}{d\omega^k} \right|_{\omega_0} \quad (\text{E.1.2})$$

where  $\Omega = \omega - \omega_0$ . Inserting this Taylor-expansion in (E.1.1), and performing a Fourier transform (FT) to the time domain, using that  $\Omega^k \rightarrow (i\partial/\partial t)^k$  (see Eqs. (C.2.2) and (C.2.3)), then

$$\frac{\partial A}{\partial z} = i \left[ \beta_0 + i\beta_1(\omega_0) \frac{\partial}{\partial t} - \frac{\beta_2(\omega_0)}{2} \frac{\partial^2}{\partial t^2} - i \frac{\beta_3(\omega_0)}{3!} \frac{\partial^3}{\partial t^3} + \dots - \beta_0 \right] A. \quad (\text{E.1.3})$$

Introducing the coordinate transform

$$\begin{aligned} Z = z & \Rightarrow \partial Z = \partial z, & \text{and} \\ T = t - \frac{z}{s} & \Rightarrow \partial T = \partial t, & \text{and} \quad \partial T = -\frac{\partial z}{s} \end{aligned} \quad (\text{E.1.4})$$

where  $s$  is some arbitrary velocity, signifying the speed of the moving time window  $T$ , will give

$$\frac{\partial A}{\partial z} = \frac{\partial A}{\partial Z} \frac{\partial Z}{\partial z} + \frac{\partial A}{\partial T} \frac{\partial T}{\partial z} = \frac{\partial A}{\partial Z} - \frac{1}{s} \frac{\partial A}{\partial T} \quad (\text{E.1.5})$$

by using the chain rule. For notational convenience the substitution  $Z \rightarrow z$  is made, i.e., lower case  $z$  is considered the longitudinal spatial coordinate. Inserting in (E.1.3) one gets

$$\frac{\partial A}{\partial z} - \frac{1}{s} \frac{\partial A}{\partial T} = i \left[ \beta_0 + i\beta_1(\omega_0) \frac{\partial}{\partial T} - \frac{\beta_2(\omega_0)}{2} \frac{\partial^2}{\partial T^2} + \dots - \beta_0 \right] A. \quad (\text{E.1.6})$$

Going back to the frequency domain (notice, that now  $T$  (and not  $t$ ) is transformed into  $\Omega$ ), then

$$\frac{\partial \tilde{A}}{\partial z} + \frac{i\Omega}{s} \tilde{A} = i \left[ \beta_0 + \beta_1(\omega_0)\Omega + \frac{\beta_2(\omega_0)}{2}\Omega^2 + \dots - \beta_0 \right] \tilde{A}. \quad (\text{E.1.7})$$

All but the last term in the parentheses above is the Taylor-expansion of  $\beta$  from Eq. (E.1.2), and thus

$$\frac{\partial \tilde{A}}{\partial z} = i \left[ \beta(\omega) - \left( \beta_0 + \frac{\Omega}{s} \right) \right] \tilde{A}. \quad (\text{E.1.8})$$

Before solving Eq. (E.1.8), one may chose an arbitrary propagation-speed  $s$ , for the reference frame  $T$ , but if the scope of solving it, is to observe a meaningful result for the pulse development, one must take it to be at least approximately equal to the speed the pulse envelope travels down the fiber. A way to ensure the reference frame  $T$  moves with approximately this speed, is to use the group velocity at the pump frequency, so

$$s = v_g = \frac{1}{\beta_1(\omega_p)} \quad (\text{E.1.9})$$

since this is the speed the light pulse will travel, at least initially, until significant spectral broadening sets in. So then, finally

$$\frac{\partial \tilde{A}}{\partial z} = i \{ \beta(\omega) - [\beta(\omega_0) + \beta_1(\omega_p)(\omega - \omega_0)] \} \tilde{A}. \quad (\text{E.1.10})$$

It has now been illustrated why  $\omega_p$  appears in the  $\tilde{\mathcal{L}}$  operator (Eq. (2.3.8)). It appears here, to account for the propagation speed of the retarded time frame  $T$  and not because only the  $k \geq 2$  terms of the Taylor-expansion (E.1.2) are needed in linear operator for the GNLSE. In the case where one deliberately chooses  $\omega_0 = \omega_p$ , then it turns out, that only the  $k \geq 2$  terms are needed, but otherwise not. It is, however, not always possible to have  $\omega_0 = \omega_p$  (see appendix D page 119).

Notice, that results presented in the time frame of Eq. (E.1.4) with  $s = v_g(\omega_p)$ , are all presented relative to the frequency component at the pump frequency, and because of it, all illustrations in this work of a time domain visualization are presented as a *delay*. This is a delay, that can be both positive and negative.

## Appendix F

# Conserved Quantity in the IAP GNLSE

It has been shown that the generalized nonlinear Schrödinger equation (GNLSE) for the complex electric field envelope  $A(z, T)$  conserves a quantity called the photon number [36] when loss can be neglected and the linear operator  $\hat{\tilde{L}}$  is not a function of propagation distance (i.e., no fiber taper etc.). The transformation into the interaction picture (IAP) and changing the GNLSE to better include the frequency dependence of the effective area as suggested in [17], warrants a correction to the usual definition of the photon number. In this appendix an expression for the photon number in the context of this modified version of the GNLSE in the IAP is derived. This quantity is important because it is used to check, if a GNLSE solver generates trustworthy results.

### F.1 Deriving the Photon Number in the IAP GNLSE

The IAP GNLSE is found in Eq. (2.3.5)

$$\frac{\partial \tilde{C}_I}{\partial z} = i\bar{\gamma}e^{-z\hat{\tilde{L}}} \left[ 1 + \frac{\omega - \omega_0}{\omega_0} \right] \mathcal{F} \left\{ C(T) \int R(T - T') |C(T')|^2 \right\} \quad (\text{F.1.1})$$

with  $\hat{\tilde{L}}$  and  $\bar{\gamma}$  defined in Eqs. (2.3.8) and (2.3.9) respectively. It can be written as

$$\frac{\partial \tilde{C}_I}{\partial z} = ibe^{-z\hat{\tilde{L}}} \kappa \tilde{g} \quad (\text{F.1.2})$$

when the following abbreviations

$$\tilde{g} = \tilde{g}(\omega) = \mathcal{F} \left\{ C(T) \int R(T - T') |C(T')|^2 \right\} \quad (\text{F.1.3})$$

and

$$\bar{\gamma}(\omega) \left[ 1 + \frac{\omega - \omega_0}{\omega_0} \right] = \frac{n_2 n_0}{c \sqrt{A_{\text{eff}}(\omega_0)} n_{\text{eff}}(\omega) \sqrt{A_{\text{eff}}(\omega)}} \omega = b\kappa(\omega) \quad (\text{F.1.4})$$

are used. Now starting from (F.1.1), multiplying on both sides by  $\tilde{C}_I^*$  and adding the complex conjugate then

$$\begin{aligned} \tilde{C}_I^* \frac{\partial \tilde{C}_I}{\partial z} + \text{c.c.} &= ibe^{-z\tilde{L}} \kappa \tilde{C}_I^* \tilde{g} + \text{c.c.} \quad \Rightarrow \\ \frac{\partial |\tilde{C}_I|^2}{\partial z} &= ib\kappa e^{-z(\tilde{L} + \tilde{L}^*)} \tilde{C}_I^* \tilde{g} + \text{c.c.} \end{aligned} \quad (\text{F.1.5})$$

where it was used that  $\partial_z |\tilde{C}_I|^2 = \partial_z (\tilde{C}_I^* \tilde{C}_I) = \tilde{C}_I^* \partial_z \tilde{C}_I + \tilde{C}_I \partial_z \tilde{C}_I^*$ . Now using  $\tilde{L} + \tilde{L}^* = 2\text{Re}(\tilde{L})$  then

$$\frac{\partial |\tilde{C}_I|^2}{\partial z} = b\kappa e^{-2z\text{Re}\tilde{L}} \left( i\tilde{C}_I^* \tilde{g} + \text{c.c.} \right) = ib\kappa e^{-2z\text{Re}\tilde{L}} \left( \tilde{C}_I^* \tilde{g} - \tilde{C}_I \tilde{g}^* \right). \quad (\text{F.1.6})$$

If loss can be neglected then  $\text{Re}(\tilde{L}) = 0$  and thus, dividing by  $b\kappa(\omega)$  and integrating over angular frequency then

$$\frac{\partial}{\partial z} \int \frac{|\tilde{C}_I|^2}{b\kappa} d\omega = i \int \left( \tilde{C}_I^* \tilde{g} - \tilde{C}_I \tilde{g}^* \right) d\omega. \quad (\text{F.1.7})$$

Next comes the calculation of the integrand on the right-hand side (RHS) above. We start by considering the function  $\tilde{g}(\omega)$  from (F.1.3) and initially look at the convolution. One has

$$\begin{aligned} \text{conv} &= \int R(T - T') |C(T')|^2 dT' \\ &= \int dT' \frac{1}{2\pi} \int \tilde{R}(\omega_1) e^{-i(T-T')\omega_1} d\omega_1 \frac{1}{2\pi} \int \tilde{C}(\omega_2) e^{-i\omega_2 T'} d\omega_2 \\ &\quad \times \left[ \frac{1}{2\pi} \int \tilde{C}(\omega_3) e^{-iT'\omega_3} d\omega_3 \right]^* \end{aligned} \quad (\text{F.1.8})$$

or

$$\begin{aligned}
 \text{conv} &= \frac{1}{(2\pi)^3} \int d\omega_1 d\omega_2 d\omega_3 \tilde{R}(\omega_1) \tilde{C}(\omega_2) \tilde{C}^*(\omega_3) e^{-i\omega_1 T} \int dT' e^{i(\omega_1 - [\omega_2 - \omega_3])T'} \\
 &= \frac{2\pi}{(2\pi)^3} \int d\omega_1 d\omega_2 d\omega_3 \tilde{R}(\omega_1) \tilde{C}(\omega_2) \tilde{C}^*(\omega_3) e^{-i\omega_1 T} \delta(\omega_1 - [\omega_2 - \omega_3]) \\
 &= \frac{1}{(2\pi)^2} \int d\omega_2 d\omega_3 \tilde{R}(\omega_2 - \omega_3) \tilde{C}(\omega_2) \tilde{C}^*(\omega_3) e^{-i(\omega_2 - \omega_3)T} \quad (\text{F.1.9})
 \end{aligned}$$

where integration over  $T'$  was done, and where Dirac's delta-function  $\delta(\omega)$  was introduced (see Eq. (C.2.1) page 110) before integrating over  $\omega_1$ . The time domain version of Eq. (F.1.3) is

$$\begin{aligned}
 g(T) &= C(T) \cdot \text{conv} = \frac{\text{conv}}{2\pi} \int \tilde{C}(\omega_4) e^{-i\omega_4 T} d\omega_4 \\
 &= \frac{1}{(2\pi)^3} \int d\omega_2 d\omega_3 d\omega_4 \tilde{R}(\omega_2 - \omega_3) \Sigma e^{-i(\omega_2 - \omega_3 + \omega_4)T} \quad (\text{F.1.10})
 \end{aligned}$$

where another abbreviation,  $\Sigma = \Sigma(\omega_2, \omega_3, \omega_4) = \tilde{C}(\omega_2) \tilde{C}^*(\omega_3) \tilde{C}(\omega_4)$ , was made. Performing Fourier transform (FT) then

$$\begin{aligned}
 \tilde{g}(\omega) &= \int dT e^{i\omega T} \frac{1}{(2\pi)^3} \int d\omega_2 d\omega_3 d\omega_4 \tilde{R}(\omega_2 - \omega_3) \Sigma e^{-i(\omega_2 - \omega_3 + \omega_4)T} \\
 &= \frac{1}{(2\pi)^3} \int d\omega_2 d\omega_3 d\omega_4 \tilde{R}(\omega_2 - \omega_3) \Sigma \int dT e^{i(\omega - [\omega_2 - \omega_3 + \omega_4])T} \\
 &= \frac{1}{(2\pi)^2} \int d\omega_2 d\omega_3 d\omega_4 \tilde{R}(\omega_2 - \omega_3) \Sigma \delta(\omega - [\omega_2 - \omega_3 + \omega_4]) \quad (\text{F.1.11})
 \end{aligned}$$

where integration over  $T$  was done in the last line. The  $\delta$ -function can be written as  $\delta(\omega_3 - [\omega_2 + \omega_4 - \omega])$  and thus, by integration over  $\omega_3$  one will get

$$\tilde{g}(\omega) = \frac{1}{(2\pi)^2} \int d\omega_2 d\omega_4 \tilde{R}(\omega - \omega_4) \Sigma(\omega_2, \omega_2 + \omega_4 - \omega, \omega_4) \quad (\text{F.1.12})$$

Multiplying by  $\tilde{C}^*(\omega)$  and integrating over  $\omega$  then

$$\begin{aligned}
 \int d\omega \tilde{C}^*(\omega) \tilde{g}(\omega) &= \\
 &= \frac{1}{(2\pi)^2} \int d\omega d\omega_2 d\omega_4 \tilde{R}(\omega - \omega_4) \tilde{C}^*(\omega) \tilde{C}(\omega_2) \times \\
 &\quad \tilde{C}^*(\omega_2 + \omega_4 - \omega) \tilde{C}(\omega_4). \quad (\text{F.1.13})
 \end{aligned}$$



The above expression corresponds to the first term on the RHS of equation. (F.1.7). From it one can also obtain the second term of (F.1.7) by complex conjugation, so

$$\begin{aligned}
\int d\omega \tilde{C}(\omega) \tilde{g}^*(\omega) &= \\
\frac{1}{(2\pi)^2} \int d\omega d\omega_2 d\omega_4 \tilde{R}^*(\omega - \omega_4) \tilde{C}(\omega) \tilde{C}^*(\omega_2) \tilde{C}(\omega_2 + \omega_4 - \omega) \tilde{C}^*(\omega_4) &= \\
\frac{1}{(2\pi)^2} \int d\omega d\omega_2 d\omega_4 \tilde{R}^*(-[\omega_4 - \omega]) \tilde{C}(\omega) \tilde{C}^*(\omega_2) \times \\
&\quad \tilde{C}(\omega_2 + \omega_4 - \omega) \tilde{C}^*(\omega_4). \quad (\text{F.1.14})
\end{aligned}$$

Reality of  $R(T)$  ensures that  $R^*(-\omega) = R(\omega)$  (see Eq. (C.2.5)) so

$$\begin{aligned}
\int d\omega \tilde{C}(\omega) \tilde{g}^*(\omega) &= \\
\frac{1}{(2\pi)^2} \int d\omega d\omega_2 d\omega_4 \tilde{R}(\omega_4 - \omega) \tilde{C}(\omega) \tilde{C}^*(\omega_2) \times \\
&\quad \tilde{C}(\omega_2 + \omega_4 - \omega) \tilde{C}^*(\omega_4). \quad (\text{F.1.15})
\end{aligned}$$

Now renaming the dummy-variables like  $\omega_4 \leftrightarrow \omega$ ,

$$\begin{aligned}
\int d\omega \tilde{C}(\omega) \tilde{g}^*(\omega) &= \\
\frac{1}{(2\pi)^2} \int d\omega d\omega_2 d\omega_4 \tilde{R}(\omega - \omega_4) \tilde{C}^*(\omega) \tilde{C}^*(\omega_2) \times \\
&\quad \tilde{C}(\omega_2 + \omega - \omega_4) \tilde{C}(\omega_4) \quad (\text{F.1.16})
\end{aligned}$$

and defining  $\omega_5 = \omega_2 + \omega - \omega_4$  so  $\omega_2 = \omega_5 + \omega_4 - \omega$  and  $d\omega_5 = d\omega_2$ , then

$$\begin{aligned}
\int d\omega \tilde{C}(\omega) \tilde{g}^*(\omega) &= \\
\frac{1}{(2\pi)^2} \int d\omega d\omega_4 d\omega_5 \tilde{R}(\omega - \omega_4) \tilde{C}^*(\omega) \tilde{C}(\omega_5) \times \\
&\quad \tilde{C}^*(\omega_5 + \omega_4 - \omega) \tilde{C}(\omega_4). \quad (\text{F.1.17})
\end{aligned}$$

Consequently Eq. (F.1.13) and (F.1.17) are identical (make the final integration variable renaming  $\omega_5 \rightarrow \omega_2$  to make it explicit). By Eq. (F.1.7) it then follows that

$$\frac{\partial}{\partial z} \int \frac{|\tilde{C}_I|^2}{b\kappa} d\omega = 0. \quad (\text{F.1.18})$$

so

$$P_N(z) = \int \frac{|\tilde{C}_I|^2}{b\kappa} d\omega = \frac{c\sqrt{A_{\text{eff}}(\omega_0)}}{n_2 n_0} \int n_{\text{eff}}(\omega) \sqrt{A_{\text{eff}}(\omega)} \frac{|\tilde{C}_I|^2}{\omega} d\omega \quad (\text{F.1.19})$$

is a constant. The quantity in Eq. (F.1.19) is the 'IAP GNLSE with frequency dependent effective area as in [17]'-analogue of the photon number introduced in [36]. It can be used as a check on an implementation of a IAP GNLSE-solver by defining the photon number error

$$\text{Err}(z) = \left| \frac{P_N(z) - P_N(0)}{P_N(0)} \right| \quad (\text{F.1.20})$$

and observing that it stays small over the entire length of propagation in a simulation ignoring loss and with  $z$ -independent  $\tilde{L}$ .



## Appendix G

# Obtaining Material Response from Raman Gain Measurement

This Ph.D.-work is on uncharted territories for this department in the sense that it is the first Ph.D.-work to incorporate multiple soft-glass materials like ZBLAN, tellurite or chalcogenide in a solver for the generalized nonlinear Schrödinger equation (GNLSE). Predictions of supercontinuum generation (SCG) by solution of the GNLSE, requires certain input, among which, is the response function of the optical fiber material. The response function  $R = R(T)$  must include both the instantaneous electronic response and the delayed (Raman) response. The response function can be deduced from a measurement of the Raman gain profile for the material, and in this appendix, focus is on how to get from a measurement of the Raman gain profile, and to a functional form of the response function  $R(T)$  that can be input to the GNLSE.

### G.1 The Math: From Measurement to Response Function

The Raman gain profile  $g'_R(\Omega)$  (with unit of  $(\text{Wm})^{-1}$ ) is related to the imaginary part of the Fourier transform (FT) of the delayed response function  $\tilde{h}_R(\Omega)$  by [6]

$$g'_R(\Omega) = 2\gamma f_R \text{Im}[\tilde{h}_R(\Omega)] \quad (\text{G.1.1})$$

where  $\gamma = n_2\omega_p^R/(cA_{\text{eff}})$  is the nonlinear coefficient and  $f_R$  is the fractional Raman contribution introduced in [69]. In the expression for  $\gamma$ ,  $\omega_p^R$  is the pump frequency used during measurement of the Raman gain profile and  $A_{\text{eff}}$  is the effective area of the fiber mode at this particular frequency. The FTs used here are defined in Eq. (2.3.2). It must be noted, that the material response  $h_R(T)$  must be a real function, and from FT theory, it can be shown that mathematically this means  $\tilde{h}_R(\Omega) = \tilde{h}_R^*(-\Omega)$  (see Eq. (C.2.5)), which amounts to the real part of  $\tilde{h}_R(\Omega)$  being even, while the imaginary part is odd. Thus  $g'_R(\Omega)$  from Eq. (G.1.1) is mathematically an odd function. The FT of Eq. (G.1.1) is

$$\int_{-\infty}^{\infty} \text{Im}[\tilde{h}_R(\Omega)] e^{-i\Omega T} d\Omega = \frac{1}{2\gamma f_R} \int_{-\infty}^{\infty} g'_R(\Omega) e^{-i\Omega T} d\Omega. \quad (\text{G.1.2})$$

Using  $\text{Im}[z] = (z - z^*)/(2i)$ ,

$$\begin{aligned} \frac{1}{2i} \int_{-\infty}^{\infty} \left( \tilde{h}_R(\Omega) - \tilde{h}_R^*(\Omega) \right) e^{-i\Omega T} d\Omega = \\ \frac{1}{2\gamma f_R} \int_{-\infty}^{\infty} g'_R(\Omega) [\cos(\Omega T) - i \sin(\Omega T)] d\Omega. \end{aligned} \quad (\text{G.1.3})$$

Because  $g'_R(\Omega)$  is odd, one gets

$$\begin{aligned} \frac{1}{2i} \int_{-\infty}^{\infty} \left( \tilde{h}_R(\Omega) - \tilde{h}_R^*(\Omega) \right) e^{-i\Omega T} d\Omega &= \frac{-2i}{2\gamma f_R} \int_0^{\infty} g'_R(\Omega) \sin(\Omega T) d\Omega \Rightarrow \\ \int_{-\infty}^{\infty} \left( \tilde{h}_R(\Omega) - \tilde{h}_R^*(\Omega) \right) e^{-i\Omega T} d\Omega &= \\ \frac{2}{\gamma f_R} \int_0^{\infty} g'_R(\Omega) \sin(\Omega T) d\Omega. \end{aligned} \quad (\text{G.1.4})$$

Rewriting the left-hand side (LHS) above by using the definition of the FTs we get

$$\begin{aligned} \int_{-\infty}^{\infty} \left( \tilde{h}_R(\Omega) - \tilde{h}_R^*(\Omega) \right) e^{-i\Omega T} d\Omega &= 2\pi h_R(T) - \left[ \int_{-\infty}^{\infty} \tilde{h}_R(\Omega) e^{-i\Omega(-T)} d\Omega \right]^* \\ &= 2\pi [h_R(T) - h_R^*(-T)] \\ &= 2\pi [h_R(T) - h_R(-T)]. \end{aligned} \quad (\text{G.1.5})$$

The response function must be causal, on top of being real, and thus one can conclude from above that for  $T > 0$  we have

$$2\pi [h_R(T) - h_R(-T)] = 2\pi [h_R(T) - 0] = 2\pi h_R(T). \quad (\text{G.1.6})$$

Combining Eq. (G.1.6) and Eq. (G.1.4) one gets

$$h_R(T) = \frac{1}{\pi\gamma f_R} \int_0^\infty g'_R(\Omega) \sin(\Omega T) d\Omega, \quad T > 0. \quad (\text{G.1.7})$$

Furthermore, the causality also dictates that  $h_R(T) = 0$  for  $T < 0$  and we must demand that  $h_R(T)$  is continuous so that  $h_R(0) = 0$ . All in all this can be summarized by

$$h_R(T) = \frac{\theta(T)}{\pi\gamma f_R} \int_0^\infty g'_R(\Omega) \sin(\Omega T) d\Omega, \quad -\infty < T < \infty \quad (\text{G.1.8})$$

where  $\theta(T)$  is the Heaviside step function. By inserting the expression for  $\gamma$  and introducing the modal gain  $g_R = g'_R A_{\text{eff}}$  (with unit m/W), then

$$h_R(T) = \frac{c\theta(T)}{\pi n_2 \omega_p^R f_R} \int_0^\infty g_R(\Omega) \sin(\Omega T) d\Omega. \quad (\text{G.1.9})$$

The fractional Raman contribution  $f_R$  is introduced as a normalization of the delayed response function and found by requiring that

$$\int h_R(T) dT = 1 \quad \text{or equivalently,} \\ f_R = \frac{c}{\pi n_2 \omega_p^R} \int_0^\infty \left[ \int_0^\infty g_R(\Omega) \sin(\Omega T) d\Omega \right] dT. \quad (\text{G.1.10})$$

The full material response is then [6]

$$R(T) = (1 - f_R)\delta(T) + f_R h_R(T) \quad \text{or} \\ \tilde{R}(\Omega) = 1 - f_R + f_R \tilde{h}_R(\Omega). \quad (\text{G.1.11})$$

### G.1.1 Material Response of ZBLAN

To demonstrate the procedure outlined above, a conversion from measurement to response function is provided here. Our collaborators at Aarhus University (AU) have measured the Raman gain profile in a ZBLAN step-index fiber (SIF) with core diameter  $2a = 10.7 \mu\text{m}$  and a numerical aperture (NA) of 0.2. The measurement was done with a pump wavelength of  $\lambda_p^R = 2\pi c/\omega_p^R = 1650 \text{ nm}$ , and the remaining experimental details can be found in [59]. A fit to the measured Raman gain  $g_R(\Omega)$  is also found here, and it is

$$g_R(\Omega) = a_1 e^{-\frac{(\Omega/(2\pi) - \nu_1)^2}{2w_1^2}} + a_2 e^{-\frac{(\Omega/(2\pi) - \nu_2)^2}{2w_2^2}} \quad (\text{G.1.12})$$

Ref.	$a_1$	$a_2$	$\nu_1$	$\nu_2$	$w_1$	$w_2$	$f_R$
	[ $10^{-11}$ cm/W]		[THz]		[THz]		
[59]	0.54	0.25	17.4	12.4	0.68	3.5	0.062

**Table G.1:** Parameters for gain curve fit given by Eq. (G.1.12).

with parameters given in Table G.1. The Gaussian fit is shown in solid black in the left panel of Fig. G.1 where dots mark the data points measured at AU. Processing the measured gain profile by using Eqs (G.1.9) and (G.1.10) finds  $f_R = 0.062$  and obtains the FT pair  $h_R(T) \leftrightarrow \tilde{h}_R(\Omega)$ , defining the full material response function through Eq. (G.1.11), which is plotted in the right panel of Fig. G.1.

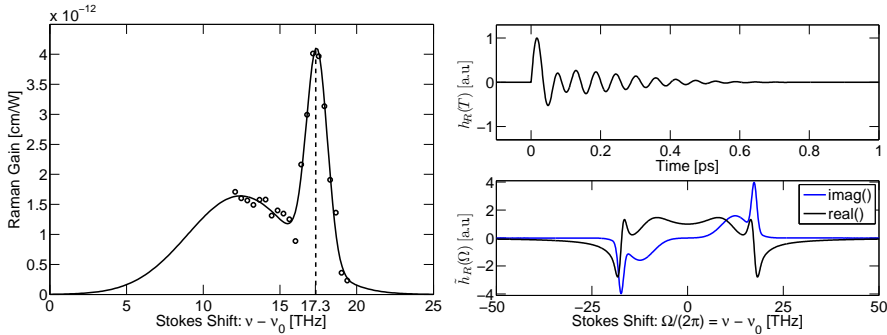


**Figure G.1:** Left: Raman gain measurement (dots) from AU and fitted curve (solid) given by Eq. (G.1.12) [59]. Right: Time domain delayed response  $h_R(T)$  (top) and frequency response  $\tilde{h}_R(\Omega)$  (bottom) as function of Stokes shift.

# List of Acronyms

<b>AU</b>	Aarhus University
<b>CW</b>	continues wave
<b>DFT</b>	discrete Fourier transform
<b>DIRCM</b>	directional infrared counter measures
<b>DTU</b>	Technical University of Denmark
<b>EDFA</b>	erbium doped fiber amplifier
<b>Er</b>	erbium
<b>ESD</b>	energy spectral density
<b>FEM</b>	finite element method
<b>FROG</b>	frequency resolved optical gating
<b>FFT</b>	fast Fourier transform
<b>FT</b>	Fourier transform
<b>FWHM</b>	full-width-at-half-maximum
<b>FWM</b>	four-wave mixing
<b>Ge</b>	germanium
<b>GNLSE</b>	generalized nonlinear Schrödinger equation



<b>GVD</b>	group-velocity dispersion
<b>IAP</b>	interaction picture
<b>iFT</b>	inverse Fourier Transform
<b>IR</b>	infrared
<b>LHS</b>	left-hand side
<b>LIDAR</b>	light detection and ranging
<b>MFD</b>	mode-field diameter
<b>MI</b>	modulation instability
<b>NA</b>	numerical aperture
<b>NLSE</b>	nonlinear Schrödinger equation
<b>NLSM</b>	nonlinear soliton matching
<b>OPPM</b>	one-photon-per-mode
<b>PBG</b>	photonic bandgap
<b>PCF</b>	photonic crystal fiber
<b>Pr</b>	praseodymium
<b>PSD</b>	power spectral density
<b>QCL</b>	quantum cascade laser
<b>RHS</b>	right-hand side
<b>SC</b>	supercontinuum
<b>S</b>	sulfur
<b>SCG</b>	supercontinuum generation
<b>Se</b>	selenium

---

<b>SIF</b>	step-index fiber
<b>SMF</b>	single mode fiber
<b>SPM</b>	self-phase modulation
<b>SSFM</b>	split-step Fourier method
<b>SSFS</b>	soliton self-frequency shift
<b>Tm</b>	thulium
<b>TPA</b>	two-photon absorption
<b>UV</b>	ultraviolet
<b>Yb</b>	ytterbium
<b>ZBLAN</b>	$\text{ZrF}_4\text{BaF}_2\text{LaF}_3\text{AlF}_3\text{NaF}$
<b>ZD</b>	zero dispersion
<b>ZDW</b>	zero dispersion wavelength



# Appendix H

## Bibliography

- [1] D. J. Griffiths, *Introduction to Electrodynamics*. Prentice Hall International Editions, third ed., 1999.
- [2] <https://lasers.llnl.gov/>.
- [3] H. Imam, “Broad as a lamp, bright as a laser,” *Nat. Pho.*, vol. 2, pp. 26–28, Jan 2008.
- [4] T. Izawa, N. Shibata, and A. Takeda, “Optical Attenuation in Pure and Doped Fused Silica in the IR Wavelength Region,” *Applied Physics Letters*, vol. 31, no. 1, pp. 33–35, 1977.
- [5] T. M. Monro and H. Ebendorff-Heidepriem, “Progress in Microstructured Optical Fibers,” *Annual Review of Materials Research*, vol. 36, no. 1, pp. 467–495, 2006.
- [6] G. P. Agrawal, *Nonlinear Fiber Optics*. Academic Press, 4th ed., Oct 2007.
- [7] Z. Chen, A. J. Taylor, and A. Efimov, “Coherent Mid-infrared Broadband Continuum Generation in Non-uniform ZBLAN Fiber Taper,” *Optics Express*, vol. 17, no. 7, pp. 5852–5860, 2009.
- [8] W. Q. Zhang, S. A. V., and T. M. Monro, “A Genetic Algorithm Based Approach to Fiber Design for High Coherence and Large Bandwidth Supercontinuum Generation,” *Optics Express*, vol. 17, pp. 19311–19327, Oct 2009.

- 
- [9] J. M. Harbold, F. O. Ilday, F. W. Wise, J. S. Sanghera, V. Q. Nguyen, L. B. Shaw, and I. D. Aggarwal, "Highly Nonlinear As – S – Se Glasses for All-optical Switching," *Opt. Lett.*, vol. 27, pp. 119–121, Jan 2002.
- [10] R. E. Slusher, G. Lenz, J. Hodelin, J. Sanghera, L. B. Shaw, and I. D. Aggarwal, "Large Raman Gain and Nonlinear Phase Shifts in High-purity As<sub>2</sub>Se<sub>3</sub> Chalcogenide Fibers," *J. Opt. Soc. Am. B*, vol. 21, pp. 1146–1155, Jun 2004.
- [11] Y.-L. Mathis, U. Schade, P. Roy, G. Sockalingum, N. Stone, H.-Y. N. Holman, F. Blankenberg, L. Miller, D. Naumann, J. Kneipp, H. Mantsch, A. Kretlow, P. Lasch, C. Petibois, K. Wehbe, G. Gouspillou, G. Deleris, A. C. Marcelli, G. Cinque, L. Carr, P. Dumas, G. Williams, P. Gardner, E. Gazi, W. Petrich, D. McNaughton, B. Wood, M. Tobin, S. Fisher, J. Sule-Suso, E. O. Faolain, H. J. Byrne, F. M. Lyng, and J. M. Chalmers, *Biomedical Applications of Synchrotron Infrared Microspectroscopy*. RSC Analytical Spectroscopy Series, The Royal Society of Chemistry, 2011.
- [12] B. Napier, *et. al.*, "Mid- to NEar Infrared spectroscopy for improVed medical diAgnostics (MINERVA)," Jan 2012. Proposal for European Commission, ID FP7-ICT-2011-8.
- [13] S. Dupont, C. Petersen, J. Thøgersen, C. Agger, O. Bang, and S. R. Keiding, "IR Microscopy Utilizing Intense Supercontinuum Light Source," *Opt. Express*, vol. 20, pp. 4887–4892, Feb 2012.
- [14] J. M. Dudley, G. Genty, and S. Coen, "Supercontinuum Generation in Photonic Crystal Fiber," *Rev. Mod. Phys.*, vol. 78, pp. 1135–1184, Oct 2006.
- [15] R. R. Alfano and S. L. Shapiro, "Emission in the Region 4000 to 7000 Å Via Four-Photon Coupling in Glass," *Phys. Rev. Lett.*, vol. 24, pp. 584–587, Mar 1970.
- [16] C. Lin and R. H. Stolen, "New Nanosecond Continuum for Excited-state Spectroscopy," *Applied Physics Letters*, vol. 28, no. 4, pp. 216–218, 1976.
- [17] J. Lægsgaard, "Mode Profile Dispersion in the Generalised Nonlinear Schrödinger Equation," *Opt. Express*, vol. 15, pp. 16110–16123, Nov 2007.

- 
- [18] K. Okamoto, *Fundamentals of Optical Waveguides*. Academic Press, second ed., 2006.
- [19] J. J. Ramskov og H. Lottrup Knudsen, *Teori for optiske Fibre*. Electromagnetics Institue, Technical University of Denmark, nb-161 ed., 1986.
- [20] J. C. Knight, T. A. Birks, P. S. J. Russell, and D. M. Atkin, "All-silica Single-mode Optical Fiber with Photonic Crystal Cladding," *Optics Letters*, vol. 21, pp. 1547–1549, Oct 1996.
- [21] J. K. Ranka, R. S. Windeler, and A. J. Stentz, "Visible Continuum Generation in Air-silica Microstructure Optical Fibers with Anomalous Dispersion at 800 nm," *Opt. Lett.*, vol. 25, pp. 25–27, Jan 2000.
- [22] T. A. Birks, J. C. Knight, and P. S. J. Russell, "Endlessly Single-mode Photonic Crystal Fiber," *Optics Letters*, vol. 22, pp. 961–963, Jul 1997.
- [23] M. H. Frosz, *Supercontinuum Generation in Photonic Crystal Fibres: Modelling and Dispersion Engineering for Spectral Shaping*. PhD thesis, Department of Communications, Optics & Materials, Technical University of Denmark, Aug 2006.
- [24] W. Wadsworth, A. Witkowska, S. Leon-Saval, and T. Birks, "Hole Inflation and Tapering of Stock Photonic Crystal Fibres," *Opt. Express*, vol. 13, pp. 6541–6549, Aug 2005.
- [25] M. El-Amraoui, G. Gadret, J. C. Jules, J. Fatome, C. Fortier, F. Désévéday, I. Skripatchev, Y. Messaddeq, J. Troles, L. Brilland, W. Gao, T. Suzuki, Y. Ohishi, and F. Smektala, "Microstructured Chalcogenide Optical Fibers from As<sub>2</sub>S<sub>3</sub> Glass: Towards New IR Broadband Sources," *Opt. Express*, vol. 18, pp. 26655–26665, Dec 2010.
- [26] J. H. V. Price, T. M. Monro, H. Ebendorff-Heidepriem, F. Poletti, P. Horak, V. Finazzi, J. Y. Y. Leong, P. Petropoulos, J. C. Flanagan, G. Brambilla, X. Feng, and D. J. Richardson, "Mid-IR Supercontinuum Generation From Nonsilica Microstructured Optical Fibers," *IEEE Journal of Selected Topics in Quantum Electronics*, vol. 13, pp. 738–749, June 2007.

- 
- [27] J. D. Joannopoulos, R. D. Meade, and J. N. Winn, *Photonic Crystals: Molding the Flow of Light*. Princeton University Press, second ed., July 2008.
- [28] J. Lægsgaard, N. A. Mortensen, and A. Bjarklev, “Mode Areas and Field-energy Distribution in Honeycomb Photonic Bandgap Fibers,” *J. Opt. Soc. Am. B*, vol. 20, pp. 2037–2045, Oct 2003.
- [29] D. Gloge, “Weakly Guiding Fibers,” *Applied Optics*, vol. 10, pp. 2252–2258, Oct 1971.
- [30] J. Hult, “A Fourth-Order Runge-Kutta in the Interaction Picture Method for Simulating Supercontinuum Generation in Optical Fibers,” *J. Lightwave Technol.*, vol. 25, pp. 3770–3775, Dec 2007.
- [31] M. H. Frosz, “Validation of Input-noise Model for Simulations of Supercontinuum Generation and Rogue Waves,” *Opt. Express*, vol. 18, pp. 14778–14787, Jul 2010.
- [32] C. Agger, S. T. Sørensen, C. L. Thomsen, S. R. Keiding, and O. Bang, “Nonlinear Soliton Matching Between Optical Fibers,” *Opt. Lett.*, vol. 36, pp. 2596–2598, Jul 2011.
- [33] C. Agger, C. Petersen, S. Dupont, H. Steffensen, J. K. Lyngsø, C. L. Thomsen, J. Thøgersen, S. R. Keiding, and O. Bang, “Supercontinuum Generation in ZBLAN Fibers - Detailed Comparison Between Measurement and Simulation,” *J. Opt. Soc. Am. B*, vol. 29, pp. 635–645, Apr 2012.
- [34] A. M. Heidt, “Efficient Adaptive Step Size Method for the Simulation of Supercontinuum Generation in Optical Fibers,” *J. Lightwave Technol.*, vol. 27, pp. 3984–3991, Sep 2009.
- [35] O. V. Sinkin, R. Holzlöhner, J. Zweck, and C. R. Menyuk, “Optimization of the Split-Step Fourier Method in Modeling Optical-Fiber Communications Systems,” *J. Lightwave Technol.*, vol. 21, p. 61, Jan 2003.
- [36] K. J. Blow and D. Wood, “Theoretical Description of Transient Stimulated Raman Scattering in Optical Fibers,” *IEEE J. of Quantum Elec.*, vol. 25, pp. 2665–2673, Dec. 1989.

- 
- [37] A. V. Husakou and J. Herrmann, "Supercontinuum Generation, Four-wave Mixing, and Fission of Higher-order Solitons in Photonic-crystal Fibers," *J. Opt. Soc. Am. B*, vol. 19, pp. 2171–2182, Sep 2002.
- [38] J. Hansryd, P. A. Andrekson, M. Westlund, J. Li, and P. O. Hedekvist, "Fiber-based Optical Parametric Amplifiers and their Applications," *IEEE, J. of Selec. Top. QE*, vol. 8, pp. 506–520, May/June 2002.
- [39] J. M. C. Boggio, J. R. Windmiller, M. Knutzen, R. Jiang, C. Bres, N. Alic, B. Stossel, K. Rottwitt, and S. Radic, "730 – nm Optical Parametric Conversion From Near- to Short-wave Infrared Band," *Opt. Express*, vol. 16, pp. 5435–5443, Apr 2008.
- [40] J. R. Ott, M. Heuck, C. Agger, P. D. Rasmussen, and O. Bang, "Label-free and Selective Nonlinear Fiber-optical Biosensing," *Opt. Express*, vol. 16, pp. 20834–20847, Dec 2008.
- [41] C. Lin, V. T. Nguyen, and W. G. French, "Wideband Near-IR Continuum (0.7 - 2.1  $\mu\text{m}$ ) Generated in Low-loss Optical Fibres," *Electronics Letters*, vol. 14, pp. 822–823, 7 1978.
- [42] J. P. Gordon, "Theory of the Soliton Self-frequency Shift," *Opt. Lett.*, vol. 11, pp. 662–664, Oct 1986.
- [43] F. M. Mitschke and L. F. Mollenauer, "Discovery of the Soliton Self-frequency Shift," *Opt. Lett.*, vol. 11, pp. 659–661, Oct 1986.
- [44] A. C. Judge, O. Bang, and C. M. de Sterke, "Theory of Dispersive Wave Frequency Shift via Trapping by a Soliton in an Axially Nonuniform Optical Fiber," *J. Opt. Soc. Am. B*, vol. 27, pp. 2195–2202, Nov 2010.
- [45] G. Qin, X. Yan, C. Kito, M. Liao, C. Chaudhari, T. Suzuki, and Y. Ohishi, "Ultrabroadband Supercontinuum generation From Ultraviolet to 6.28  $\mu\text{m}$  in a Fluoride Fiber," *Applied Physics Letters*, vol. 95, no. 16, p. 161103, 2009.
- [46] M. Horita, "Fiberlabs." private communications, FiberLabs, June 2011.



- 
- [47] C. Xia, Z. Xu, M. N. Islam, F. L. Terry, M. J. Freeman, A. Zakel, and J. Mauricio, "10.5 W Time-Averaged Power Mid-IR Supercontinuum Generation Extending Beyond  $4\text{ }\mu\text{m}$  With Direct Pulse Pattern Modulation," *IEEE, Jour. Selec. Top. in QE*, vol. 15, pp. 422–434, april 2009.
- [48] C. L. Hagen, J. W. Walewski, and S. T. Sanders, "Generation of a Continuum Extending to the Mid-infrared by Pumping ZBLAN Fiber with an Ultrafast 1550-nm Source," *Photonics Technology Letters, IEEE*, vol. 18, pp. 91–93, Jan 2006.
- [49] D. Anderson, M. Lisak, B. Malomed, and M. Quiroga-Teixeiro, "Tunneling of an Optical Soliton Through a Fiber Junction," *J. Opt. Soc. Am. B*, vol. 11, pp. 2380–2384, Dec 1994.
- [50] R. N. Brown and J. J. Dutta, "Material Dispersion in High Optical Quality Heavy Metal Fluoride Glasses," *Appl. Opt.*, vol. 24, no. 24, pp. 4500–4503, 1985.
- [51] M. Monerie, F. Alard, and G. Maze, "Fabrication and Characterisation of Fluoride-glass Single-mode Fibres," *Electronics Letters*, vol. 21, pp. 1179–1181, 5 1985.
- [52] F. Gan, "Optical Properties of Fluoride Glasses: a Review," *Journal of Non-Crystalline Solids*, vol. 184, pp. 9–20, 1995.
- [53] L. Wetenkamp, T. Westendorf, G. F. West, and A. Kober, "The Effect of Small Composition Changes on the Refractive Index and Material Dispersion in ZBLAN Heavy-Metal Fluoride Glass," *Materials Science Forum*, vol. 32-33, pp. 471–476, 1988.
- [54] A. Kasprzak, "iRphotonics." private communications, iRphotonics, Oct 2010.
- [55] C. Xia, M. Kumar, O. P. Kulkarni, M. N. Islam, J. Fred L. Terry, M. J. Freeman, M. Poulain, and G. Mazé, "Mid-infrared Supercontinuum Generation to  $4.5\text{ }\mu\text{m}$  in ZBLAN Fluoride Fibers by Nanosecond Diode Pumping," *Opt. Lett.*, vol. 31, no. 17, pp. 2553–2555, 2006.
- [56] S. R. Loehr and C. T. Moynihan, "Effect of  $\text{H}_2\text{O}$  Partial Pressure on the Rate of Hydration of  $\text{ZrF}_4 - \text{BaF}_2 - \text{LaF}_3 - \text{AlF}_3$  Glass," *Mat. Sci. Forum*, pp. 261–265, 1988.

- 
- [57] D. Szebesta, S. T. Davey, J. R. Williams, and M. W. Moore, "OH Absorption in the Low Loss Window of ZBLAN(P) Glass Fibre," *Journal of Non-Crystalline Solids*, vol. 161, pp. 18–22, 1993.
- [58] C. Agger, C. Petersen, S. Dupont, H. Steffensen, J. K. Lyngsø, C. L. Thomsen, S. R. Keiding, and O. Bang, "ZBLAN Supercontinuum Generation - Detailed Comparison Between Measurement and Simulation," in *CLEO:2011 - Laser Applications to Photonic Applications*, p. CThBB2, Optical Society of America, 2011.
- [59] C. Petersen, S. Dupont, C. Agger, J. Thøgersen, O. Bang, and S. R. Keiding, "Stimulated Raman Scattering in Soft Glass Fluoride Fibers," *J. Opt. Soc. Am. B*, vol. 28, pp. 2310–2313, Oct 2011.
- [60] J. Y. Lee and D. Y. Kim, "Versatile Chromatic Dispersion Measurement of a Single Mode Fiber Using Spectral White Light Interferometry," *Opt. Express*, vol. 14, pp. 11608–11615, Nov 2006.
- [61] R. M. Almeida and J. D. Mackenzie, "Vibrational Spectra and Structure of Fluorozirconate Glasses," *The Journal of Chemical Physics*, vol. 74, no. 11, pp. 5954–5961, 1981.
- [62] Y. Durteste, M. Monerie, and P. Lamouler, "Raman Amplification in Fluoride Glass Fibres," *Electronics Letters*, vol. 21, pp. 723–724, 15 1985.
- [63] A. Saïssy, J. Botineau, L. Macon, and G. Maze, "Diffusion Raman dans une fibre optique en verre fluoré," *Jour. de Phys. Lett.*, vol. 46, no. 6, pp. 289–294, 1985.
- [64] T. Mizunami, H. Iwashita, and K. Takagi, "Gain Saturation Characteristics of Raman Amplification in Silica and Fluoride Glass Optical Fibers," *Opt. Comm.*, vol. 97, no. 1-2, pp. 74–78, 1993.
- [65] X. Yan, C. Kito, S. Miyoshi, M. Liao, T. Suzuki, and Y. Ohishi, "Raman Transient Response and Enhanced Soliton Self-frequency Shift in ZBLAN Fiber," *J. Opt. Soc. Am. B*, Dec 2011.
- [66] L. Liu, G. Qin, Q. Tian, D. Zhao, and W. Qin, "Numerical Investigation of mid-infrared Supercontinuum Generation up to 5  $\mu\text{m}$  in Single Mode Fluoride Fiber," *Opt. Express*, vol. 19, pp. 10041–10048, May 2011.

- 
- [67] N. R. Newbury, "Raman Gain: Pump-Wavelength Dependence in Single-mode Fiber," *Opt. Lett.*, vol. 27, pp. 1232–1234, Jul 2002.
- [68] T. Nakai, N. Norimatsu, Y. Noda, O. Shinbori, and Y. Mimura, "Changes in Refractive Index of Fluoride Glass Fibers During Fiber Fabrication Processes," *Applied Physics Letters*, vol. 56, no. 3, pp. 203–205, 1990.
- [69] R. H. Stolen, J. P. Gordon, W. J. Tomlinson, and H. A. Haus, "Raman Response Function of Silica-core Fibers," *J. Opt. Soc. Am. B*, vol. 6, pp. 1159–1166, Jun 1989.
- [70] C. Xia, M. Kumar, M.-Y. Cheng, R. S. Hegde, M. N. Islam, A. Galvanauskas, H. G. Winful, J. Fred L. Terry, M. J. Freeman, M. Poulain, and G. Mazé, "Power Scalable Mid-infrared Supercontinuum Generation in ZBLAN Fluoride Fibers with up to 1.3 Watts Time-averaged Power," *Opt. Express*, vol. 15, no. 3, pp. 865–871, 2007.
- [71] O. P. Kulkarni, V. V. Alexander, M. Kumar, M. J. Freeman, M. N. Islam, J. Fred L. Terry, M. Neelakandan, and A. Chan, "Supercontinuum Generation from  $\sim 1.9$  to  $4.5\ \mu\text{m}$  in ZBLAN Fiber with High Average Power Generation Beyond  $3.8\ \mu\text{m}$  Using a Thulium-doped Fiber Amplifier," *J. Opt. Soc. Am. B*, vol. 28, pp. 2486–2498, Oct 2011.
- [72] P. Beaud, W. Hodel, B. Zysset, and H. Weber, "Ultrashort Pulse Propagation, Pulse Breakup, and Fundamental Soliton Formation in a Single-mode Optical Fiber," *IEEE Journal of Quantum Electronics*, vol. 23, pp. 1938–1946, Nov 1987.
- [73] J. M. Stone and J. C. Knight, "Visibly "White" Light Generation in Uniform Photonic Crystal Fiber Using a Microchip Laser," *Opt. Express*, vol. 16, pp. 2670–2675, Feb 2008.
- [74] J. M. Dudley, L. P. Barry, P. G. Bollond, J. D. Harvey, and R. Leonhardt, "Simultaneous Measurement of the Dispersion and Nonlinearity of Standard Fibre Using Frequency Resolved Optical Gating," in *Integrated Optics and Optical Fibre Communications, 11th International Conference on, and 23rd European Conference on Optical Communications (Conf. Publ. No.: 448)*, vol. 3, pp. 307–310, Sep 1997.

- 
- [75] I. Kubat, C. Agger, P. M. Moselund, and O. Bang, "Mid-infrared Supercontinuum Generation in Tapered ZBLAN Step-index Fiber by Direct Pumping at 1064 and 1550 nm." Submitted to J. Opt. Soc. Am. B, Oct 2012.
- [76] S. Agger, *Thulium Distributed-feedback Fiber Lasers*. PhD thesis, Department of Communications, Optics & Materials, Technical University of Denmark, Jan 2006.
- [77] D. Marcuse, "Loss Analysis of Single-Mode Fiber Splices," *The Bell Systems Technical Journal*, vol. 56, no. 5, pp. 703–718, 1977.
- [78] D. Buccoliero, H. Steffensen, O. Bang, H. Ebendorff-Heidepriem, and T. M. Monro, "Thulium Pumped High Power Supercontinuum in Loss-determined Optimum Lengths of Tellurite Photonic Crystal Fiber," *Appl. Phys. Lett.*, vol. 97, no. 6, p. 061106, 2010.
- [79] V. V. R. K. Kumar, A. George, J. Knight, and P. Russell, "Tellurite Photonic Crystal Fiber," *Opt. Express*, vol. 11, pp. 2641–2645, Oct 2003.
- [80] P. Domachuk, N. A. Wolchover, M. Cronin-Golomb, A. Wang, A. K. George, C. M. B. Cordeiro, J. C. Knight, and F. G. Omenetto, "Over 4000 nm Bandwidth of Mid-IR Supercontinuum Generation in Sub-centimeter Segments of Highly Nonlinear Tellurite PCFs," *Opt. Express*, vol. 16, pp. 7161–7168, May 2008.
- [81] G. Snopatin, V. Shiryaev, V. Plotnichenko, E. Dianov, and M. Churbanov, "High-purity Chalcogenide Glasses for Fiber Optics," *Inorganic Materials*, vol. 45, pp. 1439–1460, 2009.
- [82] D. D. Hudson, S. A. Dekker, E. C. Mägi, A. C. Judge, S. D. Jackson, E. Li, J. S. Sanghera, L. B. Shaw, I. D. Aggarwal, and B. J. Eggleston, "Octave Spanning Supercontinuum in an As<sub>2</sub>S<sub>3</sub> Taper Using Ultralow Pump Pulse Energy," *Opt. Lett.*, vol. 36, pp. 1122–1124, Apr 2011.
- [83] B. Ung and M. Skorobogatiy, "Chalcogenide Microporous Fibers for Linear and Nonlinear Applications in the Mid-infrared," *Opt. Express*, vol. 18, pp. 8647–8659, Apr 2010.

- 
- [84] M. F. Churbanov, V. S. Shiryaev, I. V. Scripachev, G. E. Snopatin, V. V. Gerasimenko, S. V. Smetanin, I. E. Fadin, and V. G. Plotnichenko, "Optical Fibers Based on As – S – Se Glass System," *Journal of Non-Crystalline Solids*, vol. 284, pp. 146–152, May 2001.
- [85] J. S. Sanghera, L. B. Shaw, P. Pureza, V. Q. Nguyen, D. Gibson, L. Busse, I. D. Aggarwal, C. M. Florea, and F. H. Kung, "Nonlinear Properties of Chalcogenide Glass Fibers," *International Journal of Applied Glass Science*, vol. 1, no. 3, pp. 296–308, 2010.
- [86] A. Seddon, "Private communications." Confidential.
- [87] O. P. Kulkarni, C. Xia, D. J. Lee, M. Kumar, A. Kuditcher, M. N. Islam, F. L. Terry, M. J. Freeman, B. G. Aitken, S. C. Currie, J. E. McCarthy, M. L. Powley, and D. A. Nolan, "Third Order Cascaded Raman Wavelength Shifting in Chalcogenide Fibers and Determination of Raman Gain Coefficient," *Opt. Express*, vol. 14, pp. 7924–7930, Aug 2006.
- [88] R. T. White and T. M. Monro, "Cascaded Raman Shifting of High-peak-power Nanosecond Pulses in As<sub>2</sub>S<sub>3</sub> and As<sub>2</sub>Se<sub>3</sub> Optical Fibers," *Opt. Lett.*, vol. 36, pp. 2351–2353, Jun 2011.
- [89] J. Fatome, C. Fortier, T. N. Nguyen, T. Chartier, F. Smektala, K. Messaad, B. Kibler, S. Pitois, G. Gadret, C. Finot, J. Troles, F. Desevedavy, P. Houizot, G. Renversez, L. Brilland, and N. Traynor, "Linear and Nonlinear Characterizations of Chalcogenide Photonic Crystal Fibers," *J. Lightwave Technol.*, vol. 27, pp. 1707–1715, Jun 2009.
- [90] Z. G. Lian, Q. Q. Li, D. Furniss, T. M. Benson, and A. B. Seddon, "Solid Microstructured Chalcogenide Glass Optical Fibers for the Near- and Mid-Infrared Spectral Regions," *Photonics Technology Letters, IEEE*, vol. 21, pp. 1804–1806, Dec 2009.
- [91] P. M. Moselund, C. Petersen, S. Dupont, C. Agger, O. Bang, and S. R. Keiding, "Supercontinuum: Broad as a Lamp, Bright as a Laser, Now in the Mid-infrared," vol. 8381, p. 83811A, SPIE, 2012.
- [92] H. Steffensen, C. Agger, and O. Bang, "Influence of Two-photon Absorption on Soliton Self-Frequency Shift," *J. Opt. Soc. Am. B*, vol. 29, pp. 484–492, Mar 2012.

- 
- [93] D.-I. Yeom, E. C. Mägi, M. R. E. Lamont, M. A. F. Roelens, L. Fu, and B. J. Eggleton, “Low-threshold supercontinuum generation in highly nonlinear chalcogenide nanowires,” *Opt. Lett.*, vol. 33, pp. 660–662, Apr 2008.
- [94] J. Hu, C. R. Menyuk, L. B. Shaw, J. S. Sanghera, and I. D. Aggarwal, “Maximizing the Bandwidth of Supercontinuum Generation in  $\text{As}_2\text{Se}_3$  Chalcogenide Fibers,” *Opt. Express*, vol. 18, pp. 6722–6739, Mar 2010.
- [95] S. T. Sørensen, A. Judge, C. L. Thomsen, and O. Bang, “Optimum Fiber Tapers for Increasing the Power in the Blue Edge of a Supercontinuum—Group-acceleration Matching,” *Opt. Lett.*, vol. 36, pp. 816–818, Mar 2011.
- [96] M. R. Spiegel, *Schaum’s Mathematical Handbook of Formulas and Tables*. McGraw-Hill, 2 ed., Oct 1998.
- [97] The MathWorks, *Matlab2010a Documentation*, 2010.
- [98] J. G. Proakis and D. K. Manolakis, *Digital Signal Processing*. Prentice Hall, fourth ed., Apr. 2006.